

MID-INFRARED HIGH RESOLUTION IMAGING OF HERBIG AE/BE STARS:
EXPLORING THE GEOMETRY OF CIRCUMSTELLAR DUST

By

NAIBI MARIÑAS

A DISSERTATION PRESENTED TO THE GRADUATE SCHOOL
OF THE UNIVERSITY OF FLORIDA IN PARTIAL FULFILLMENT
OF THE REQUIREMENTS FOR THE DEGREE OF
DOCTOR OF PHILOSOPHY

UNIVERSITY OF FLORIDA

2007

© 2007 Naibi Mariñas

To my grandparents (mima, abuelo Raul, abuela Odilia y abuelo Paco)

ACKNOWLEDGMENTS

I would like to acknowledge my advisor, Charles Telesco, for his love and enthusiasm for astronomy. I will always be indebted to him for giving me the opportunity to work at the Gemini Telescopes as part of the University of Florida mid-infrared instrumentation group. I also like to thank him for allowing me work independently on this research while still providing guidance when I needed it, and for trusting my decisions.

I am grateful to all the committee members for their support during the oral defense. I specially want to thank Dr. Yasu Takano, for taking the time to carefully read and correct all the typos and problems with the written dissertation.

I am very grateful to Chris Packham for being the best friend anyone could ask for, for helping me move along in difficult times, and for reminding me that this was difficult, but doable.

Many other friends also helped along the way: Lori read part of this work and corrected my English, Joanna gave me invaluable advice on how to meet the deadlines during this last semester, and Cynthia was always there to offer a hand when needed.

I also like to thank our secretary, Catherine Cassidy, for taking care of all the paperwork, reminding me deadlines, and pointing out other things that I had to do in order to graduate.

I could never have finished this research without the support of my family: my mom who came on weekends to take care of everything in the house, Ridel who also came every weekend to take care of our son, Onelia who stayed with me this last semester so that I could write this dissertation, and my aunt. I also have to give a very special thanks to my three-year-old son for letting me know that even though he wanted to be with me, it was ok to stay with grandmas and nannies.

I am very thankful to the NASA Graduate Student Research Program (GSRP) and to the South East Alliance for Graduate Education and the Professoriate (SEAGEP) for their financial support.

TABLE OF CONTENTS

	<u>page</u>
ACKNOWLEDGMENTS	4
LIST OF TABLES	9
LIST OF FIGURES	10
ABSTRACT	13
1 INTRODUCTION	15
Star Formation	15
Herbig Ae/Be Stars	19
Geometry of Circumstellar Dust: Disk vs. Envelope	20
Observations	21
Direct imaging	21
Spectroscopy	21
Interferometry	23
Polarization	24
Modeling the Spectral Energy Distribution	24
Research Overview	29
2 MID-INFRARED INSTRUMENTATION, OBSERVATIONS AND DATA REDUCTION	38
Infrared Sky	38
Ground-Based Mid-infrared Astronomy	39
Atmosphere	39
Gemini Observatory	40
Mid-infrared Instruments: Michelle and T-ReCS	42
Observing Technique: Chop-Nod	43
Output Data Files Structure	44
Output Image Spurious Structure	45
Data Reduction	46
Image Cross-Correlation	47
Flat Fielding	47
Sky Subtraction	47
Standard Star Calibration and Airmass Correction	48
Photometry	49
Color-Correction	49
3 SOURCE SAMPLE AND DATA ANALYSIS	59
Herbig Ae/Be Sample	59
Calculating Stellar Properties	59

	Photospheric Emission	60
	Line Emission	62
	Classification of sources	62
	Source Sizes	63
	Point Spread Function	63
	Moffat Function	64
	Measuring Sizes	65
	Properties of the Circumstellar Dust	66
	Dust Temperature	67
	Warm Dust Mass	69
	Dust Size Distribution	70
	State of Evolution of Dust Grains	70
	Opacity	71
	Passive Flared Disk Model	72
4	AB AURIGAE	84
	Observations and Data Reduction	85
	Source Size	86
	Dust Properties	87
	Particle Temperature and Sizes	88
	Dust Optical Depth and Disk Morphology	90
	Models	91
	Conclusions	94
5	RESOLVING HERBIG AE/BE PROTOPLANETARY DISKS IN THE MID- INFRARED: THE GROUP I SOURCES	104
	Introduction	104
	Observations and Data Reduction	106
	Extended Emission	107
	Notes on Individual Sources	108
	HD36112	108
	HD97048	109
	HD100453	111
	HD135344	112
	HD139614	113
	HD169142	114
	HD179218	114
	HD97048: An Alternative Scenario	115
	Spherical Emission: Flaring Disk or Envelope?	119
	Geometry of the Systems: Disks or Haloes?	120
	Conclusions	122
6	RESOLVING HERBIG AE/BE PROTOPLANETARY DISKS IN THE MID- INFRARED: THE GROUP II SOURCES	138

Introduction.....	138
Notes on Individual Sources.....	139
Observations and Data Reduction	144
Extended Emission	145
Dust Properties.....	148
Discussion.....	148
Conclusions.....	151
7 CONCLUSIONS AND FUTURE WORK.....	165
Disk Geometry in Herbig Ae/Be Stars	165
Future Work.....	166
LIST OF REFERENCES.....	171
BIOGRAPHICAL SKETCH	177

LIST OF TABLES

<u>Table</u>		<u>page</u>
3-1	Physical properties of program stars.....	77
4.1	Comparison of flux density measurements for AB Aurigae.....	96
5-1	Log of observations for Group I sources	125
5-2	Standard stars photometry.....	125
5-3	Derived flux measurements.	125
5-4	Quadratic subtracted sizes at 11.7 μm for all Group I sources.....	126
5-5	Quadratic subtracted sizes at 18.3 μm for all Group I sources.	126
6-1	Log of observations for Group II sources	154
6-2	Standard stars flux densities.....	154
6-3	Derived flux densities	155
6-4	Derived dust color temperatures and masses for all sources included in this survey.	155

LIST OF FIGURES

<u>Figure</u>	<u>page</u>
1-1 Stages of stellar and planetary system formation.	30
1-2 H-R diagram showing the locus of different types of stars.	31
1-3 Images of very young stars in the Taurus molecular cloud.	32
1-4 Infrared spectra of the HAeBe stars Elias 1 and HD97048.	33
1-5 Size-luminosity correlation derived from near-infrared interferometric observations	34
1-6 Typical spectral energy distribution (SED) of a HAeBe star.	35
1-7 Schematic of the modified Chiang-Goldreich model.	36
1-8 Schematic of the flat disk plus halo model	37
2-1 ATRAN model of atmospheric transmission for Mauna Kea.	53
2-2 Full width at half maximum measurements as a function of Universal Time	54
2-3 Optical design for a Ritchey-Chrétien telescope.	55
2-4 T-ReCs optical design.....	55
2-5 Filter transmission for T-ReCS (blue) and Michelle (magenta).....	56
2-6 Chop-Nod strategy	57
2-7 Spurious structure in the images	58
3-1 H-R diagram for all the sources included in this survey.....	78
3-2 Spectrum from stellar photosphere	79
3-3 Plot of the ratio of near- to mid-infrared luminosity versus mid-infrared colors	80
3-4 Normalized intensity profile of a Gaussian function and Moffat functions with different parameters β	81
3-5 Representation of the Chiang and Goldreich flaring disk.....	82
3-6 The two solutions for the modified Chiang and Goldreich disk model.....	83
4-1 Near-infrared scattered light of AB Aurigae taken with STIS at the Hubble Space Telescope	97

4-2	Near-infrared scattered light image of AB Aurigae showing spiral structure	98
4-3	AB Auriga false color images.....	99
4-4.	Normalized contour level of AB Aur, PSF star and PSF subtracted emission.....	100
4-5	11.7 μm data (top panel) and 18.1 μm (lower panel) FWHM for AB Aur (solid circles) and PSF star (open triangles)	101
4-6	Ratio of the thermal emission at 11.7 and 18.1 μm shown for different values of λ_0	102
4-7	Radial distribution of the dust temperature from the flaring disk model.....	103
5-1	Clearly resolved sources in the sample.....	127
5-2	FWHM measurements for HD36112, HD139614, and HD179218	128
5-3	Residuals after subtraction of the normalized PSF in the Si-5 filter.....	129
5-4	Group I sources and PSF stars in the Si-5 filter.....	130
5-5	Group I sources and PSF stars in the Qa filter.....	131
5-6	Modeled and observed emission from a flared disk with an inclination of ~ 45 degrees.	132
5-7	HD97048 cross-convolved Gemini images	133
5-8	Location of the Herbig star HD97048 on the southeastern edge of the Chameleon I dark cloud.....	133
5-9	IRAS images of the Ced111, reflection nebula associated with HD97048	134
5-10	H band polarization map of ChaI IRN.....	135
5-11	1.3 mm observations of HD97048 showing the offset of mm emission relative to the optical and near-infrared source position.....	135
5-12	Offset of the Si-5 and Qa peak of emission relative to the optical position of HD97048 (left panel) and PSF star (right panel).....	136
5-13	Ratio of the thermal emission at 11.7 and 18.3 μm for different values of λ_0	137
6-1	FWHM sizes versus UT time.....	156
6-2	Residual emission at 11.7 μm	157
6-3	Photometry from the literature and from this study for the companion source to HD144668 (Rossiter 3930).....	158

6-4	H-R Diagram showing the position of HD144668 (largest circle) and Rossiter 3930 (smallest circle).....	159
6-5	Plot of the ratio of near- to mid-infrared luminosity versus mid-infrared colors	160
6-6	Measured sizes at the FWHM level in the Si-5 and Qa images.....	161
6-7	Ratio of warm to cold dust disk mass for all the sources with available cold dust mass values in the literature	162
6-8	Correlation of sizes and fraction of extended to total emission as a function of age.	162
6-9	Group I and Group II sources in the H-R diagram	163
6-10	Color temperatures for all the sources included in this survey as a function of stellar ages	164
7-1	Sketch of the evolution of protoplanetary disks in HAeBe stars	169
7-2	Spatial resolution of Spitzer (blue line) from near- to far-infrared wavelengths and the IRAS (red lines) spatial resolution.....	170

Abstract of Dissertation Presented to the Graduate School
of the University of Florida in Partial Fulfillment of the
Requirements for the Degree of Doctor of Philosophy

MID-INFRARED HIGH RESOLUTION IMAGING OF HERBIG Ae/Be STARS:
EXPLORING THE GEOMETRY OF CIRCUMSTELLAR DUST

By

Naibí Mariñas

May 2007

Chair: Charles M. Telesco
Major: Astronomy

Herbig Ae/Be (HAeBe) stars are emission line pre-main-sequence stars of intermediate mass. Circumstellar dust is well established as the origin of the large infrared excesses characteristic of these stars; however, the geometry of this dust has remained controversial for a long time. The sources have been divided into two groups depending on the infrared excess: Group I sources have strong near- to far-infrared excesses, and Group II sources, only have strong near-infrared excess. Previous studies associate Group II sources with optically thick flat disks and Group I sources either with optically thick flat disks surrounded by haloes or flaring disks with an inner hole at the dust sublimation radius and a puffed up inner wall. These two models predict the same overall flux at all wavelengths. An evolutionary scenario has been proposed in which grain growth, dispersion, and settling of larger grains towards the mid-plane change the geometry of circumstellar dust from flaring disks in Group I sources, to flat cold disks in Group II sources in about 1 Myr.

For this study, I imaged a sample of 20 HAeBe stars (8 Group I and 12 Group II) in the mid-infrared from the 8-meter Gemini telescopes. I resolve extended emission in all Group I sources with sizes tens to hundreds of AU. Most of the resolved emission is spherical, which

could be interpreted either by a halo or the surface of an almost face-on flaring disk; however, the distribution of dust grain sizes that I derived from these observations, with larger grains at smaller radii is inconsistent with halo models. Only three of the Group II sources are extended and two of them show emission consistent with highly inclined disks. I find no correlation between stellar ages and geometry of the circumstellar material supporting an evolution from Group I sources to Group II sources, on the contrary, Group II sources are younger than Group I sources and all resolved sources presented here are older than 1 Myr.

CHAPTER 1 INTRODUCTION

During the last two decades and motivated by a desire to understand the origin of our own solar system, a significant effort has been placed into the study of pre-main-sequence (PMS) stars. These studies combined with the advances in stellar evolution modeling, have allowed us to integrate the observational properties of young stars at different wavelengths and create a coherent theory of the physical processes involved in the formation and evolution of stars and planetary systems. In this research I discuss the properties and geometry of dust around young stars of intermediate mass. These circumstellar structures of gas and dust are the remnants of the stellar formation process and the sites of planetary systems formation.

Star Formation

We can divide the stellar formation process into four stages. During the first stage of star formation, when the balance between pressure and self-gravitation is lost, dense cores form in a massive, cold, nearly static molecular cloud. The cloud starts to collapse, fragmenting into smaller (\sim few solar masses) regions. The resulting fragments continue to collapse on their own in a quasi-isothermal mode because the densities are too low to prevent cooling. Most of the energy released during the gravitational collapse is radiated away and absorbed by the optically thick envelope, keeping the interstellar gas in an envelope surrounding the core almost isothermal. The spectral energy distribution of the system at this stage is the signature of the collapsing envelope and peaks in the mid- to far-infrared wavelengths (Figure 1-1, top row). When the density and temperature of the core become coupled and the collapse becomes adiabatic, fragmentation stops and the different cores evolve into protostars. The density at the core determines the rate of matter infall onto the core. The timescale for this process, t_{ff} , is given by

$$t_{ff} = \sqrt{\frac{3\pi}{32G\rho_c}} \quad (1.1)$$

where G is the gravitational constant and ρ_c is the density of the core. Eventually, when the pressure at the central core becomes significant, the core reaches quasi-static equilibrium and becomes a protostar on the Kelvin-Holmholtz timescale given by

$$t_{KH} = \frac{GM_c}{R_c L_c} \quad (1.2)$$

where M_c , R_c , and L_c are the mass, radius and luminosity of the core respectively. During the second stage, gas and dust closer to the core accrete faster onto the protostar than the mass at larger radii, and pressure gradients develop. Matter originating far from the rotation axis (defined by the average angular momentum of the circumstellar material) has too large an angular momentum to fall onto the protostar and begins to settle into a disk. The high accretion rates power bipolar outflows, which are aligned with the rotation axis of the system, and material near the poles in the envelope starts to clear. At this point the spectral energy distribution of the system has two components. It is still dominated by the circumstellar material peaking in the mid-infrared; however, the protostar is beginning to emerge at shorter wavelengths (Figure 1-1, second row)

In the third stage, accretion rates decrease, the envelope is mostly lost, and circumstellar gas and dust are confined to a massive optically thick disk. This is thought to be the birthplace of planets; therefore, the disk is called a protoplanetary disk. In the center of the system, the protostar continues to contract until the core temperature is high enough to ignite nuclear reactions. At this point the release of nuclear energy stops the collapse on the core and the

protostar becomes a star, reaching the zero age main sequence (ZAMS). The spectral energy distribution of the system is now dominated by the optically visible star and peaks in the UV; however, there is still a significant contribution of emission from dust at longer wavelengths (Figure 1-1, third row).

During the last stage, the physical properties of the star remain mostly unchanged while the star burns the hydrogen available in its core. The star becomes a main sequence star. In the circumstellar disk, solid particles in orbit around the star settle into a layer in the mid-plane of the disk and grow by collisions. The dust becomes optically thin to radiation from the star and very little, if any, gas remains in the disk. At this point, the protoplanetary disk is called a debris disk since most of the dust in the system has been reprocessed. Main sequence stars surrounded by debris disks are sometimes called Vega-type stars. In the spectral energy distribution of these sources, there is very little excess emission in the mid-infrared due to a remnant dust disk (Figure 1-1, bottom row). Growth continues through settling of small dust particles onto larger particles and the gravitational pull of neighboring material. Some planetesimals become large enough to accrete gas and form giant planets.

One would expect to be able to extend this theory of star formation to intermediate (~ 2 to 8 solar masses) and high mass (> 8 solar masses) stars; however, we have seen that the timescales controlling these processes depend mostly on the mass of the original protostar. Therefore, the timescales for the evolution of the central star and its surrounding material are different. If $t_{KH} > t_{ff}$, the protostar will still be contracting when the high accretion from the envelope stops. This happens for stars of mass lower than 8 solar masses. However, if $t_{ff} > t_{KH}$, the core will evolve faster than the free-falling envelope and the star will reach the ZAMS while still embedded in an accreting envelope.

There are also two different mechanisms for burning hydrogen in stars depending on the initial protostellar mass. The proton-proton (PP) cycle uses only hydrogen to fuse helium. Since hydrogen has only one proton, the temperature required to start this process is only about 10 million K, and the energy generated in this process is proportional to T^4 . This cycle predominates in low mass stars ($M < 1.5$ solar masses). More massive stars need more energy to balance self-gravitation and stop the collapse. If a more massive protostar has carbon, nitrogen and oxygen present in its core, when it reaches temperatures of ~ 16 million K, it initiates the carbon-nitrogen-oxygen (CNO) cycle. The energy released in this process is more sensitive to temperature ($E \sim T^{20}$) and can balance the contraction of the star. The different internal temperatures of low and high mass stars also cause different mechanisms of energy transfer in their cores. In more massive stars temperature changes rapidly with distance so that

$$\left. \frac{dT}{dr} \right|_{actual} > \left. \frac{dT}{dr} \right|_{adiabatic}, \text{ and the fluid becomes unstable and boils transferring energy by}$$

convection. Cores of lower mass stars remain adiabatic and energy transfer occurs by radiative processes.

On this basis, three types of PMS stars can be defined: (1) low mass ($M < 2$ solar masses) stars, also called T-Tauri stars, have radiative cores and are optically visible during their PMS phase; (2) intermediate mass stars (2 to 8 solar masses), also called Herbig Ae/Be (HAeBe) stars, have convective cores and are visible during part of their PMS phase; (3) massive ($M > 8$ solar masses) stars have convective cores and remain invisible in the optical during the whole PMS phase. The intermediate mass stars represent an interesting transition between the well-studied T-Tauri stars and their high mass counterpart and are the subject of this research.

Herbig Ae/Be Stars

In 1960, Herbig discovered a class of emission line stars of spectral types A and B associated with nebulosity and claimed them to be the high mass counterpart of T-Tauri stars. All the stars were located in obscure regions (star forming regions), had spectra with emission lines, and were illuminating bright reflection nebulae (rejecting nebulous objects).

Subsequent studies extended the membership criteria to include stars of spectral type F8 or earlier and provided better continuity with T-Tauri stars (Finkenzeller and Mundt, 1984). They also proved the PMS nature of these stars. Comparison of the stellar radial velocity of 27 HAeBe stars from photospheric Balmer lines to radial velocities of molecular clouds from molecular lines showed that there was no systematic stellar motion relative to the clouds, and the stars were still associated with the star forming regions (Finkenzeller and Jankovics, 1984). Palla and Stahler (1993) revised early evolutionary models and the role of deuterium burning disproving the idea that stars heavier than 3 solar masses would not be observable during their PMS phase, and showed the observational birthline (where stars first appear as optically visible sources) for intermediate mass stars in the Hertzsprung-Russel (HR) diagram¹ (Figure 1-2). Calculation of effective temperatures, surface gravities and stellar luminosities (Strom et al. 1972; Cohen and Kuhn 1979; van den Ancker et al. 1998) allowed the positioning of HAeBe stars in the H-R diagram where they appeared above the zero-age main sequence (ZAMS) in evolutionary tracks still moving toward the main sequence (MS). The strong ultraviolet and infrared excess discovered by Mendoza (1966) could not be explained by free-free, free-bound, and bound-bound emission in hot gas, but required dust thermal emission to account for the

¹ The HR diagram is used to identify the evolutionary status of a star. It plots the effective temperature (T_{eff}) of the star on the x-axis versus the luminosity of the star (L) in the y-axis on a logarithmic scale. During its lifetime a star changes position in the diagram following evolutionary tracks dictated by the mass of the original protostar.

larger excesses beyond 1 μm . The detection of the dust related silicate feature in the 10 μm band of some HAeBe stars offered further evidence of the presence of circumstellar (CS) dust clouds (Cohen 1980, Berrilli et al. 1992).

During the 1980s, the number of candidate HAeBe stars increased significantly when Infrared Astronomical Satellite (IRAS) found a large number of stars resembling HAeBe, but located in isolated regions. A catalogue of HAeBe stars by The et al. (1994) included 287 sources with the following membership criteria:

- Spectral type B to F8
- Near or far infrared excess due to circumstellar material
- With or without:
 - Reflection nebulae
 - Association with obscure star forming region
 - Emission lines
- Sometimes with:
 - Irregular photometric variations
 - Variable or high degree of linear polarization

Geometry of Circumstellar Dust: Disk vs. Envelope

The presence of cool circumstellar material in HAeBe stars is well established as the origin of their characteristic large infrared and sub-millimeter excesses; however, the spatial distribution of this material remains controversial. The intrinsic complexity expected in these more massive environments makes multiple interpretations of the same observational data

possible. In addition, there seems to be an equal amount of observational evidence favoring spherical and axis-symmetric geometries.

Observations

Direct imaging

Imaging of CS material at different wavelengths directly reveals the geometry of the systems; however, these observations are limited by the spatial resolution of the telescopes used. In the sub-mm, imaging of HAeBe star in continuum and molecular line emission (Mannings and Sargent 1997, 2000, Corder et al. 2005, Pietu et al. 2005) showed gas emission regions extending hundreds of AU in size. Masses of the CS material from these observations were in the range of 0.01 – 0.05 solar masses, and because there is low optical extinction toward the stars in all these systems, this provided strong evidence for the existence of optically thick disks where most of the cold mass could reside without covering the central star.

Optical and near-infrared scattered light images from Hubble Space Telescope (HST) revealed large (hundreds of AU) disks in some sources, sometimes immersed in more extended nebulosities, Figure 1-3. Structures (gaps, spirals) that signal the presence of large bodies clearing the dust or gravitational instabilities in the disks were also visible (Grady et al. 1999, 2001). Mid-infrared imaging from large ground-based telescope has also resolved extended emission in a few sources (Fisher et al. 2000, Polomski et al. 2002, Jayawardhana et al. 2001).

Spectroscopy

A study of emission lines of HAeBe stars by Hamann and Persson (1992) found a correlation between excess infrared luminosity and Ca II line strength. The correlation could be explained if the lines originate from material accreting onto the star or from fully ionized matter very close to the stars evaporating due to intense thermal and radiative pressure. Lorenzetti et al. (1994) explained the correlation between H α and L band (3.5 μ m) excess in a similar fashion,

either resulting from winds powered by accretion or from very small excited superheated grains emitting in the near-infrared as they cool down to equilibrium temperatures.

The presence of only blue-shifted wings in some forbidden line emission in HAeBe stars has also been attributed to a disk obscuring the red-shifted flow. The study of [SII] by Corcoran and Ray (1994) revealed some optical veiling (presence of non-stellar continuum) in the more embedded stars supporting accretion models. The small percentage of detection was attributed to the increased brightness of the stellar continuum of HAeBe stars in comparison to T-Tauri stars, which may reduce the chance of revealing forbidden line emission. However, a similar study of [OI] forbidden line emission showed that most of the surveyed sources had unshifted symmetric line profiles implying an absence of CS disks at the scale mapped by the [OI] forbidden line emission (Bohm and Catala 1994). More recently, Acke, van den Ancker and Dullemond (2005) studied the origin of this more spherical [OI] forbidden line emission and found a strong correlation of line strength with 60 μm continuum excess emission. They interpreted their findings in the context of a flared disk model. In this scenario UV radiation from the star can penetrate more deeply into the flared disk, photodissociation of OH molecules in the disk and non-thermal excitation of oxygen in the atmosphere of the disk were able to reproduce the observations.

Near-infrared spectroscopy from Infrared Space Observatory (ISO) showed that while the near-infrared excess is similar for all HAeBe stars, there are large differences in the mid- and far-infrared excesses prompting the separation of these sources into two subgroups, with Group I sources having strong near- and far- infrared excess, and Group II, only strong near-infrared excess (Meeus et al. 2001). They also showed that the infrared spectrum of these sources is dominated by amorphous and crystalline silicates, and in some cases by polycyclic aromatic

hydrocarbon (PAH) emission, Figure 1-4. Silicates have been observed in many young stars; the general idea is that amorphous silicates from the interstellar medium (ISM) are crystallized within CS disks. Van Boekel et al. 2003 showed a relationship between the silicate emission strength and shape of these systems. The change in shape from a narrow peak to a broader feature was explained by an increased in grain sizes and larger amount of crystalline silicates. PAH emission lines are only seen in Meeus group I sources (those with stronger excesses) and are thought to originate in optically thin dust around the star (Acke and van den Ancker 2004), either as an optically thin halo or the surface of a flaring disk.

Recently, mid-infrared spectroscopy with high spatial resolution has revealed radial variations of dust composition with crystalline silicates dominating the regions closer to the star and a mixture of crystalline and amorphous silicates at larger distances (van Boekel et al. 2004).

Interferometry

Interferometry combines the light waves captured by multiple telescopes to achieve higher spatial resolution. Near-infrared interferometry is used to probe the hot circumstellar dust very close to the star. Millan-Gabet (2001, 1999) resolved the inner regions of a group of HAeBe systems with typical source sizes of 0.5-0.9 AU. Their observations were consistent with symmetrical brightness distribution in all resolved sources and since we expect different inclination angles in disk systems, they ruled out the presence of disks. They also found that the near-infrared excess was similar in all sources independent of the sizes of the emitting regions. More recently, interferometric observations with larger baseline are showing evidence of inclination in these systems (Eisner et al. 2004, 2003) favoring the presence of disks. Eisner et al. (2004) and Monnier et al. (2005) also found a strong correlation between the derived sizes and the stellar and accretion luminosity of the sources, Figure 1-5. The correlation can be explained if the source size is set by the dust sublimation temperature, which depends on the stellar and

accretion luminosity and on the properties of the dust (Tuthill 2001, Natta 2001, Muzerolle 2003). The observations can be explained if the near-infrared emission originates on curved inner walls at the dust-destruction radius (Monnier et al. 2006). Mid-infrared interferometry has also resolved extended emission in these sources with sizes for the extended warm dust of a few 10 AU at most (Leinert et al. 2004).

Polarization

Polarimetry provides additional information about the geometry of these systems because CS material causes polarization in the light from the system due to scattering from dust. Resolved extended axisymmetric geometries show spatial changes in the polarization vector, unresolved axisymmetric geometries viewed with some inclination angle will have some degree of polarization, while unresolved disk-like structures viewed face-on and spherical distributions produce polarization vectors that cancel each other out resulting in a zero net polarization for the system. Optical linear polarization (Maheswar et al. 2002) and H α spectropolarimetry observations (Vink et al. 2005, 2002) of HAeBe stars provided evidence for the presence of disk-like CS structures. Change in linear polarization was found in a group of sources with earlier types having a broad polarization consistent with a small scale (~ 0.07 AU) flattened structure, and later types (A2-F) showing a line polarization characteristic of a compact H α emission region being polarized by a rotating disk-like medium. The majority of the sources with known outflows or companion stars had polarization vectors close to perpendicular or parallel to the outflow or binary position angle.

Modeling the Spectral Energy Distribution

Modeling the observed spectral energy distribution (SED) of the sources is one way to gain insight as to the geometry of the CS material. Assuming radiative equilibrium, the flux from the

central star absorbed by a grain at a distance r equals the power radiated by the grain, which allow us to calculate the radial temperature distribution, $T(r)$, of the CS material. With some knowledge about the density distribution and physical properties of the grains, the SED of the CS material can be computed for different geometries.

Hillenbrand et al. (1992) modeled the SED of 47 HAeBe stars and proposed an evolutionary sequence based on the slope of the SED in the infrared: group II sources had flat or rising spectra and were modeled by a star plus accretion disk surrounded by a spherical envelope; group I sources had spectral slope $\lambda F_\lambda \propto \lambda^{-\frac{4}{3}}$ and could be fitted by using only a star plus a flat accretion disk; and group III sources had very little infrared excess emission that could be explained by free-free emission from an ionized region around the star, and did not required dust thermal dust emission to be present. The proposed evolutionary sequence in this classification was group II-group I-group III (Natta et al. 1998). In order to fit a 3 μm peak observed in the spectra of early type HAeBe stars with flat disks, Figure 1-6, the model required high accretion rates (6×10^{-7} to 8×10^{-5} solar masses per year) and inner holes of 5 to 20 stellar radii in the disks so that the observed excess near-infrared luminosity in these systems originated from accretion of circumstellar dust onto the central star.

The main problem with this model arose from the high accretion rates required for the models to keep the region inside the inner hole optically thin. Clearing of grain dust around a star is expected inside the dust sublimation radius, the distance at which grains are heated to ~ 1500 K and annealed; however, this inner region will remain optically thick at the high accretion rates needed to fit the models (Hartman, Kenyon, and Calvet 1993). For an accretion disk, the radial temperature distribution is set by the luminosity of the central star and the accretion luminosity. The disk temperature increases with decreasing radius and since the opacity of the material

increases with increasing temperature, there should be an optically thick inner region, even inside the dust sublimation radius. In addition, these high accretion rates were incompatible with observations. To eliminate this problem, Hartman, Kenyon and Calvet (1993) proposed three different scenarios as possible sources for the 3 μm emission peak: 1) thick infalling envelopes with empty cavities to provide a clear line of sight to the hot central region producing the emission (model with very limiting parameters for all sources); 2) presence of companion plus envelope (which would require all HAeBe stars to be binaries with clear line of sight to the central HAeBe star and high extinction towards the companion to explain the high frequency of the emission peak); and 3) dusty optically thin envelopes with a population of very small transiently heated dust grains. This last alternative model explained the 3 μm emission in early type HAeBe stars and its absence in later spectral types since F-type stars do not produce enough UV photons to heat large populations of very small grains to high temperatures.

Passive disks (flat and flared) were also invoked to explain the observed SED (Lada and Adams 1992). Even though symmetric dust and gas envelopes were not the only possibility, they were still required to explain the infrared component of the spectra in some HAeBe stars (Berrilli et al. 1992, Pezzuto et al. 1997, Di Francesco 1994, Evans and Di Francesco 1995) and a combination of geometries at different spatial scales seemed to be the only approach (Natta et al. 1993, Malfait et al. 1998).

Until this point, all the models assumed radiative equilibrium, and power-law approximations for the dust density distribution. Chiang and Goldreich (1997) were the first to self-consistently calculate the disk structure by considering hydrostatic and thermal equilibrium in a passively irradiated disk. The gravitational force acting on a particle around a star has two components: the horizontal component forces the particle to move in keplerian orbits around the

central star, while the vertical component pulls the particle towards the disk mid-plane. The net result of gravity on circumstellar material is a flat keplerian disk. However, protoplanetary disks also have large amounts of gas, and gas pressure can counter the vertical component of the gravitational force resulting in a disk scale height that depends on the balance between gas pressure and gravity. The Chiang-Goldreich disk model results in a flaring disk with an inner optically thick layer where most of the disk mass is concentrated, and an optically thin surface layer. The disk flares and intercepts more stellar radiation than a flat disk, especially at larger radii. This model was able to reproduce the SED of T-Tauri stars without recurring to high accretion rates or a combination of geometries; however, it failed to account for the near-infrared 3 μm bump in the SED of HAeBe stars.

Dullemond, Dominik, and Natta (2001) proposed a modified Chiang-Goldreich model able to fit the SED of HAeBe stars at all wavelengths. In a passively irradiated disk, dust very close to the star is destroyed because of the very high temperatures in this region. As a result, the inner disk close to the star is cleared of dust at the dust sublimation radius, truncating the disk at this point. Gas might still be present in this “inner hole”; however, since the disk is passive, accretion does not play a role and the holes remain optically thin to stellar radiation. The inner rim at the dust sublimation radius directly receives radiation from the star and is very hot, as a result the vertical scale height at this point increases casting a shadow over the disk behind it. The region in the shadow becomes colder and collapses. At larger radii, depending on the opacity of the disk, the disk can take two different geometries: if the optical depth is higher than a threshold value, the disk’s outer regions flare and leave the shadowed region; if the optical depth is below that value, the disk can never leave the shadow of the inner rim and remains flat and cold at larger radii (Dullemond and Dominik 2004). This geometry, Figure 1-7, is able to reproduce

the SED of HAeBe stars and reconcile observations of these systems at different wavelengths. The only drawback of the model is that it approximates the inner rim by a vertical wall and since radiation from the inner rim is responsible for the 3 μm feature in the SED, systems need to be viewed at an inclination angle of ~ 45 degrees to have full view of the rim radiation (if viewed close to face-on, the inner rim becomes a very thin annuli and the observed radiation from the rim decreases considerably). This problem can be solved if curved inner walls in the rim are introduced so that more of the rim radiation is visible for face-on disks as addressed by the authors. This model will be addressed in more detail later in this research.

If the previously mentioned model can account for the observed SED of HAeBe stars without recurring to an envelope, Vinkovic, Ivezić, and Miroshnichenko (2003) have shown that by combining an optically thick flat disk and an optically thin halo, Figure 1-8, the same SED is obtained. Since the dust in the flaring surface of the disk is optically thin, the temperature of this dust depends only on the distance to the star and the grazing angle (the angle at which stellar radiation is received) and spherical geometries with some assumed density profiles could produce identical results. Therefore, it is impossible to distinguish between the two configurations based only on the SED of the sources, leaving direct imaging the only way to decipher the intrinsic geometry of HAeBe systems.

As we have seen, modeling the SED's of HAeBe stars does not provide unique physical parameters to constrain the geometry. In addition, Brandner et al. 2002 showed that a slight change in the viewing angle of a disk can lead to large differences in the observed SED of the source (class I to class II) and large grains close to the star can mimic the spectra of small grains further from the star. The detection of cold companions around some of these sources adds to the complexity of HAeBe star environments. The uncertainties in the models and the lack of

consensus in the interpretation of the observations prove that, in order to make progress in the study of PMS intermediate mass stars, direct observations of a large sample with enough spatial resolution to see the inner regions around these sources and constrain grain properties of the CS dust are needed.

Research Overview

This research focuses on the geometry and properties of the warm CS dust in HAeBe stars. I observed 20 sources using the mid-infrared cameras T-ReCS and Michelle in the Gemini North and South Telescopes to obtain high angular resolution and high sensitivity images in the 10 and 20 μm regions. These observations allowed us to resolve or place severe limits on the sizes of the mid-infrared emitting regions and characterize the structure of resolved sources. In Chapter 2, I introduce mid-infrared astronomy and instrumentation and describe the observation technique and data reduction procedures used in this study. In Chapter 3, I discuss our source sample and data analysis. In Chapter 4, I present our results for AB Aurigae, the prototype HAeBe star. In Chapter 5, I discuss the CS dust for Group I sources (in the classification of Meeus et al. 2001). In Chapter 6, I describe the results for the Group II sources and discuss general results from the survey; and in Chapter 7, I summarize the results and provide a coherent picture of the HAeBe CS environments. I also discuss areas of future research.

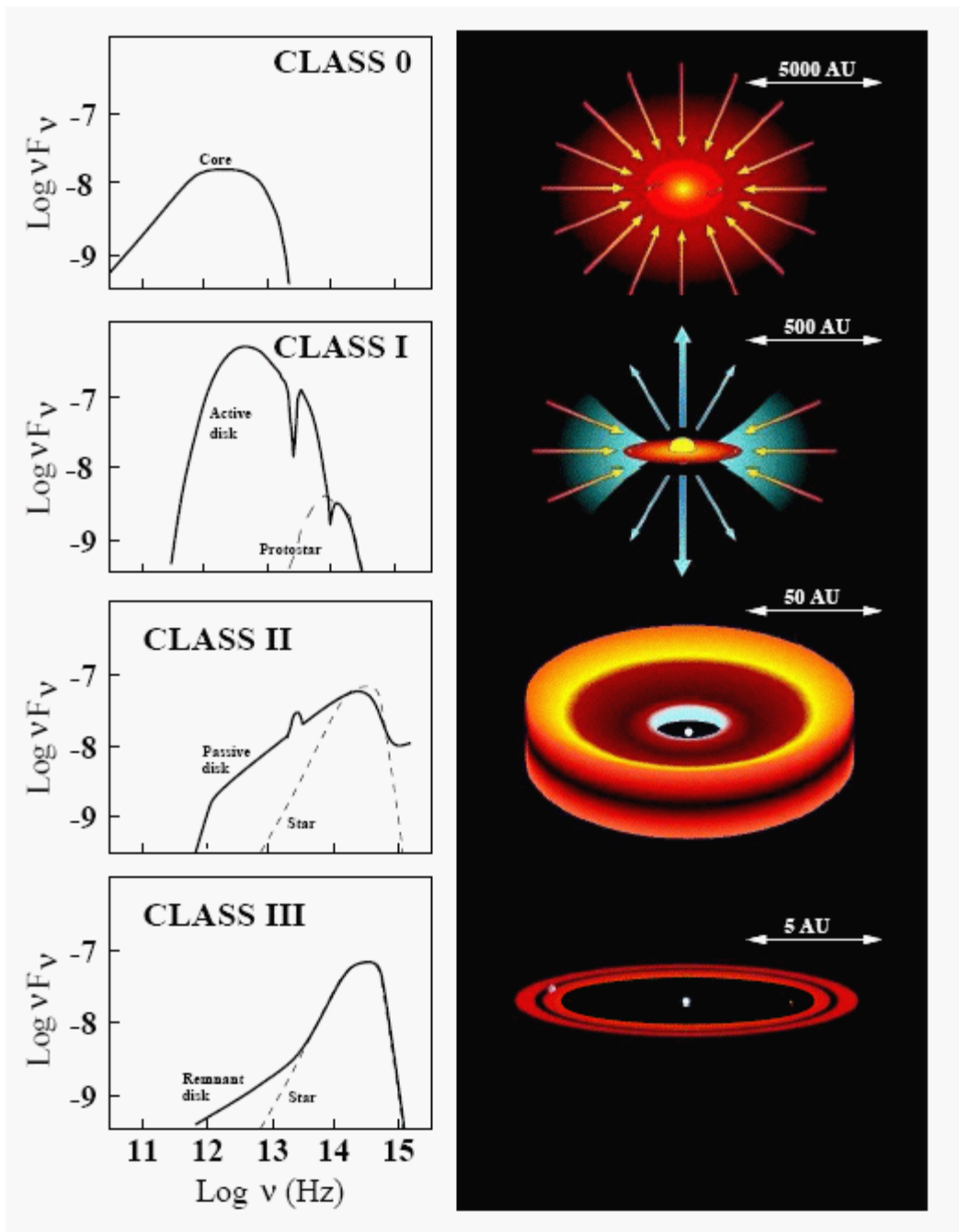


Figure 1-1. Stages of stellar and planetary system formation. Modified image from NASA website. Image credits: Shu et al. 1987, Dullemond et al. 2001

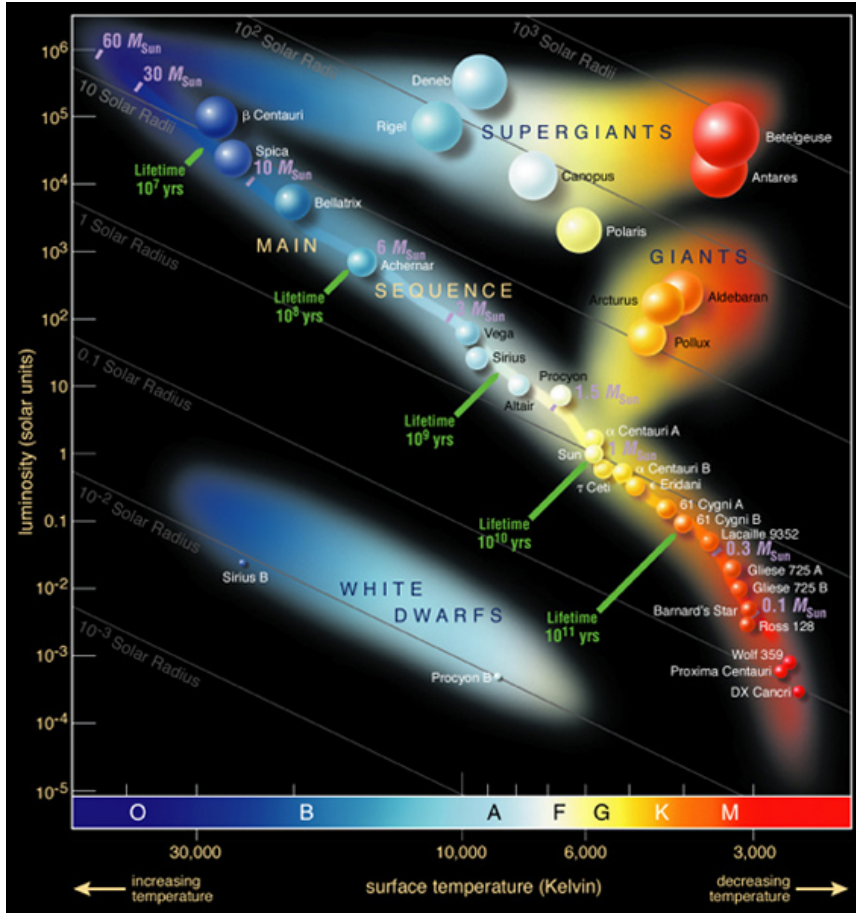


Figure 1-2. H-R diagram showing the locus of different types of stars. Image credit: Pearson Education, Addison Wesley.

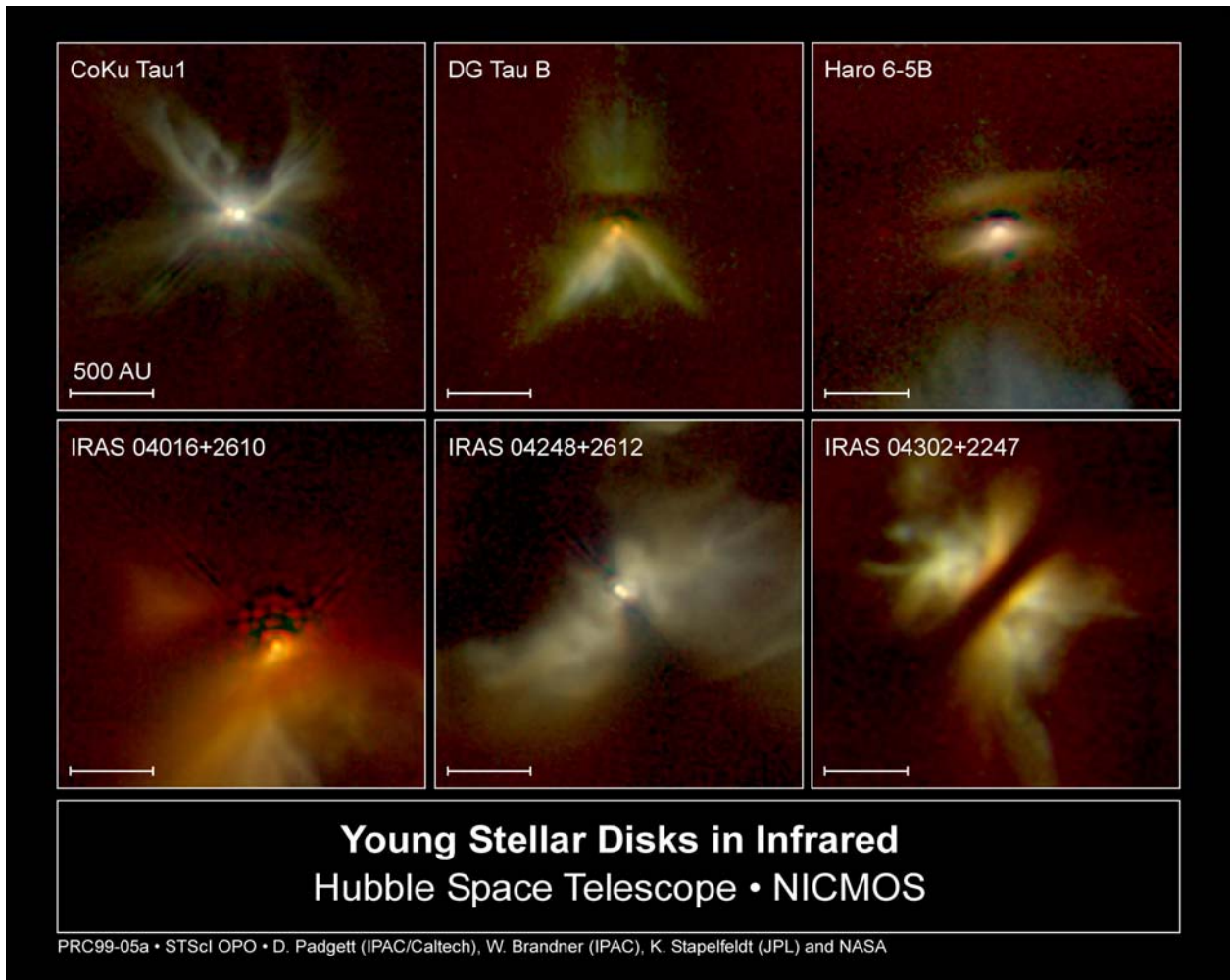


Figure 1-3. Images of very young stars in the Taurus molecular cloud. The nebulosities seen surrounding the stars are the result of small dust particles in the vicinity of the stars reflecting stellar radiation. These images were taken by NASA Hubble Space Telescope (HST) in the near-infrared using NICMOS.

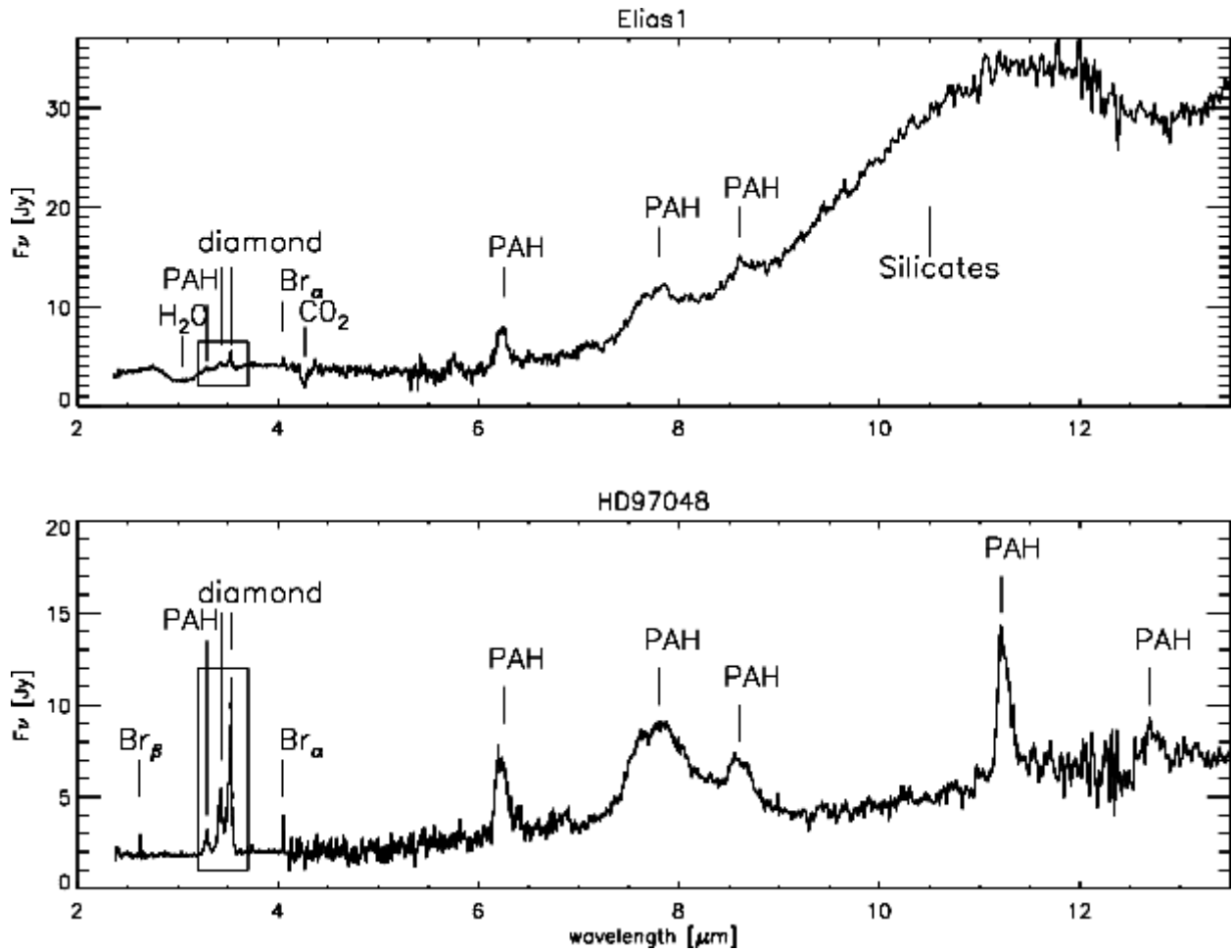


Figure 1-4. Infrared spectra of the HAeBe stars Elias 1 and HD97048. The emission features due to PAH and silicate emission are labeled. Figure from Van Kerckhoven et al. 2002

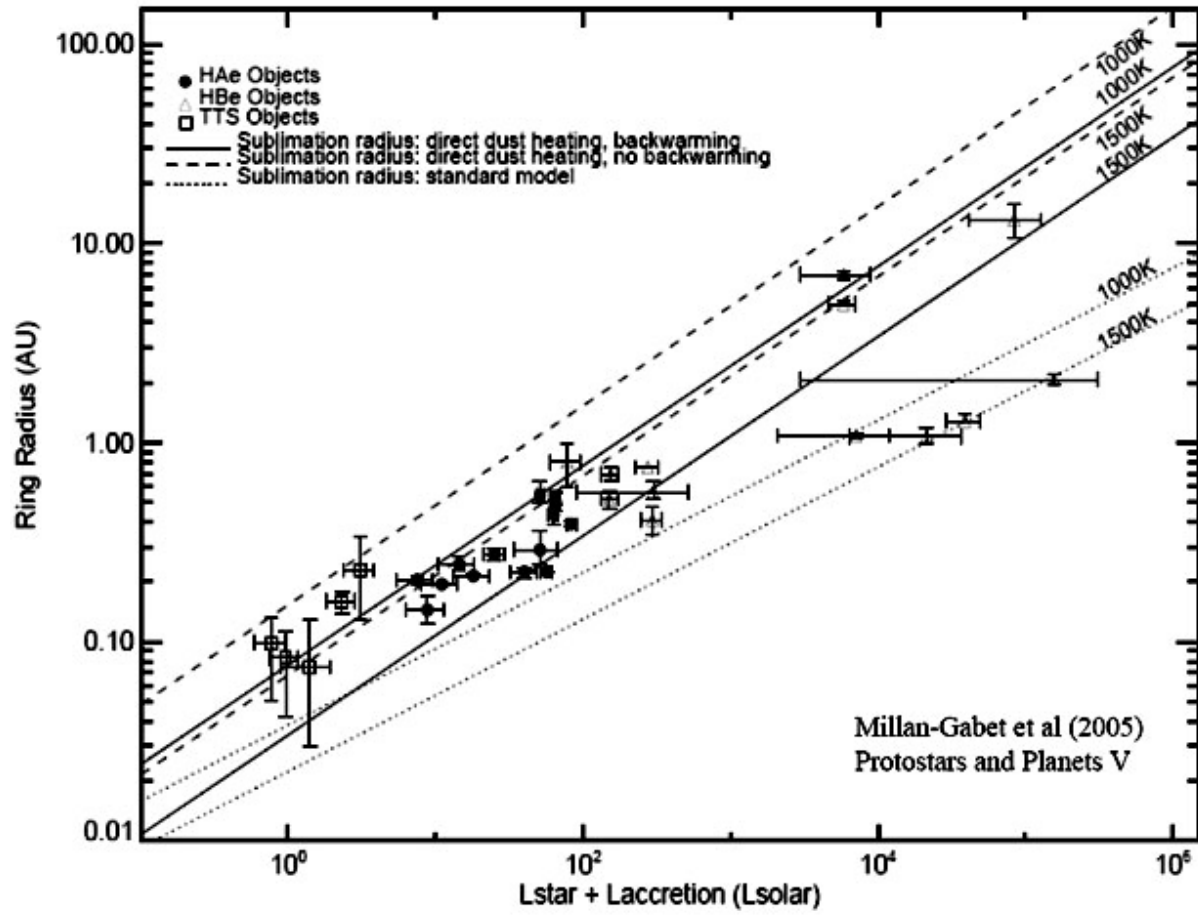


Figure 1-5. Size-luminosity correlation derived from near-infrared interferometric observations

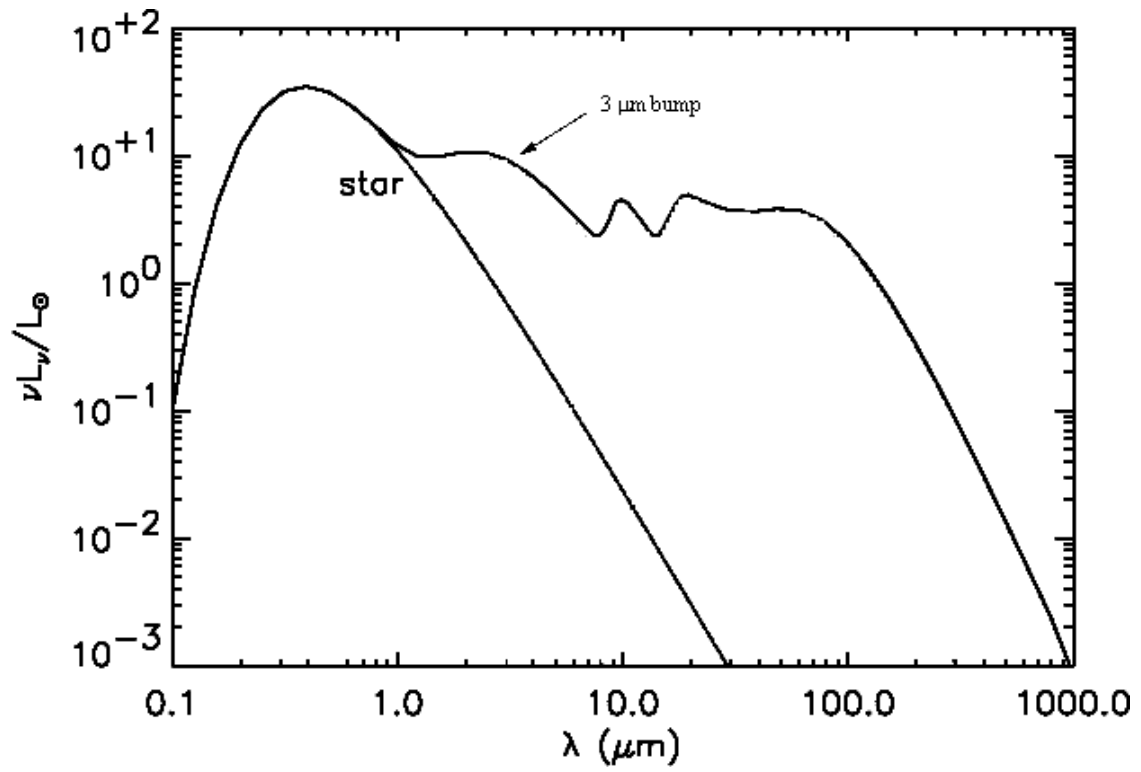


Figure 1-6. Typical spectral energy distribution (SED) of a HAeBe star. The figure shows the stellar contribution and the 3 μm bump.

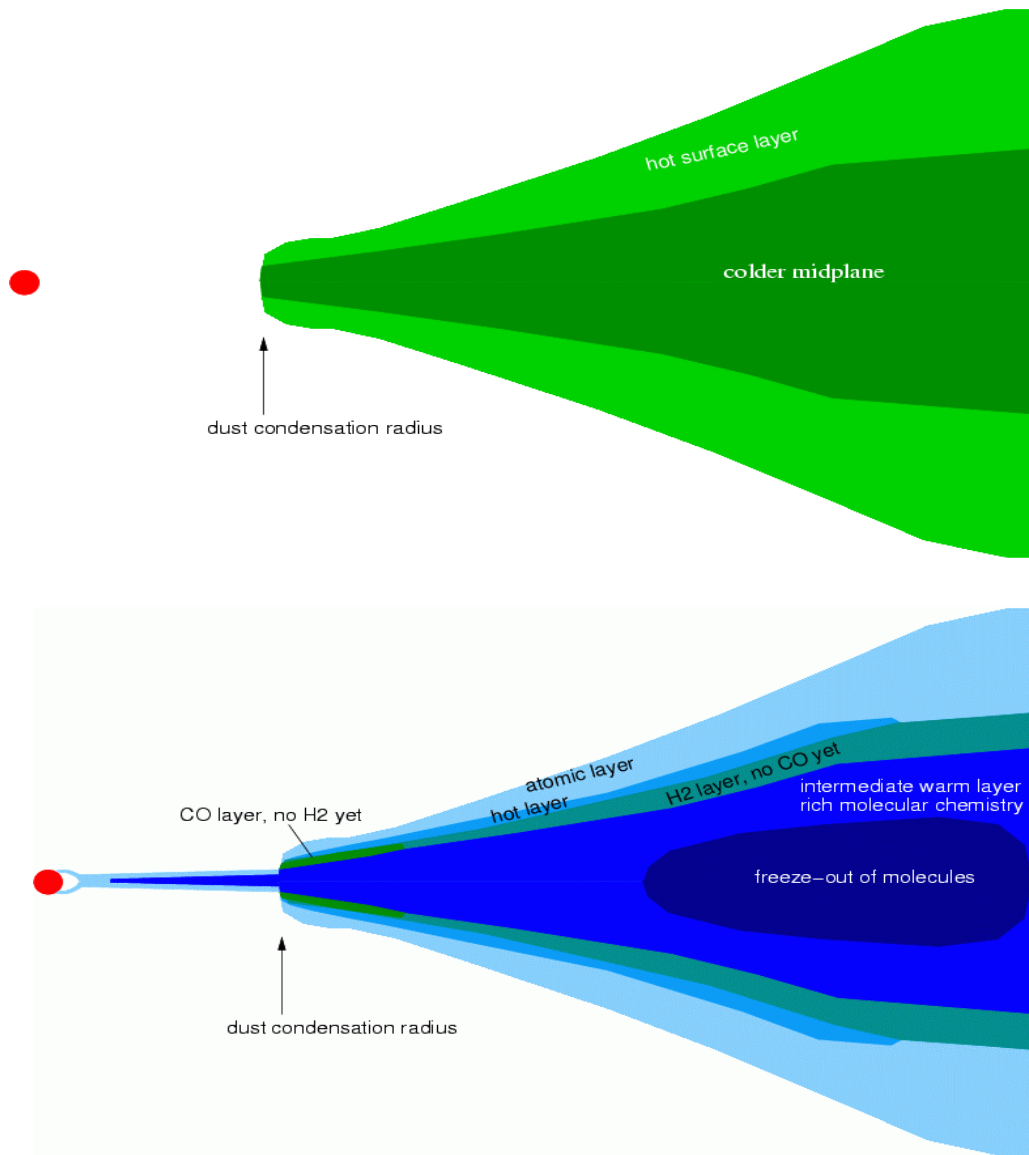


Figure 1-7. Schematic of the modified Chiang-Goldreich model developed by Dullemond (2001, 2004). The first panel shows the geometry of the dust in a flaring disk, the second panel shows the geometry of the gas component. The gas component can extend to the inner hole at the dust sublimation radius.

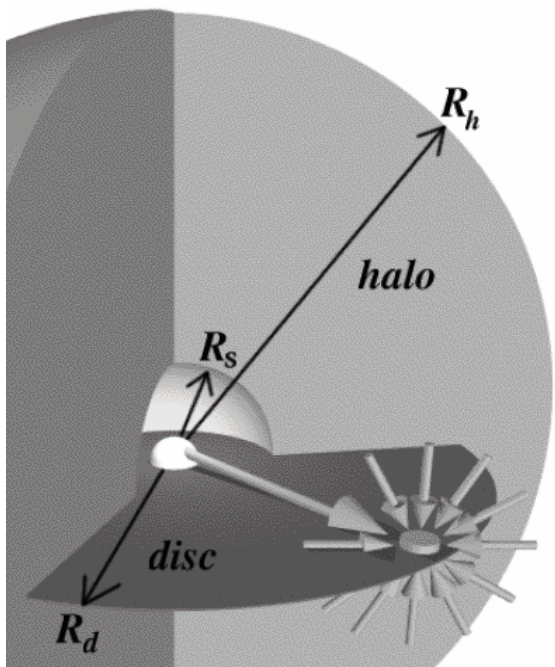


Figure 1-8. Schematic of the flat disk plus halo model described by Vinkovic et al. 2003 as an alternative to the Dullemond model

CHAPTER 2
MID-INFRARED INSTRUMENTATION, OBSERVATIONS AND DATA REDUCTION

Infrared Sky

Infrared radiation covers the region from 1 to 350 μm and is divided into three regimes: near (1 to 5 μm), mid (5 to 25 μm), and far (25 to 350 μm). Thermal emission is the principal source of this radiation and any object with a temperature above 0 degrees Kelvin emits in the infrared. Infrared astronomy allows the exploration of many different sources: cool red giants and star forming regions with temperatures in the 750 to 5000 Kelvin range in the near-infrared; planets, comets, asteroids, and dust around stars with temperatures from 100 to 1000 Kelvin in the mid-infrared; and very cold dust and molecular clouds with temperatures in the 10 to 100 Kelvin range in the far-infrared.

Many astronomical sources are only accessible to scientist in infrared wavelengths because they are embedded in dense regions of gas and dust that obscure the objects at shorter wavelengths, only becoming transparent at longer infrared wavelengths. In addition, objects that are too cool and faint to be detected at visible wavelengths, like planets and dust in circumstellar disks, can be detected in the infrared. Stellar radiation from stars of spectral type F or earlier will heat optically thin dust to temperatures above 100 K within hundreds of AU from the star; this warm dust will reradiate primarily in the mid-infrared part of the spectrum. At shorter wavelengths, the disk becomes invisible because radiation from the star overwhelms and hides it; however, at longer mid-infrared wavelengths radiation from the disk peaks, while radiation from the star decreases, making it possible to detect the disk.

Ground-Based Mid-infrared Astronomy

Atmosphere

The principal limitation in doing mid-infrared astronomy from the ground is the Earth's atmosphere, which emits and absorbs infrared radiation. Thermal background emission from the sky is primarily due to water vapor content, which is strongly related to ground temperature. More water vapor leads to higher atmospheric emission. Terrestrial thermal emission, which peaks in the mid-infrared, also contributes to the strong thermal background, limiting the sensitivity of ground-based observations. The atmosphere also absorbs mid-infrared radiation; Figure 2-1 shows the transmission curve from the atmosphere over these wavelengths. Regions with fewer absorption lines, high atmospheric transmission, are called atmospheric windows and most mid-infrared observations from the ground target these windows. In the 7-14 μm window, N band region, ozone is responsible for the strong absorption feature at 9.6 μm , while water vapor causes many of the absorption features in the 16-30 μm window, Q band region. Atmospheric transmission strongly depends on altitude; as altitude increases, the atmospheric absorption bands become narrower due to a reduction in pressure, and emission from the sky is slightly reduced due to a decrease in temperature. Therefore, good geographical sites for mid-infrared observations are located at high altitudes.

Another major problem for mid-infrared astronomy is the unstable nature of the sky background caused by microthermal turbulence and changes in water vapor and aerosol content on short timescales. This effect is called *seeing* and causes blurring in the images affecting the angular resolution of the observations. One way to measure the seeing is by measuring the full width at half maximum (FWHM) of a point source. The image of a point source as seen through a telescope is determined by diffraction. Light collected in the telescope lens interferes with itself

creating a ring diffraction pattern known as the Airy pattern. In the absence of atmosphere, the angular resolution of the image is only limited by diffraction and given by the *Rayleigh criterion*

$$\sin \theta = 1.22 \frac{\lambda}{D} \quad (2.1)$$

where θ is the angular resolution in radians, λ is the wavelength of the observation and D is the diameter of the telescope lens, or telescope aperture. However, when light from an astronomical source enters the atmosphere the parallel plane light waves are disturbed on small scales creating an additional blurring effect on the images. This effect is greater for small wavelengths. If less blurring is created by the seeing than is by diffraction on the telescope, the effect of seeing becomes irrelevant and the resolution of the observations is only limited by telescope aperture. However, mid-infrared observations from large ground-based telescopes are usually limited by seeing conditions. Figure 2-2 shows changes in the FWHM of a point source during observations at 11.7 μm (first column) and 18.1 μm (second column) taken from the Gemini 8 meter telescopes. The first row shows observations taken under very stable seeing. The second row shows observations taken under variable seeing.

Gemini Observatory

The identical Gemini telescopes are two of the largest and more advanced optical telescopes in the world and the first ones to be specially designed to work in the infrared. They use a combination of two single mirrors in a *Ritchey-Chrétien* configuration, Figure 2-3. This optical design is used in all professional telescopes since it offers the advantage of eliminating coma and spherical aberration, which can distort the image quality. The primary mirror is a single 8.1 m mirror only 21 cm thick and is coated with a protective silver layer to reflect infrared radiation more effectively while reducing the overall thermal emission of the telescope. Since the mirror is too large and thin to keep its shape, it is tuned by using active optics at the

beginning of each night and every few minutes throughout the night. Tuning of the mirror is done by splitting the light beam from a star and sending a representative part of the light to a wavefront sensor that calculates how far out of shape the mirror is. Around the edge and under the mirror, 180 computer-controlled actuators correct the deformation caused by gravity and temperature changes by pushing and bending the mirror until it is perfectly shaped.

While adaptive optics is used to tune the primary mirror, adaptive optics is used to minimize the effects of seeing in a process called *fast guiding*. A bright star near the science target is used as a guide star. Light from the star is sent to a wavefront sensor, which calculates the image distortion due to atmospheric seeing and the optimal position of the secondary mirror to reduce it. The simplest form of this correction is using the *tip-tilt* mechanism of the 1-m secondary mirror; the mirror position is adjusted around two axes so that the position of the guiding star remains fixed in the field of view. Since the seeing can change rapidly during a night, fast guiding continuously operates at a frequency greater than 10 Hz. The secondary mirror of the telescope is also used for chopping during mid-infrared observations as will be described in the next section, and is able to simultaneously do fast guiding and chopping.

Other features that make the Gemini Observatory optimized for infrared observations are the excellent geographical sites and the system's thermal controls. Gemini North Telescope, also known as Fred Gillet Telescope, sits on the dormant volcano Mauna Kea, Hawaii, at an elevation of 13,822 ft. The Gemini South Telescope sits on Cerro Pachon, Chile, at an elevation of 8,895 ft. These are considered the best sites currently in use for optical and infrared observations due to the stability of the seeing and atmospheric transparency. The system's thermal controls also help improve the image quality by keeping the telescope, its enclosure and optics at the same temperature as the environment, minimizing local self-induced seeing effects at the ground level.

Mid-infrared Instruments: Michelle and T-ReCS

After the telescope stabilize and correct the light beam using fast guiding, the beam is sent through a central hole in the primary mirror to the instruments. Michelle and T-ReCS are the mid-infrared imager/spectrometers in use at Gemini North and Gemini South respectively. Both instruments are optimized for low thermal background and provide excellent image quality.

T-ReCS was designed and built for the Gemini South telescope at the University of Florida. Figure 2-4 shows the path of the light beam inside the instrument and the different optical components:

- Entrance window: Environmental conditions, specially the percentage of humidity, and the wavelength of the observation determine the entrance window used for an observation. The entrance window filter wheel provides three interchangeable entrance windows: (1) KBr has a transmittance of 92% over the full mid-infrared wavelength range and emissivity of only 0.04%, making it the ideal window for infrared observations; however, the window is water soluble and not adequate for observing if humidity is high, (2) ZnSe has a transmittance $> 94\%$ and emissivity of 0.4%; this window is not water soluble but it has a small wavelength coverage (2.5-13 μm), and (3) KRS-5 has a transmittance of 70% over the full mid-infrared range, an emissivity of 0.3% and is not water soluble.
- Filter wheel: T-ReCS has two filter wheels. Observations for this thesis were taken using the Si-5, central wavelength 11.7 μm , and Qa, central wavelength 18.3 μm , filters. Figure 2-5 shows the transmittance pass-band for each of these filters.
- Detector: T-ReCs uses a Raytheon 320 x 240 Si:As block impurity band (BIB) detector that covers the wavelength from 5 to 28 μm . It is the largest mid-infrared detector currently in use. The pixel size is 50 μm . When used at the Gemini telescope, the pixel scale is 0.089 arcseconds for a total field of view of 28.4 x 21.1 arcseconds. The detector is made of 16 independent channels of dimensions (20 x 240 pixels). The signal of each channel is read from the bottom in a consecutive order.

During operation, filter changes and telescope movement generate heat inside the instrument. The temperature at which the array sensitivity is maximized is maintained using a closed-loop temperature control system. T-ReCS is mostly a reflective instrument and all the mirrors used are coated with gold to increase their reflectivity.

Michelle, the mid-infrared instrument currently in use at Gemini North, was built for United Kingdom Infrared Telescope (UKIRT). The instrument has the same array as T-ReCS and similar filters. The transmission band pass of the Si-5 and Qa filters used to collect the data for this thesis are also shown in Figure 2-5. Michelle only has one entrance window made of Potassium Bromide (KBr), so it is only used in low humidity.

Observing Technique: Chop-Nod

Despite all the care taken to optimize the instruments and telescopes for mid-infrared observations, there is still higher background mid-infrared radiation compared to the radiation we get from the science targets. To eliminate this excess emission, mostly due to the sky, and locally to the telescope and entrance window to the instrument, a technique called *Chop-Nod* is used. First the telescope is pointed at the target in the sky and a set of images is taken. The images will contain mid-infrared radiation from the target superimposed on the large mid-infrared radiation from the sky and radiation from the camera-telescope system. The frame time of these observations is very small, ~ 10 ms; otherwise, the detector will saturate due to the high background radiation. Then, the secondary mirror of the telescope moves slightly away from the target source, and another set of images is taken. These images contain only mid-infrared radiation from the sky in the vicinity of the source and from the telescope-camera system. The telescope's secondary mirror will move from the target plus background position, or *on-source* position, to the only background position, or *off-source* position, at a frequency of 3-10 Hz. This procedure is called chopping. During a *chop cycle* mid-infrared radiation from the sky is effectively removed from the images; however, because the position of the telescope's secondary mirror changes during the cycle, the path the light travels to reach the detector is slightly different for the on-source and off-source positions and the radiation from the telescope-instrument system is not effectively removed. The excess emission left after chopping is called

radiative offset. In order to remove radiative offset, the entire telescope is moved so that the position of the source now appears where the only-sky position was previously, and the only-sky position appears where the on-source position was. This movement of the entire telescope is called nodding and occurs over a time frame larger than chopping, a few tens of seconds. Position 1 is called *nod A* and position 2 is called *nod B*. In nod B position, the chop cycle is repeated, and the radiative offset of the new differenced images will be the negative of the one obtained in nod position A. By combining the differenced images from the two nod positions, the radiative offset is effectively cancelled leaving only the mid-infrared emission from the target.

Figure 2-6 shows a standard chop-nod cycle. The figure was created using images obtained with OSCIR at the Infrared Telescope Facility (IRTF). OSCIR is the University of Florida infrared camera used to test the mid-infrared performance of the Gemini North and South telescopes during commissioning of the telescopes.

Output Data Files Structure

The output data files for Michelle and T-ReCS are multi-extension Flexible Image Transport System (FITS) files. The primary header, a text file containing all the parameters and information used during the observation, is contained in extension 0 of the multi-extension fits file. The remaining file structure is determined by which method is used to collect the data (the chop-nod technique was used for the observations included in this thesis) and how the data is saved in the two systems. Since the two instruments work in somewhat different ways, the resulting file structure is slightly different. In Michelle output data files, each extension contains the image data for a single nod position. All the images taken during a chop cycle at each nod position are contained within an extension. As a result, the number of extensions in a Michelle data file equals the number of nod positions used in the observation. In T-ReCS, each nod-cycle is divided into multiple savesets of about 10 ms, which contain the co-added chopped frames

taken during that time. Each of the savesets is written into a different plane of the file extension for that nod. There are usually 3 savesets per nod position. Therefore, T-ReCS raw data files can be broken down into smaller sub-sets.

The nodding sequence for Michelle and T-ReCS observations is also different. During a chop-nod cycle taken with Michelle, the telescope will move through positions ABBA. The observations will start at nod position A, then go to nod position B, where two chop cycles will be taken, returning afterwards to nod position A. During a T-ReCS chop-nod cycle, the observations will start at nod position A, then move to nod position B, then move back to nod position A, and then move back to nod position B. The sequence for a T-ReCS nod cycle is ABAB.

Output Image Spurious Structure

The resulting image for each observation is a compilation of the many images produced during the total number of chop-nod cycles taken during the observation. On occasions, the resulting image will present distortions produced by non-perfect tuning of the primary mirror or fast guiding of the secondary. The image can also present spurious structures related to the detector. The data collected for this thesis was one of the first science observations taken with the newly commissioned telescopes and instruments, and, as a result, the Observatory was still correcting some of these problems. I only see image distortions due to telescope operations from Gemini South observations taken in 2004. Figure 2-7 (A) shows some of these image aberrations: the trifoil shape of the stellar image due to astigmatism caused by imperfect tuning of the system, and an elongated structure across the image, probably also due to the telescope's imperfect tuning.

Another problem with the output images is detector *crosstalk*. Fig 2-7 (A) also shows spurious structures along rows and columns, which are characteristic of the detector response

when imaging very bright sources. The dark row centered on the source is due to a drop of the signal along all channels and also shows *ghost* images of the source. The drop is only a few tens of a percent of the peak emission of the stellar source and becomes obvious only in observations of very bright sources. The image is presented in a logarithmic scale to emphasize the low level structures. Since both Michelle and T-ReCS use the same detector, this image structure is present at different degrees in all the observations. Since the effect is seen across the whole array and is to some extent uniform, finding the median value along the rows for a range of columns with only sky emission significantly reduces it.

The same method can be used to eliminate electronic noise in the images, which shows up along columns and rows in the array. To clean the images, I modified an Interactive Data Language (IDL) routine written by James M. De Buizer to create an image of the noise based on the median value along columns and rows in the array. This image of the noise was then subtracted from the images. Figure 2-7 (B) shows the resulting improved image after noise subtraction.

Data Reduction

In this section I describe the data reduction procedures used to prepare the output images from the detector for scientific analysis. The following steps are standard for mid-infrared astronomy:

1. Cross-correlation
2. Flat fielding
3. Sky subtraction
4. Standard star calibration and airmass correction
5. Photometry
6. Color correction

Image Cross-Correlation

Cross-correlation of the images, a useful technique to correct positional drift of the source in the array due to tracking errors or imperfect fast guiding, was unnecessary for the data included in this thesis. I looked at the data sets of all the images before stacking them into a final image and measured the central position of the source in the array. Due to the excellent quality of the Gemini Observatory, no drifts of the sources were observed in the images obtained for this thesis and I was able to stack all the data subsets for each source to obtain a final image.

Flat Fielding

Flat fielding is another standard routine used in the processing of astronomical images and corrects pixel-to-pixel variations in the detector array. The mid-infrared arrays used in Michelle and T-ReCS are very flat, especially in the central region where the targets are centered. Since taking flats for flat fielding involves more observing time and the non-uniformity in the array is very small, the Gemini Observatory does not offer the option of doing flat fielding. Thus, no flat-fielding correction was applied to the data.

Sky Subtraction

Even after chop/nod there is sometimes residual background radiation in the images making the mean radiation from the sky different from zero. Eliminating this residual emission was the first step taken in reducing these data. The procedure used in all images is as follow:

- The image source was masked and the area in the perimeter of the source divided into four regions (top, bottom, left, right)
- For each region the mean sky value (total count in the region divided by the number of pixels in the region) and the standard deviation associated with the mean (sample standard deviation, σ_{px} , divided by the square root of the number of pixels) was calculated.
- The four sky regions were combined and a combined mean sky value calculated.
- The mean sky value was then subtracted from the image to effectively remove the residual sky emission.

Standard Star Calibration and Airmass Correction

Photometric calibration is the process of converting Analog Digital Units (ADU/sec/px), the flux units in the final detector image, into a physical flux density unit, in the case of this thesis: Janskys, Jy. These observations were calibrated using mid-infrared standard stars. For observations taken at Gemini North, the Gemini scientist overseeing the observations decided which standard stars were observed on any given night. For some of the observations taken at Gemini South, I was requested to provide specific standard stars to go with my observations. All the standard stars were selected from two different lists of mid-infrared standards: (1) Mid-infrared calibration standard stars compiled by the European Southern Observatory (ESO) with accurate mid-infrared photometry from Thermal Infrared Multimode Instrument (TIMMI 2) and (2) Cohen et al. (1999) mid-infrared standards. In the cases when Cohen (1999) standard stars were used, I calculated the flux densities for these star from the spectral models provided by Cohen. Only two observations of standard stars at each filter were taken along with each observation.

Once I know the expected flux density of the standard at the filter central wavelength, I need to find calibration values. Since the mean sky is already zero, this is a straightforward procedure. I used a circular aperture to measure the ADU/sec/px in the image of the standard star and divided the expected flux by that value; the ratio of the two is the calibration value for that observation. The calibration value is an indicator of the photometric quality of the night. The error associated with the flux measurement in the images, $\sigma_{px} \sqrt{n_{px}}$, where n_{px} is the number of pixels included in the aperture, is much less than the 10% standard error associated with photometric calibration in the mid-infrared; therefore, I assume the typical 10% error for the calibration values.

Under ideal conditions, the calibration value will be the same for all stars observed at the same *airmass*. Airmass is a measure of the thickness of the atmosphere that light from an astronomical source has to cross to get to us relative to the zenith and is defined by $\text{Airmass} = \sec(z)$, where z is the angle of the observation from zenith. To reduce the negative effect of the atmosphere on the observations, it is desirable to take observations at an airmass close to 1. All the sources in this survey were observed at airmass < 1.5 . In reality, the airmass correction needed in the mid-infrared is very small. To include airmass correction, standard stars are observed at different airmasses throughout the night with each filter so that the airmass of the science target can be matched to the airmass of a standard star. Since this procedure adds a significant amount of time to each science target observation, airmass correction was not applied to the images. In all these observations, the calibration values obtained from the two standard star observations at each filter were almost the same.

Photometry

Once the calibration value for one observation is known, I need to multiply the science target image by that value so that the flux density is in Jy/px. A circular aperture is placed over the source to measure the total emission from the source. The size of the aperture was decided on upon inspection of each image to include all flux from the source and as little sky as possible. The error associated with this measurement is again dominated by the 10% error in the calibration value.

Color-Correction

Color correction is important for flux density measurements, because the SED of stellar sources used as standards and the SED of the science targets have different shapes and therefore different colors over the filter bandpass. Color correction depends not only on the shape of the SED of the two objects, but also on the central wavelength and bandpass of the filters. The effect

is larger for wide band filters. In this thesis, only narrow band filters were used; however, there is still a small error associated with color-correction.

Most of the standards used in this thesis are spectral type K or M with effective temperatures in the range of 3000 to 5000 K. These sources were selected to avoid using the very bright stars that saturate the detector; however the A0 star Sirius with a temperature of 9,500 K was also used in some observations. The SEDs of these sources peak in the optical and have a steep decline dominated by the Rayleigh-Jeans law, $f(\lambda) \propto \lambda^{-2}$, in the mid-infrared. On the other hand, the SEDs of the target sources are very flat at this wavelengths because they are dominated by grain dust emission with temperatures of ~ 100 -300 K that peak in the mid-infrared.

The color correction method assumes that

$$\frac{ADU_P}{ADU_S} = \frac{N_{\gamma P}}{N_{\gamma S}} \quad (2.2)$$

where P stands for photometric standard, S for science target, and N_{γ} is the number of photons received at the detector. The number of photons is given by

$$N = \int_{\nu_1}^{\nu_2} \Omega_{\text{sys}} \frac{F_{\nu}}{h\nu} d\nu \quad (2.3)$$

where ν_1 and ν_2 are the frequency limits of the observation, h is the Planck's constant and F_{ν} is the flux density of the source through the filter bandpass. The flux density depends on the solid angle of the observation, Ω , the optical depth, τ_{ν} , and the Planck function as a function of temperature, $B_{\nu}(T)$,

$$F_{\nu} = \Omega(1 - e^{-\tau_{\nu}})B_{\nu}(T) \quad (2.4)$$

and Q_{sys} is the system quantum efficiency which depends on the transmission of the atmosphere, T_{atran} , and the filter, T_{filter} , and on the quantum efficiency, QE, of the detector at the desired wavelength

$$Q_{sys} = T_{filter}(\lambda)T_{atran}(\lambda)QE(\lambda) \quad (2.5)$$

Combining the previous equations, I can write the number of photons in terms of a monochromatic flux density $F_{\nu o}$

$$N = \frac{F_{\nu o}}{(1 - e^{-\tau_{\nu o}})B_{\nu o}(T)} \int_{\nu_1}^{\nu_2} \frac{Q_{sys}(1 - e^{-\tau_{\nu}})B_{\nu}(T)}{h\nu} d\nu \quad (2.6)$$

and relate the number of photons received from the program source to the counts measured in ADU by using the first equation in this section. Approximating the standard star by a blackbody, the opacity term for that side of the equation disappears. Then I can write the monochromatic flux density for the science source as a function of the ratio of the flux density to the counts measured for the standard star, which is the calibration value, multiplied by the counts in ADU measured for the source, and a color correction term. The calibration value multiplied by the source counts is the calculated flux density for the source and the color correction from the previous derivation is

$$color - correction - term = \frac{\int Q_{sys} \frac{B_{\nu}(T_s)}{\nu B_{\nu o}(T_s)} d\nu}{\int Q_{sys} \frac{(1 - e^{-\tau_{\nu}})B_{\nu}(T_p)}{\nu(1 - e^{-\tau_{\nu o}})B_{\nu o}(T_p)} d\nu} \quad (2.7)$$

Color correction was done using a MATHCAD program written by Dr. R. K. Piña. The input parameters are the calculated flux density and filter properties. The code iterates to solve for temperature, opacity and color correction. Since the filters used in this thesis are narrow band

filters, the color correction for all sources using the previously outlined procedure is very small, less than 1 % for the Si-5 filter and less than 4% for the Qa filter. Therefore, the color corrected flux measurements are within the photometric errors.

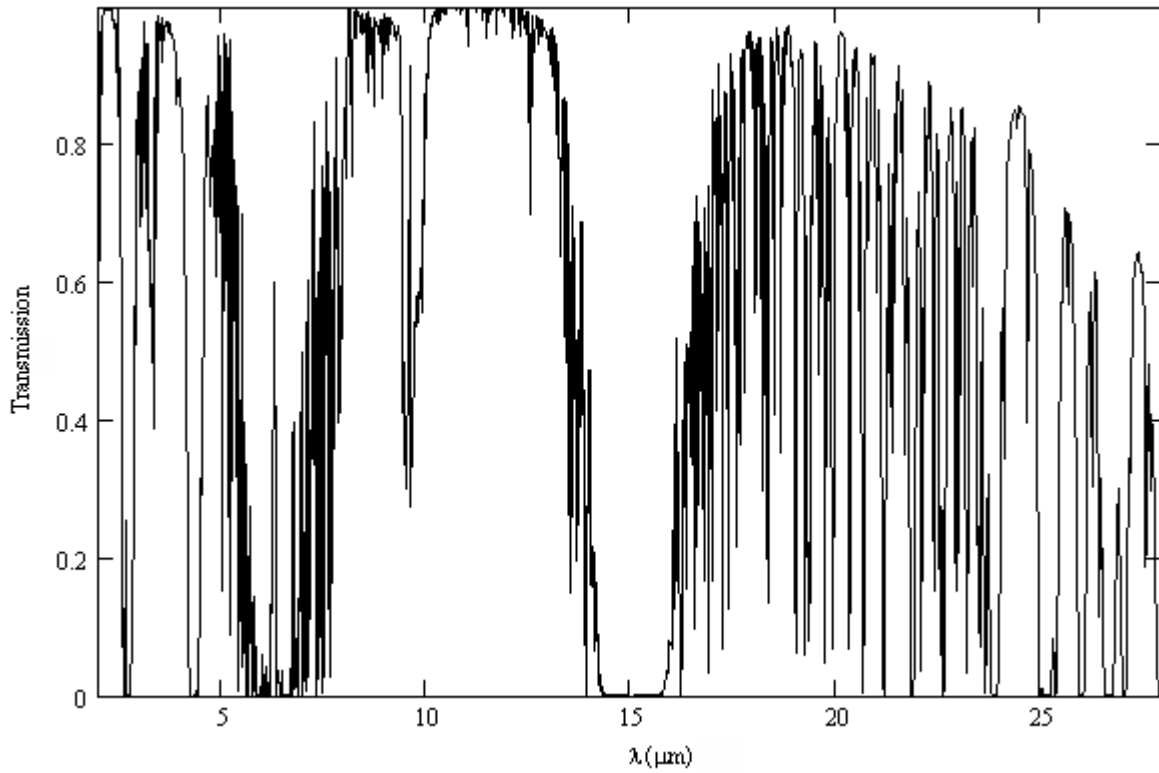


Figure 2-1. ATRAN model of atmospheric transmission for Mauna Kea. The absorption feature at 9.8 μm is due to ozone.

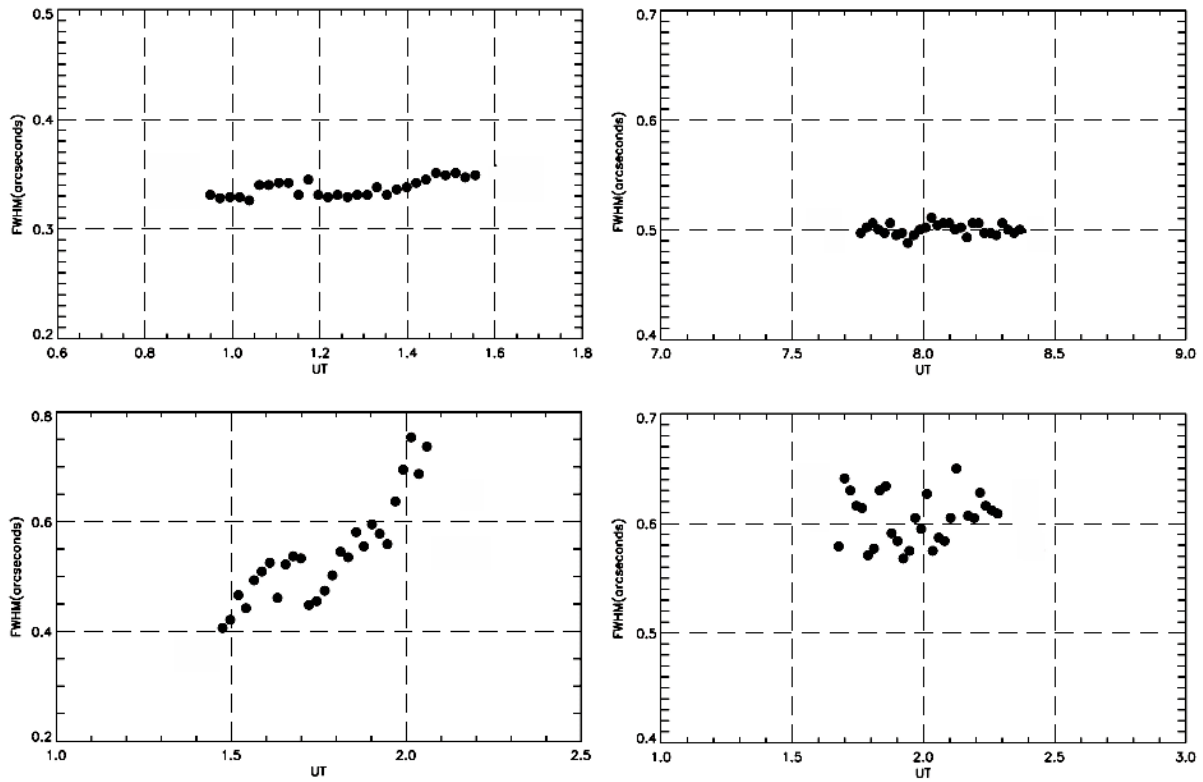


Figure 2-2. Full width at half maximum measurements as a function of Universal Time. The first row shows observations taken under stable seeing. The second row shows observations taken under variable seeing. The $18.3 \mu\text{m}$ observations are less affected by seeing because of the larger wavelength. Both sets of observations were taken as part of this thesis data at Gemini South telescope using T-ReCS.

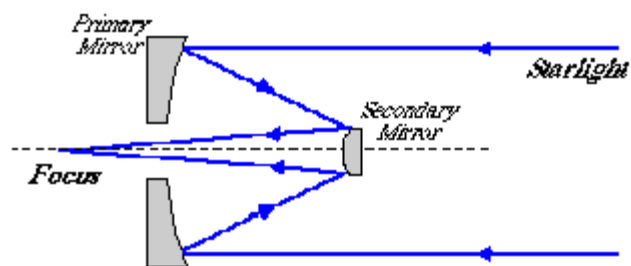


Figure 2-3. Optical design for a Ritchey-Chretien telescope.

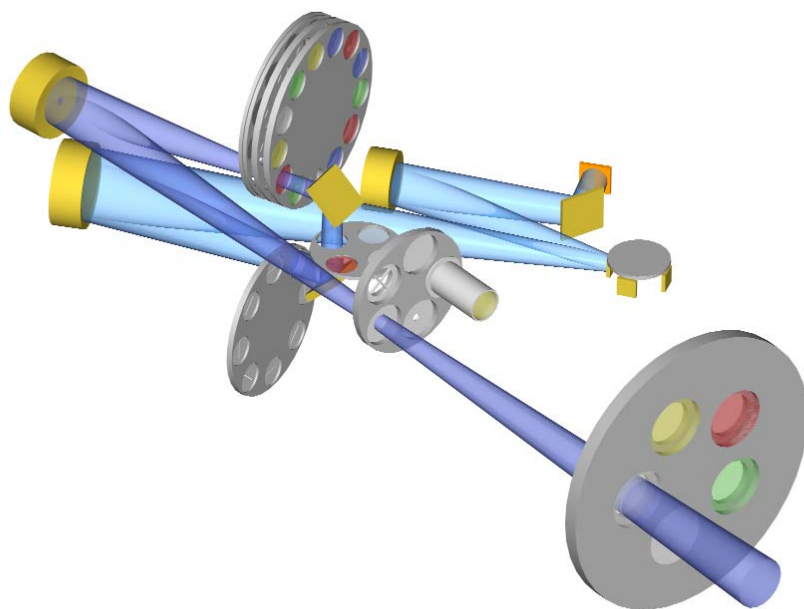


Figure 2-4. T-ReCs optical design

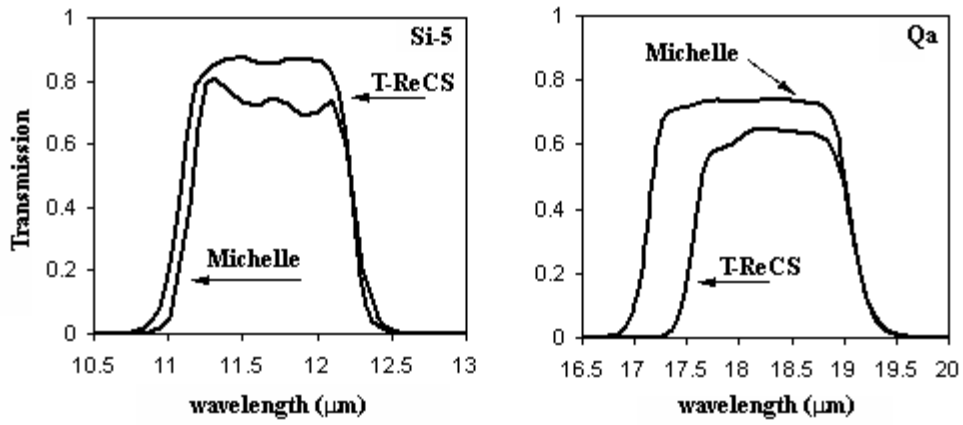


Figure 2-5. Filter transmission for T-ReCS (blue) and Michelle (magenta)

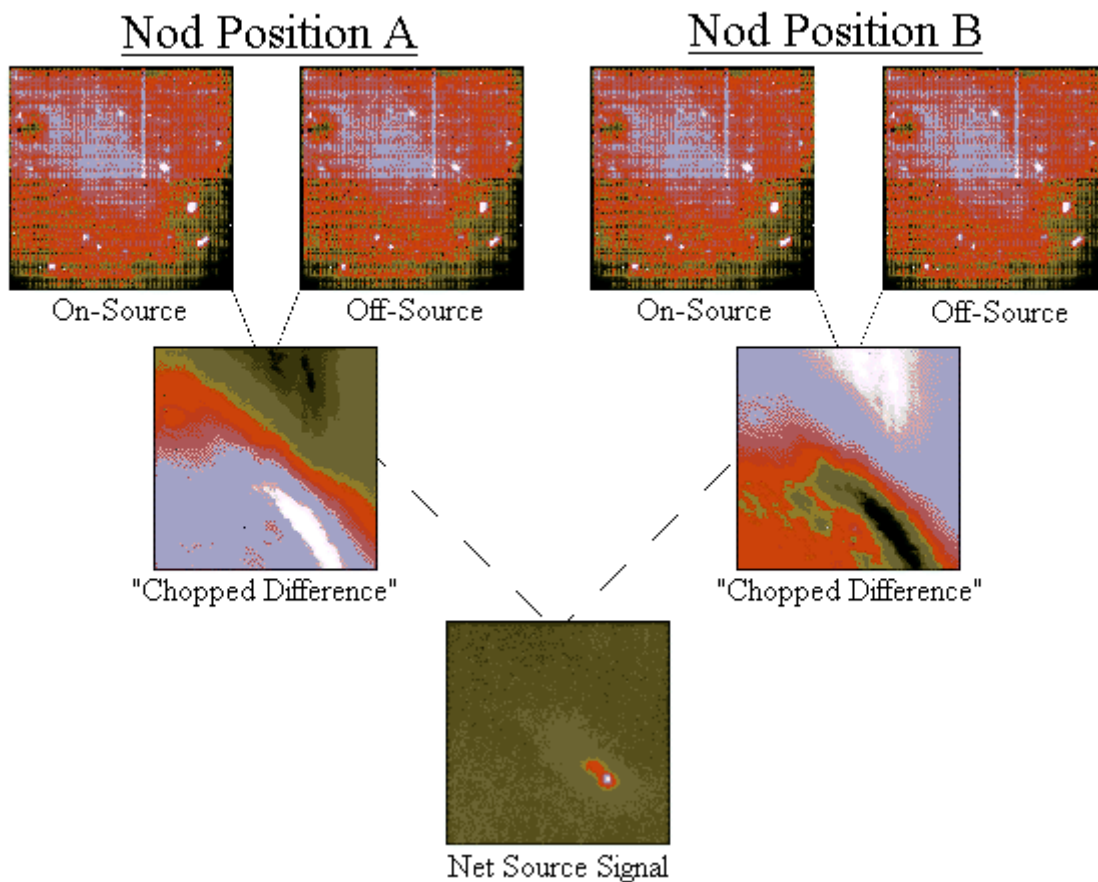


Figure 2-6. Chop-Nod strategy. The top four images are the raw co-added images at each chop position. The target source is not seen on the on-source images because emission from the source is small compared to sky emission, which dominates the mid-infrared radiation observed. The middle row shows the resulting images after subtraction of the off-source images, removing the contribution from the sky. These two images, called dif frames, are the negative of each other and show the large radiative offset due to the telescope-camera mid-infrared emission. The bottom image is the result of combining the two dif frames and mid-infrared radiation from the astronomical source dominates the final image. This image was taken with OSCIR at the IRTF and is part of the OSCIR operation manual.

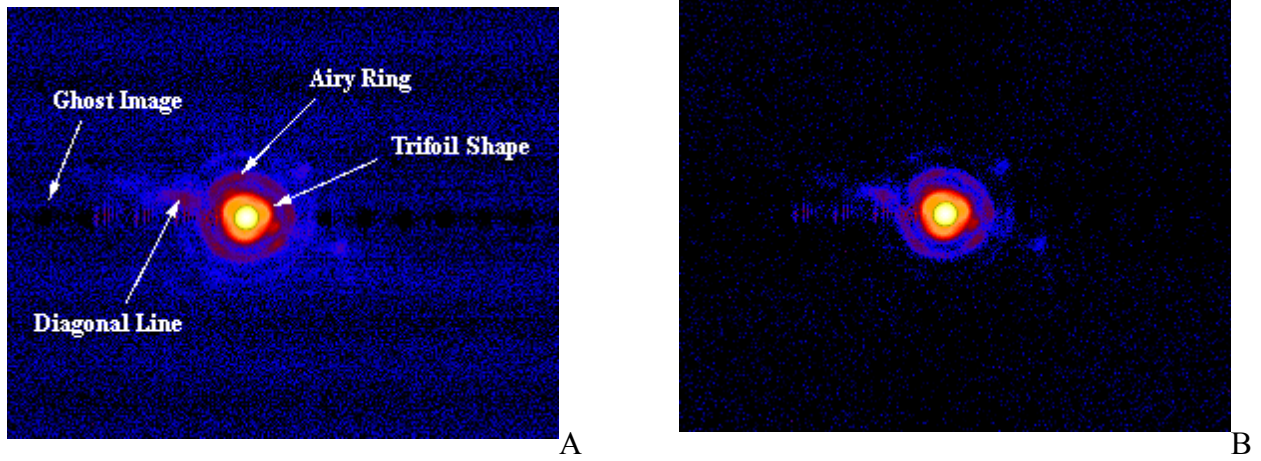


Figure 2-7. Spurious structure in the images. The image on the left shows image structure due to diffraction (airy ring), imperfect tuning (trifoil structure and diagonal line across the source), detector response to bright sources (ghost image across array), and electronic noise (horizontal banding noise). The image on the right shows the improved image after implementing the noise mask routine. Non-uniform structures are still present.

CHAPTER 3 SOURCE SAMPLE AND DATA ANALYSIS

Herbig Ae/Be Sample

We selected all targets for this survey (except one, HD97048) from the list of optically visible Herbig stars by Malfait et al. (1998). The sources were selected by matching the positions of stars in the Smithsonian Astrophysical Observatory (SAO) Star Catalogue and stars in the IRAS point source catalogue. An advantage of this selection is that this sample should not include any of the heavily obscured very young systems and I can concentrate on the sources that have evolved beyond the embedded stage. A drawback of the selection criteria is that the sample also excludes stars with disks orientations far from face-on where the star is obscured by dust in the disks, and the appearance of face-on disks is difficult to distinguish from spherical halos. All 20 objects were chosen to be within 500 pc, with 17/20 objects being within 300 pc, to ensure the ability to spatially resolve the circumstellar structures in these systems. Many of the sources in the target list have been shown to have extended CS dust from studies at other wavelengths.

Calculating Stellar Properties

Determination of stellar parameters and evolutionary states is limited mostly by the accuracy of stellar models. The morphology of the stellar tracks from different stellar tracks codes (Baraffe et al. 1998, BCAH code; Charbonnel et al. 1999, Geneva code; Siess et al. 2000, Grenoble code) largely depends on the different physics, convection, surface boundary conditions, that goes into the codes. However, for stellar masses above 1 solar mass and ages of more than 1 million year, the regime of interest for us, all the stellar tracks are very close to each other.

Spectral types, effective temperatures and luminosities of all the target sources were taken from the literature (Acke et al. 2005, van den Ancker et al. 1998, van Boekel et al. 2005, Pietu et

al. 2003, Jura et al. 2001, Hamaguchi et al. 2005, and Moth et al. 1997). I then used those stellar parameters and assumed solar metallicity ($z=0.02$) to derive stellar masses and ages for all the sources in the survey by using the stellar PMS evolutionary tracks of Siess et al. (2000). To check the accuracy of the calculated stellar parameters, I compared the derived parameters for the very well studied Herbig Ae star AB Aurigae to other published results. The parameters I derived were within the range of published values found in the literature for this source. An overview of the stars in the sample, some of their properties, and calculated stellar parameters are given in Table 3-1.

An H-R diagram for all the sources, Figure 3-1, shows the majority of the sources along evolutionary tracks for PMS stars with masses between 1.7 and 7 solar masses. Most of the stars in this study are approaching the zero age main sequence line, reinforcing the idea that they have probably dissipated most of the original envelope material. However, the classification of two of the sources as young stars and therefore candidate Herbig Be stars is questionable. The star HD41511 is thought to be a binary system with an M type companion star and its position in the H-R diagram well above the main sequence has been interpreted as evidence of its post-main-sequence state (Welty and Wade 1995). The star HD50138 is also a suspected binary system (Cidale et al. 2001), and it has been classified in multiple studies as a classical B[e] star.

Photospheric Emission

Flux densities measured from the images contain emission from the stellar photosphere and thermal emission from dust grains around the star. Since the main objective of the study is to investigate the properties of the mid-IR emission from the dust, I need to isolate this emission by removing the photospheric component of the emission.

Two different methods were used to estimate the stellar contribution to the source fluxes derived from the observations. First, I used the spectral type of the star and its effective

temperature from table 3-1 to select the appropriate stellar atmosphere model using the PHOENIX/NextGen grid of models developed by Peter H. Hauschildt for M dwarf stars of solar metallicity. This model includes over 500 million atomic and molecular lines and treats stellar structure as a sphere instead of using the parallel plane approximation. As a simpler alternative, I used the effective temperature of the sources and approximated the stellar photosphere by a blackbody function. Since I was only interested in the mid-infrared contribution, the blackbody approximation also gives an accurate estimate of the stellar flux. I then used photometric measurements in the optical UBV bands to scale the models. The average ratios of the U_o/U_m , B_o/B_m , V_o/V_m , where o stands for observed and m for modeled, were used to calculate the scale value and normalize the model atmosphere.

From the normalized atmospheric model, I found the expected atmospheric fluxes at the wavelengths of the observations. These fluxes were then subtracted from the total fluxes to obtain the dust emission contribution. Figure 3-2 shows the stellar atmospheric model and the blackbody approximation, both normalized to the UBV fluxes for one of the sources. The derived mid-infrared fluxes are identical using either of the two approximations. Since I did not have a theoretical computation model atmosphere matching the effective temperature of all the sources from NextGen, I only used photospheric fluxes derived from the blackbody approximation when the NextGen model was not available.

For all the sources studied in this survey, stellar fluxes were negligible when compared to the total flux of the system. Mid-infrared emission in these objects is dominated by dust emission.

Line Emission

In addition to correct the fluxes for photospheric emission, I also corrected the 11.7 μm fluxes for silicate and PAH line emission. I used the available line fluxes from Acke and van den Ancker (2005) to estimate the contribution of the 11.2 μm PAH emission line and the 11.3 μm silicate emission band to the fluxes calculated from the observations since these emission lines are within the Si-5 filter bandpass. For all the sources with line flux information, the line flux was subtracted to leave only the contribution from dust thermal emission at this wavelength.

Classification of sources

For consistency with the literature I have classified all the sources into the Group I/Group II classes as defined by Meeus et al. (2001). I used near-infrared photometry in the JHKLM filters (Malfait et al. 1998, Hillenbrand et al. 1992) to calculate near-infrared luminosities, and flux densities at 11.7 and 18.3 μm from the observations to calculate mid-infrared luminosities and mid-infrared colors [12]-[18]. This differs from previous classifications in that I am using the mid-infrared fluxes derived from the observations presented in this work and not IRAS fluxes. The resulting graph is shown in Figure 3-3. Only two sources have different classifications than in the literature. HD34282 has been previously classified as a Group I source; however, I classify this object as a Group II source based on the photometry presented here. The star HD150193 also falls under a different classification. It has been previously classified as a Group II source. Based on the fluxes derived from the observations presented here, HD150193 would be a Group I object. However, the Si-5 observations of this source were taken under unstable conditions, with seeing variations as large as 0.4 arcseconds, and I cannot evaluate the photometric errors during that night since only one observation of a standard star was taken. Given the uncertainties associated with the Si-5 photometry of this object and the lack of

nebulosity around the source that could compromise the IRAS measurements, I have kept the Group II classification for HD150193.

Source Sizes

The accurate measurement of angular diameters of partially resolved sources is a long-standing problem. Nevertheless, very few papers have been published on this subject. In this section I describe the systematic approach I followed to measure sizes of the target sources.

Point Spread Function

The image of a point source on the detector is not a point; because of diffraction the observed image is a convolution of the intrinsic source and the instrumental profile or point spread function (PSF). The PSF can be determined by observing a main sequence star close to the program star on the sky before and after each observation of the program star. It is important for the observations of the PSF and science star to be close in the sky and in time so that observing conditions for the two are as similar as possible. Since these main sequence stars are point sources without extended structure, the resulting image profile is a reflection of the instrumental profile and seeing conditions relevant to the program star.

All PSF stars for the survey were selected from the Positions and Proper Motions (PPM) Star Catalogue. I constrained the list to include only stars of spectral types K or M, brighter than $V = 6$, and located within 5 degrees of the program star in the sky. One of the problems I encountered early on with the observations of PSF stars was that although they were bright at visible wavelengths, they were faint at mid-infrared wavelengths. Since observations of PSF stars are taken with short integration times, the resulting PSF image had low signal to noise ratio for the desired analysis. In an effort to correct this, all PSF stars for subsequent observing runs were correlated with IRAS point sources. Selected sources from the PPM catalogue with no flux measurement in the IRAS catalogue or with low flux density at 12 and 25 μm were discarded.

Very bright mid-infrared sources were also discarded to avoid image distortions due to detector crosstalk. This step significantly improved the PSF star observations.

Moffat Function

Another blurring effect on the images that I have not mentioned previously is due to pixels on the array. The image registered on the detector is broken down into pixels and each pixel act as a boxcar function so that the signal from each pixel is a constant. The resulting effect can be seen if one zooms in the image; instead of having a smooth source profile, one finds sharp edges. For slowly changing regions of the source profile, interpolation can be used to break the original pixels down into smaller pixels. New data points are created by smoothly blending the signal from pixel to pixel. However, pixelation is more difficult to correct for sharp regions of the profile, with only one or two pixels covering the whole region. In this case, an alternative method is to model the source profile using a well behaved mathematical function.

Two widely used functions to model stellar profiles in astronomy are the Gaussian function and the Moffat function (Moffat 1969). The Moffat function provides a better fit to source profiles especially on the wings of the profile, where a Gaussian function decays faster. The Moffat function is given by

$$I(r) = \frac{\beta - 1}{\pi \alpha^2} \left[1 + \left(\frac{r}{\alpha} \right)^2 \right]^{-\beta} \quad (3.1)$$

and in the limiting case where $\beta \rightarrow \infty$, it is identical to a Gaussian function. Figure 3-4 shows the normalized profile of a Gaussian and Moffat functions with different β values, the smaller the β value, the larger the wings of the profile.

The presence of wings in all the sources makes the Moffat function an excellent choice to model PSF and science targets, and recover the stellar profiles without the effect of pixelation. I

used the IDL code mpfit2dpeak created by Dr. Craig B. Markwardt and publicly available at (<http://cow.physics.wisc.edu/~craigm/idl/fitting.html>) to model the profiles.

Measuring Sizes

In order to extract meaningful sizes for the system, it is necessary to deconvolve the observed image and the PSF, especially if the profiles of the science target and PSF star are similar. The problem with deconvolution is that it is a complicated technique and the results strongly depend on the assumptions made and the method employed. As a simpler alternative, I have chosen to deconvolve the observed sizes at the FWHM by using quadrature subtraction of the observed source diameter, Φ , and PSF diameter, Φ_b . The deconvolved diameter, Φ_d , and the error in the size, σ_{Φ_d} , are then given by:

$$\Phi_d = \sqrt{\Phi^2 - \Phi_b^2} \quad (3.2)$$

and

$$\sigma_{\Phi_d} = \frac{\sqrt{(\Phi \sigma_{\Phi})^2 + (\Phi_b \sigma_{\Phi_b})^2}}{\sqrt{\Phi^2 - \Phi_b^2}} \quad (3.3)$$

At the FWHM level, all the sources diameters are very close to the PSF diameters. Since I integrated longer on the sources than on PSF stars and integration time can influence the image profile, especially due to changes in the seeing during the observation, I divided all the images for HAeBe stars and PSF stars into multiple subsets of equal integration time. This offers the advantage of excluding integration time as a factor for wider FWHM in HAeBe stars, while providing information about the seeing conditions during the observation and a good statistical sample to strengthen the results. This technique could only be used to measure diameters at this level, where the surface brightness of the individual data frames was well above the 3σ level of the background.

We considered a source to be extended if the deconvolved diameter minus the error was larger than zero. For all unresolved sources, I calculated limiting sizes at the FWHM brightness contour level by increasing the FWHM of the HAeBe stars until the deconvolved size minus the error was larger than zero.

A last step taken to evaluate extension in the systems was to subtract the PSF from the sources. First, I normalized all images so that the peak fluxes in all HAeBe stars and PSF stars equal 100. This was done by dividing all the HAeBe and PSF star images by the peak fluxes in their images and multiplying by 100. I then cropped the images so that the peak position for PSF and HAeBe stars were on the same position in the images, and subtracted the PSF image from the HAeBe star image. Residual emission after PSF subtraction is another evidence of extended emission. To measure diameters of this more extended fainter emission, I chose surface brightness contour levels equivalent to 0.5 % and 1 % of the peak emission at 11.7 μm , and 5% and 3 % of the peak emission at 18.5 μm . These specific levels were chosen so that they were more than three times the background noise for all extended sources and their respective PSF stars. Since I used stacked images in this procedure, all observations without stable seeing, as reflected in the FWHM measurements, were discarded from this analysis. In order to assess the validity of the residuals, I directly measured the diameters at the specific brightness levels from the images and used half the spread in sizes observed in the FWHM as an upper limit to the errors.

Properties of the Circumstellar Dust

In this section I explain the different analysis I used to derive properties of the circumstellar dust for all the sources in the survey.

Dust Temperature

The temperature of a dust grain in radiative equilibrium depends on the optical properties of the grain and its distance from the radiating source.

The flux from an isotropic source at a point P at a distance r from a star of radius R and effective temperature T_{eff} is

$$F_\nu = \int B_\nu(T_{eff}) \cos \theta d\Omega \quad (3.4)$$

where $d\Omega = 2\pi \sin \theta d\theta$ is the solid angle of the observations. From geometry, I can then write:

$$F_\nu = B_\nu(T_{eff}) \pi \int \sin 2\theta d\theta = \pi B_\nu(T_{eff}) \left(\frac{R}{r}\right)^2 \quad (3.5)$$

Then the power from the central star absorbed by a uniformly heated dust grain at that location will be

$$F_{\nu(abs)} = \pi a^2 \int Q_\nu \pi B_\nu(T_{eff}) \left(\frac{R}{r}\right)^2 d\nu \quad (3.6)$$

where a is the dust grain radius and Q_ν is the emissivity of the material, which also depends on grain size; grains absorb and emit radiation more efficiently for wavelengths smaller than the grain size.

The power radiated by the grain is then given in terms of the dust grain temperature, T_g , by

$$F_{\nu(rad)} = 4\pi a^2 \int Q_\nu \pi B_\nu(T_g) d\nu \quad (3.7)$$

and, given the condition of radiative equilibrium, I can then write

$$\int \left(\frac{R}{r}\right)^2 B_\nu(T_{eff}) Q_\nu d\nu = 4 \int B_\nu(T_g) Q_\nu d\nu \quad (3.8)$$

with the assumption:

$$Q_\nu \begin{cases} 1 \rightarrow \lambda < \lambda_0 \\ Q_0 \left(\frac{\lambda_0}{\lambda}\right)^n \rightarrow \lambda > \lambda_0 \end{cases} \quad (3.9)$$

where λ_0 is a critical wavelength in the sense that absorption and emission of radiation at wavelengths shorter than λ_0 gives $Q_\nu \sim 1$.

Since the absorbed and the emitted radiation have different wavelengths, I can let $n=p$ for absorbed radiation and $n=q$ for emitted radiation. Then I can use different exponents, p and q , to approximate the behavior of different grain materials. Grains much larger than incoming and emitted radiation can be approximated as blackbody grains with $p=q=0$; grains much larger than the incoming radiation, but smaller than the peak of radiated emission will have $p=0$ and $q=1$ for amorphous materials and $q=2$ for crystalline materials and metals; grains smaller than the incoming and emitted radiation like ISM grains will emit and absorb inefficiently; thus, I can assume that $p=q=1.5$ (Helou 1989, Backman and Paresce 1993).

Therefore, given some assumptions about the composition of the dust grains, I can solve Equation 3.8 analytically to obtain the temperature of the dust grains. Substituting for the Planck function:

$$B_\nu = \frac{2h\nu^3}{c^2 \left[\exp\left(\frac{h\nu}{kT_{eff}}\right) - 1 \right]} \quad (3.10)$$

where c is the speed of light, h is the Planck constant, and k is the Boltzmann's constant into

Equation 3.8 and introducing the Stefan-Boltzman constant, $\sigma = \frac{2\pi k^4}{15h^3 c^2}$, I have:

$$\sigma T_{eff}^4 \left(\frac{R}{r}\right)^2 = 4 \frac{Q_0}{\nu_0^q} 2 \frac{h}{c^2} \int \nu^{q+3} \left[\exp\left(\frac{h\nu}{kT_g}\right) - 1 \right]^{-1} d\nu \quad (3.11)$$

By letting $x = \frac{h\nu}{kT_g}$ we can solve the integral analytically and obtain:

$$\sigma T_{eff}^4 \left(\frac{R}{r}\right)^2 = 8 \frac{Q_0}{c^2 \nu_0^q} (kT_g)^{q+4} h^{-(q+3)} \Gamma(q+3) Z(q+4) \quad (3.12)$$

Defining the stellar luminosity by:

$$L_* = 4\pi R^2 \sigma T_{eff}^4 \quad (3.13)$$

we can then solve for the temperature of grains of different materials as a function of distance to the star:

$$T_g^{q+4} = \frac{L_* \nu_0^q c^2 h^{q+3}}{32\pi Q_0 k^{q+4} \Gamma(q+3) Z(q+4) r^2} \quad (3.14)$$

For blackbody grains, where $q=0$, this is the equivalent expression:

$$T_g = 278 L_*^{\frac{1}{4}} r_{AU}^{-\frac{1}{2}} \quad (3.11)$$

For medium size grains with $q=1$ I get:

$$T_g = 468 L_*^{\frac{1}{5}} r_{AU}^{-\frac{2}{5}} \lambda_0^{-\frac{1}{5}} \quad (3.12)$$

and for very small grains, where $q=p=1.5$, a different expression has to be used, which transforms into:

$$T_g = 636 L_*^{\frac{2}{11}} r_{AU}^{-\frac{4}{11}} T_{eff}^{\frac{3}{11}} \quad (3.13)$$

Warm Dust Mass

We also calculated the warm dust masses in these systems. Using the dust temperatures derived from the flux ratios and the dust thermal emission at $18.3 \mu\text{m}$, I can provide a rough estimate of the minimum warm dust mass contributing to the observed emission by using,

$$M_{warm} = \frac{F_\nu D^2}{B_\nu(T_g) \chi_\nu} \quad (3.14)$$

where F_ν is the flux density from dust thermal emission at 18.3 μm , T_g is the derived average dust grain temperatures for the systems, D is the distance to the sources in parsecs as listed in Table 3-1, and χ_ν is dust absorption opacity estimated to be 1000 cm^2/g (Ossenkopf, Hennings & Mathis 1992).

Dust Size Distribution

I used an approach similar to the one explained in the Dust Temperature section to derived typical dust grain sizes. Instead of plotting the temperature of the grains as a function of radius, I plotted the expected flux ratios for particles of different sizes and values of λ_0 as a function of the distance to the star. I then used the flux ratio from the observations and assigned this value to the mid-point of the resolved extended emission region or the mid-point of the limiting size in the case of unresolved sources. Just by inspection, I can find which modeled flux ratio better represents the observed flux value (large blackbody grains, very small grains, or mid-size grains of some specific λ_0). In the case of mid-size grains, the value of λ_0 can be used to estimate grain sizes: $a \sim \lambda_0$ for moderately absorbing dielectrics and $a \sim \lambda_0/2\pi$ for strongly absorbing materials (Greenberg 1978).

State of Evolution of Dust Grains

Studying the effects of the ratio of the radiative to gravitational forces, β , on the maximum sizes derived above, I can assess the evolution of the dust in these systems.

$$\beta = \frac{3L_*}{16\pi cGM_*a\rho} \quad (3.15)$$

where c is the speed of light, G is the gravitational constant, L_* is the stellar luminosity from Table 3-1, M_* is the stellar mass also from Table 3-1, a is the size of dust grains derived above, and ρ is the dust density. For $\beta > 1$, the radiative force will predominate. Studies of the solar

system zodiacal cloud have shown that for realistic grain materials, particles are in bound orbits for $\beta < 0.5$. All particle sizes in a system giving $\beta > 0.5$ will be in unbound orbits and expelled from the system in a timescale comparable to the orbital period.

Opacity

Stellar optical radiation penetrates the CS dust to a radius corresponding roughly to an optical depth $\tau_v = 1$. If I assume a flat disk, with inner radius, R_{in} , equal to the dust sublimation radius, outer radius, R_{out} , equal to the larger disk size known for a system, thickness ΔS , a cold dust mass, M_{mm} , from sub-mm and mm studies when available, and uniform volume dust ρ_o density given by the relationship:

$$\rho_o = \frac{M_{mm}}{\pi(R_{out}^2 - R_{in}^2)\Delta S} \quad (3.16)$$

we can calculate the optical depth along the plane of the disk by using:

$$\tau_\lambda = \kappa_\lambda \int_{R_{in}}^R \rho_o dr \quad (3.17)$$

with the absorption coefficient of the form

$$\kappa_\lambda = \kappa_{\lambda 0} \left(\frac{0.25mm}{\lambda} \right) \quad (3.18)$$

where $\kappa_{\lambda 0} = 0.1 \text{ cm}^2 \text{ g}^{-1}$ (Hildebrand 1983). From these calculations I can estimate the radius of the disk for which $\tau_v = 1$, where the disk becomes optically thick. This value is an upper limit in the sense that the inner regions of a flaring disk are likely to be thinner than 10 AU, and any other axisymmetric dust density distribution will place more dust mass closer to the star making the disk opacity higher at small radii. Knowing where $\tau_v = 1$ for a system tells us how far stellar radiation penetrates into the plane of the disk. Dust located at larger radii should be cold and;

therefore, undetected at mid-infrared wavelengths. If I detect warm dust beyond this radius in a system, it implies that the dust must be heated by direct radiation from the star and consequently should be located above or below the disk mid-plane in an optically thin region either a halo or the surface layer of a flaring disk.

To further constrain the location of the mid-infrared emitting dust in the system, I considered the vertical (i.e. perpendicular to the plane of the disk) optical depth in a system. Given the low optical extinction toward the central star, I believe most of these systems to be close to face-on; therefore, an estimate of the vertical optical depth of the disk at mid-infrared wavelengths should indicate if I are only detecting emission from the dust located above the disk (if the disk is optically thick to mid-infrared radiation) or from both sides of the disk (if the disk is optically thin to mid-infrared radiation). The disk in the mid-plane evidently would be too cool for us to detect even if it were optically thin to mid-infrared radiation since optical radiation cannot penetrate there.

For a disk surface density with the radial distribution

$$\Sigma = \Sigma_0 \left(\frac{1AU}{r} \right)^2 \quad (3.19)$$

where Σ_0 is the disk surface density in g cm^{-2} and

$$\tau_\lambda = \kappa_\lambda \Sigma \quad (3.20)$$

we can calculate how far from the central star the disk becomes vertically thin to mid-infrared radiation.

Passive Flared Disk Model

The Chiang and Goldreich model is based on the idea that the surface of a CS disk is irradiated by the central star under a shallow angle. Previously in this chapter, I derived the

energy balance equations for an optically thin disk. A grain of dust in a thin disk sees radiation from all the stellar surface facing it. This is not the case for very massive, optically thick disks. The previously derived equations have to be modified then to include the angle α of incidence of stellar radiation upon the disk, (grazing angle). The irradiated flux can then be written by

$$F_{\nu} = \alpha \frac{L_{*}}{4\pi r^2} \quad (3.21)$$

and the emitted flux disk temperature takes the form

$$T \approx \left(\frac{\alpha}{2}\right)^{1/4} \left(\frac{R}{r}\right)^{1/2} T_{eff} \quad (3.22)$$

For a flat disk, the scale height, H , is independent of radius, and the grazing angle, α , and can be approximated by $\alpha \cong \frac{0.4R}{r}$ for $r \gg R$ (Ruden and Pollack 1991). Chiang and Goldreich (1997) presented a more general form of this equation accounting for the height H of the disk surface above the mid-plane:

$$\alpha \cong \frac{0.4R}{r} + r \frac{d}{dr} \left(\frac{H}{r}\right) \approx \xi \frac{H}{r} \quad (3.23)$$

The irradiated dust at the surface of the disk absorbs stellar flux and re-radiates in the infrared part of the spectrum. About half of the infrared flux is radiated away from the disk plane and escapes the system; the other half is sent downwards and heats the dust grains in the disk's mid-plane. The higher densities expected in these more massive optically thick disks translate into thermal coupling of the dust and gas in the disk (the gas and dust in the disk have equal temperatures). The heating of the mid-plane by the re-radiated infrared emission from the optically thin outer layer heats the dust and gas in the mid-plane, resulting in higher gas temperatures and increasing the gas pressure. The increase in gas pressure counteracts the effect

of the gravitational forces pulling disk matter towards the mid-plane and affects the vertical scale height, H , of the disk and, consequently, changes the geometry of the disk.

The Chiang and Goldreich model assumes thermal and hydrostatic equilibrium, thermal coupling of the dust and gas, a gas to dust ratio of 100 and a form for the opacity of dust grains and surface density distribution. Given those assumptions and the luminosity of star, the model calculates the expected surface temperature of the disk. Using the previous equations and writing the effective temperature in terms of the stellar luminosity, the surface temperature is given by

$$T^4 = \xi \frac{HL_*}{4\pi\sigma r^3} \quad (3.24)$$

From the surface temperature, the model derives the flux irradiated inward towards the disk mid-plane and calculates the temperature and pressure of the gas in the disk's mid-plane. Using the balance between gravity and gas pressure, the model is solved for hydrostatic equilibrium by iterating from a flat disk geometry and adjusting the scale height of the disk until balance is reached.

The surface scale height H can be written in terms of the pressure scale height, $H = \chi h$, where χ equals a constant and the pressure scale height is defined by

$$h = \sqrt{\frac{kTr^3}{\mu_g GM_*}} \quad (3.25)$$

where μ_g is the mean molecular weight of the gas.

From Equation 3.24 I can write

$$h^7 = \left(\frac{k}{\mu_g GM_*} \right)^4 r^9 \frac{\xi}{\sigma} \frac{\chi L_*}{4\pi} \quad (3.26)$$

and obtain the relation between pressure scale height and radius, $h \propto r^{9/7}$. The resulting geometry is a scale height that increases with radius, a flaring geometry, Figure 3-6.

The modified Chiang and Goldreich model (Natta et al. 2001, Dullemond, Dominik and Natta 2001) starts by clearing the dust inside the dust sublimation radius. Dust can still be present within this region; however, because I am assuming a passive disk, this region is optically thin to stellar radiation. The result of truncating the disk is that dust located at this radius receives stellar radiation head-on, at an angle of 90 degrees, and heats up more than in the Chiang and Goldreich model with a low grazing angle. Because of hydrostatic equilibrium in this region, the vertical scale height of the disk at this inner radius becomes large and creates a wall. The larger vertical scale height implies larger emission surface, which explains the excess near-infrared bump at $3 \mu\text{m}$ in the spectral energy distribution of HAeBe stars. The scale height of the inner rim is computed as the surface scale height of the flaring disk, but using a grazing angle of 90 degrees.

The puffed-up inner rim affects the geometry of the rest of the disk. It intercepts more stellar radiation and the disk region directly behind the rim lies in its shadow and remains cold. This shadowed region is heated only by the fraction of stellar light scattered towards the disk by the edge of the rim and by thermal diffusion from the inner rim, resulting in a very cold region with little contribution to the total emitted radiation from the disk. The geometry in the outer regions of the disk can take two solutions. If the disk opacity is high, the surfaces of the outer parts are still irradiated as in the Chiang and Goldreich model. Re-emitted stellar flux from the inner rim and surface layer towards the disk's mid-plane maintains the temperature; therefore, the pressure of the gas is high enough to increase the scale height of the disk, resulting in a flaring region. In the second solution, the geometry of the system in the outer regions remains at low

scale height. This is the result of low dust opacities; the absorbed flux is not sufficient to push the surface layer up and the disk stays in the shadow of the inner rim. Figure 3-7 shows a schematic picture of these two geometries and the expected SED for each case.

Table 3-1. Physical properties of program stars.

HD #	Sp. Type	d [pc]	Log Teff [K]	log L [Lsun]	Mass [Msun]	age [Myr]
31293	A0V	144	3.98	1.71	2.57	3.81
34282	A0Ve	400	3.94	1.38	2.19	6.08
36112	A3-5IV/V	204	3.91	1.47	2.00	5.67
36917	A0V	460	3.93	2.20	3.72	1.22
37806	B9-A2V	470	3.95	2.13	3.36	1.69
38087	B5V	470	4.20	2.56	4.98	2.03
41511	A2esh	328	3.97	3.10	7.00	3.94
50138	B5-B9Ve	290	4.19	2.85	5.02	0.79
58647	B9IV	280	4.03	2.48	4.06	0.80
97048	B9-A0V	180	4.00	1.61	2.53	4.96
100453	A9V	112	3.87	1.09	1.84	14.69
135344	A0-F4V	140	3.82	1.01	1.74	9.70
139614	A7Ve	140	3.89	1.03	1.85	10.45
144668	A5-7III/IV	210	3.90	1.98	3.26	1.65
150193	A1-2IV/V	150	3.95	1.38	2.18	7.08
158643	B9-A0V	131	4.00	2.39	3.88	1.22
163296	A0-A3IV/V	122	3.94	1.52	2.30	4.56
169142	B9-A5V	145	3.91	1.13	1.94	10.59
179218	B9Ve	240	4.00	2.50	4.33	0.73
244604	A0-A3V	336	3.95	1.35	2.18	7.53

Note: columns (2-5) Acke et al 2005, van den Ancker 1998, van Boekel 2004, Pietu et al. 2003, Jura et al. 2001, Hamaguchi et al. 2005, Moth et al. 1997. Columns (6, 7) calculated from stellar PMS tracks (Seiss et al. 2000)

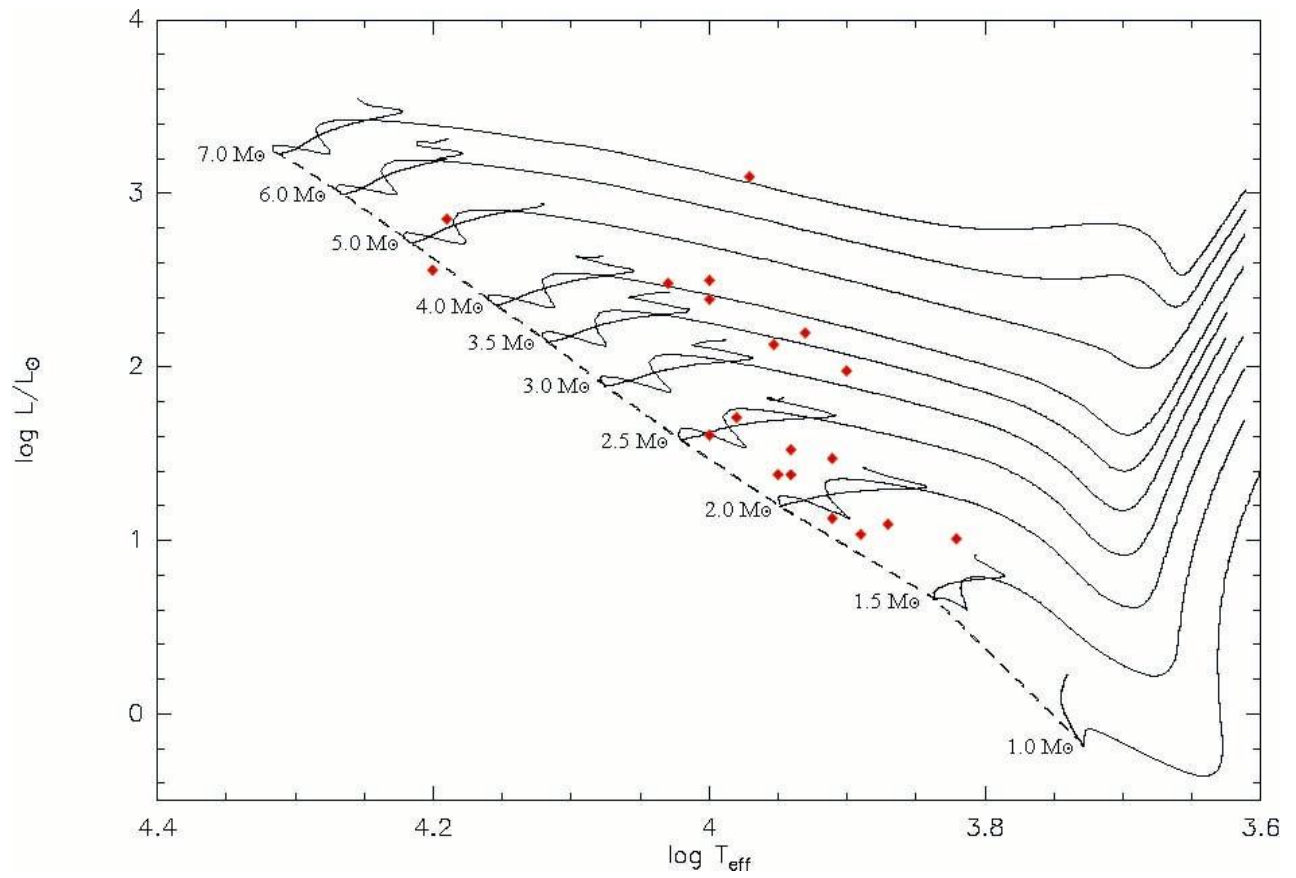


Figure 3-1. H-R diagram for all the sources included in this survey. PMS evolutionary tracks are from Seiss et al. (2000)

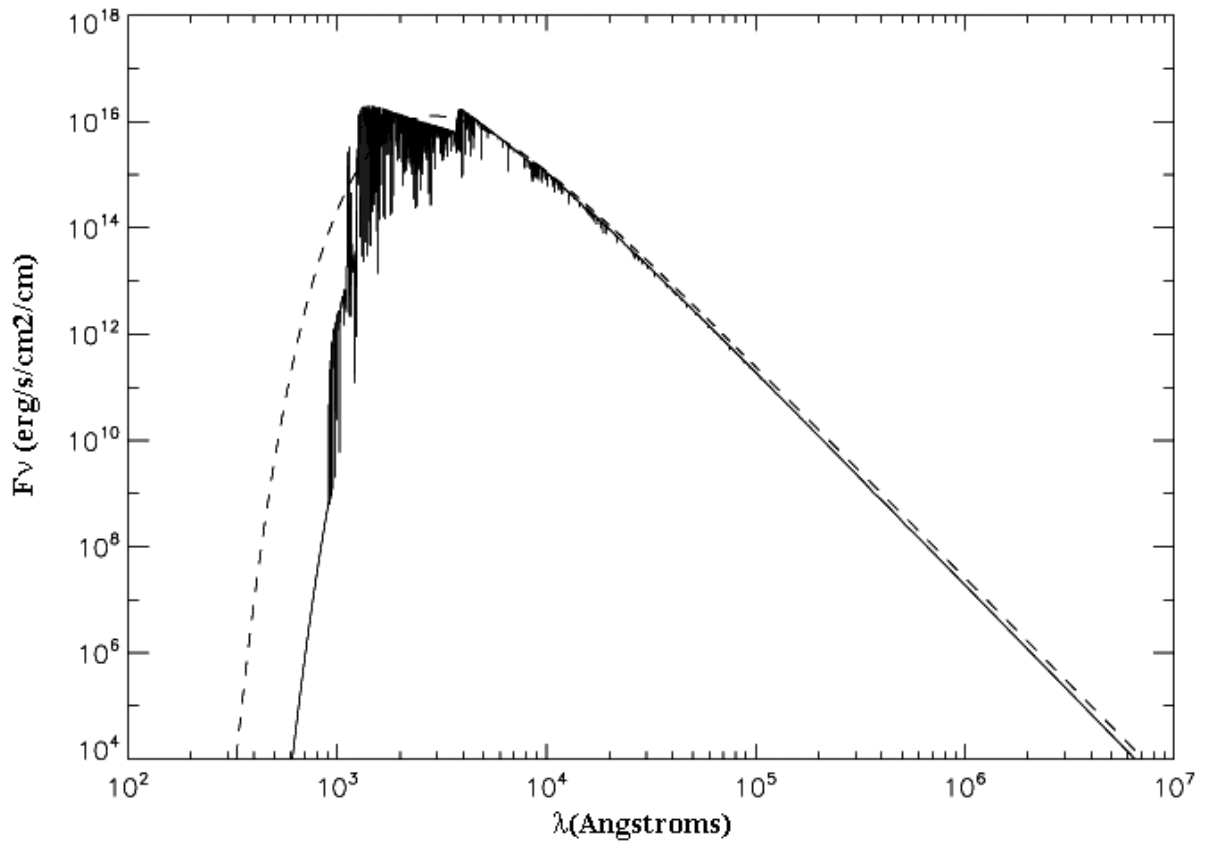
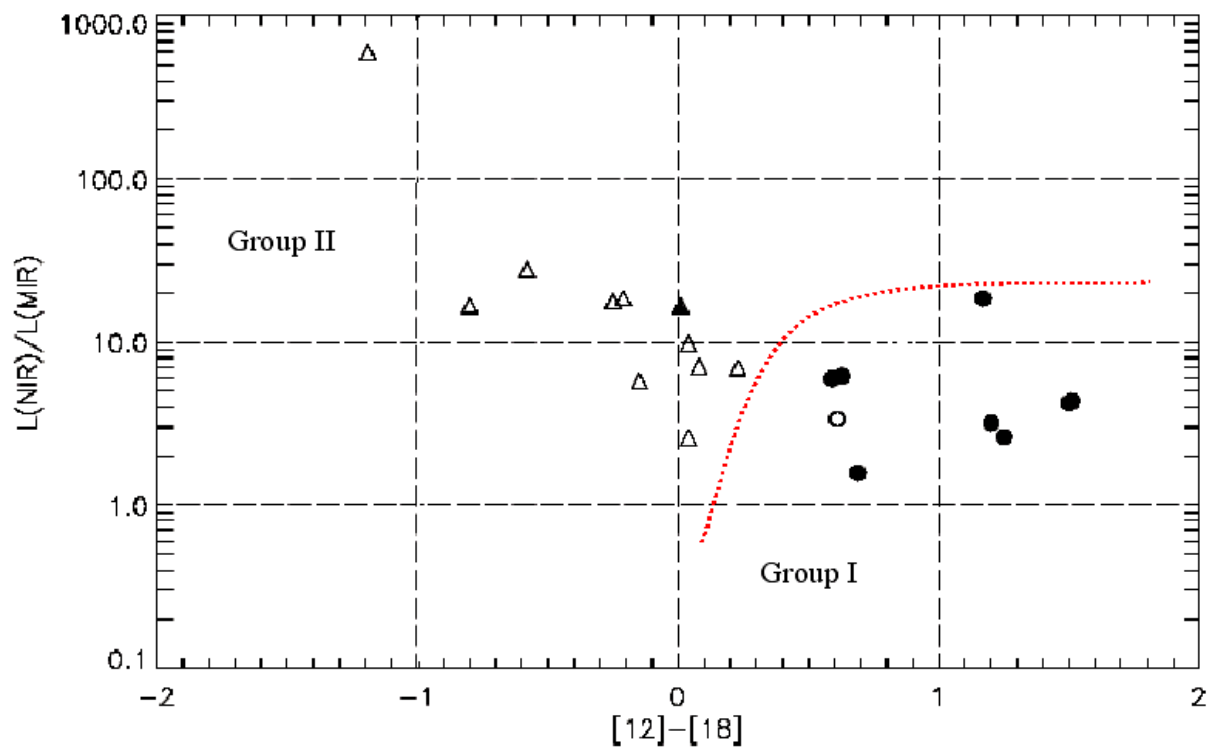


Figure 3-2. Spectrum from stellar photosphere using the NextGen model is shown with the solid line. The dashed line shows the blackbody approximation for a stellar source with the same temperature. The two curves are very similar in the infrared regime of the spectrum.



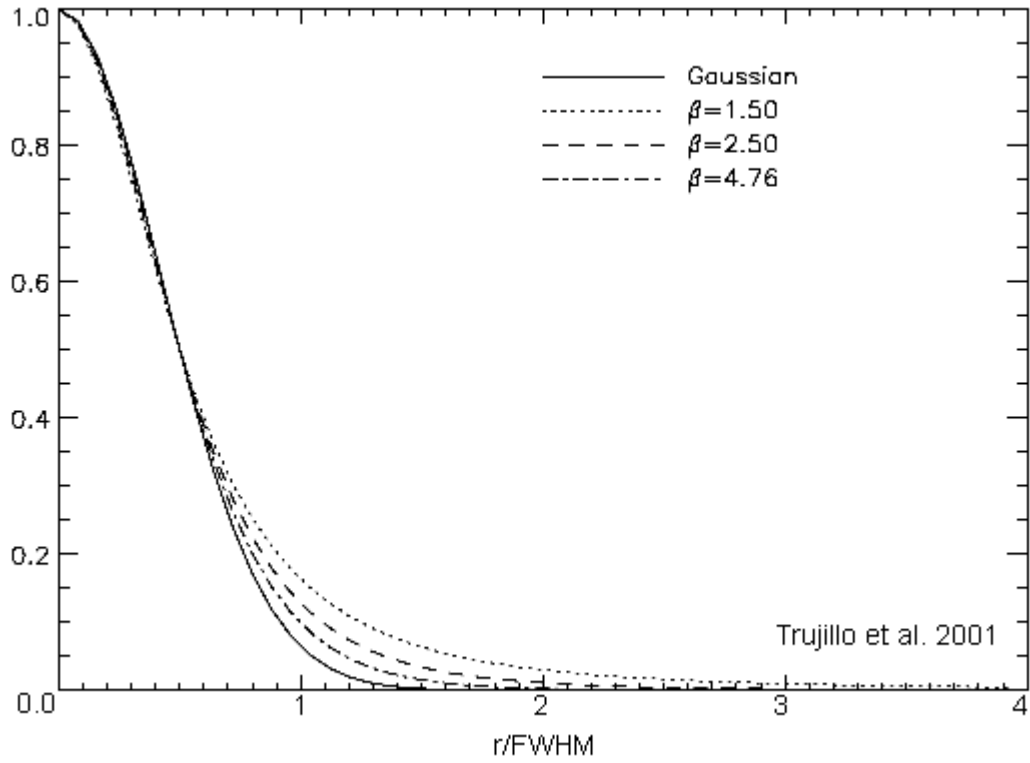


Figure 3-4. Normalized intensity profile of a Gaussian function and Moffat functions with different parameters β . The difference in the profiles is in the wings. The lower the β value, the larger are the wings of the profile.

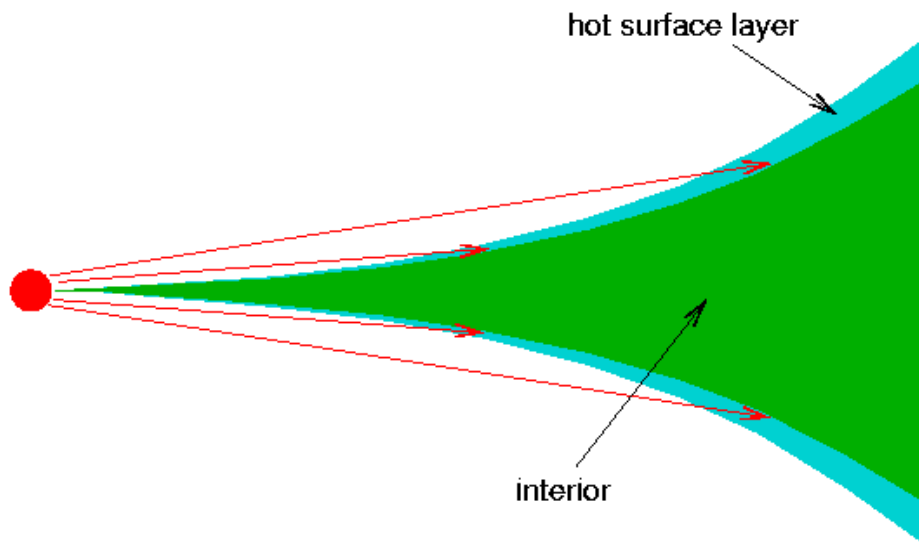


Figure 3-5. Representation of the Chiang and Goldreich flaring disk. The dust disk extends all the way to the central star. The optically thin surface layer of the disk receives stellar radiation at a low grazing angle, while the mid-plane remains colder.

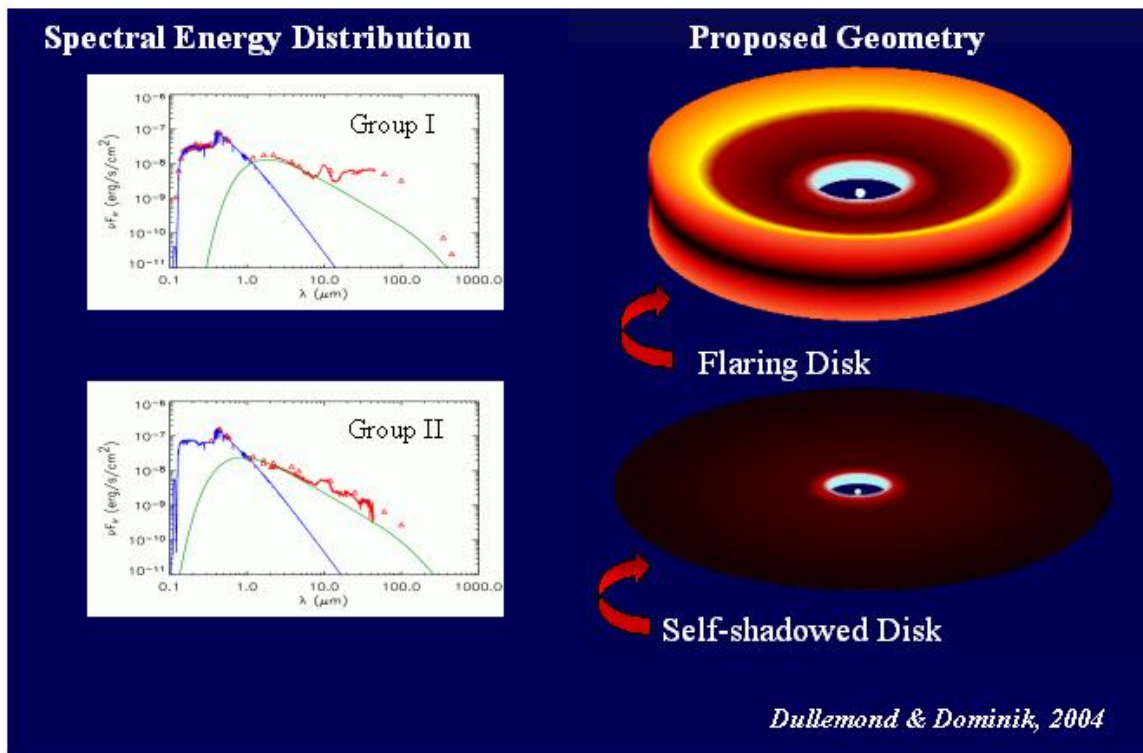


Figure 3-6. The two solutions for the modified Chiang and Goldreich disk model. The inner region of the disk is cleared because the dust is destroyed at temperatures above 1500 K. The dust at the edge of the disk is then heated directly by stellar radiation and its scale height increases because of gas pressure. The area directly behind the puffed-up inner rim stays in the shadow of the rim and is very cold. At larger radii, if the optical depth of the disk is high, the disk will assume the flaring disk geometry of the Chiang and Goldreich model; however, if the optical depth of the disk is low, the disk will remain flatter and in the shadow of the inner rim. These two geometries have been associated with the Meeus et al. (2001) classification of Herbig Ae/Be stars in Group I (flaring disks) and Group II (self-shadowed disks).

CHAPTER 4 AB AURIGAE

Located only 144 pc away (van den Ancker et al. 1998), the 2 Myr old A0 star AB Aurigae is the brightest ($V = 7.06$) of the original sample of Herbig stars (Herbig 1960), which are intermediate mass (2 to 8 M_{\odot}) pre-main sequence stars. Consequently, it is not only the best-studied Herbig object, but an important touchstone for the understanding of the class. The spectral energy distribution (SED) of this source shows emission in excess of the photosphere throughout the infrared region indicative of circumstellar (CS) dust. Different models, among which are a highly inclined passive flared disk with an inner rim (Dullemond et al. 2001); a flat thick disk surrounded by a halo (Vinković et al. 2003); and a halo alone (Elia et al. 2004) have been used to explain the spatial distribution of this dust. Notwithstanding their differences, all of these models reproduced the observed SED reasonably well, which indicates the need for high-resolution imaging to provide additional critical constraints.

Spatial observations at various wavelengths imply that the CS dust in the AB Aur system lies in a disk and some type of more extended structure, Figure 4-1. An inhomogeneous envelope extending to 1300 AU is apparent in optical scattered light (Grady et al. 1999), while closer to the star, in optical and near-IR scattered light, one sees what appears to be a disk with quasi-spiral structure, a radius of 580 AU, and an inclination of 30° (face-on = 0°), assuming flat geometry (Grady et al. 2001, Fukagawa et al. 2004), Figure 4-2. CO observations reveal a complex disk with an inner hole of about 70 AU extending out to 1000 AU and possibly having non-keplerian motions, while 1.4 mm continuum observations indicate a disk with an inner radius of 110 AU and an outer radius of 350 AU (Pietu et al. 2005; see also Mannings and Sargent 1997; Corder et al. 2005). Near-IR interferometric studies resolve the inner 0.7 AU region of the disk (Millan-Gabet et al. 2001). However, previous mid-infrared studies present

somewhat contradictory results. Marsh et al. (1995) report an extended structure at $17.9 \mu\text{m}$ with a semi-major axis of 80 ± 20 AU and an inclination of 75° . Chen and Jura (2003), using the 10 meter Keck telescope, do not confirm that detection of extended structure, and at $20.5 \mu\text{m}$ using deconvolved images with a resolution of $0''.6$, Pantin et al. (2005) report an elliptical ring-like structure at an average distance of 280 AU from the star. In addition, Liu et al. (2005) resolve the inner disk interferometrically at $10.3 \mu\text{m}$, determining a size of 27 ± 3 AU and an inclination of 45° . There is also recent evidence that AB Aur could be the brighter component of a binary system, with a companion separation most likely between 1 and 3 arcseconds (Baines et al. 2006).

In this Chapter I present deep mid-infrared images of AB Aur obtained at Gemini North. I have resolved the emission close to the star at 11.7 and $18.1 \mu\text{m}$, and found an additional extended component that appears to be roughly circularly symmetric. I show how these observations of the thermal emission from dust in the AB Aur system help establish a more coherent picture of the dust geometry consistent with most observations at other wavelengths.

Observations and Data Reduction

Observations of AB Aur were obtained on 2003 November 7 using Michelle (Roche 2004) at Gemini North as part of the imaging survey of Herbig Ae/Be stars. Images, Figure 4-3, were taken using the Si-5 filter ($11.7 \mu\text{m}$, $\Delta\lambda = 1.1 \mu\text{m}$) and Qa filter ($18.1 \mu\text{m}$, $\Delta\lambda = 1.6 \mu\text{m}$). The standard chop-and-nod technique was used to remove thermal background from the sky and telescope. The total on-source time was 645 seconds for each filter. The nearby point-spread-function (PSF) star PPM 94262 was observed before and after each observation of AB Aur. The average values of the full-width at half-maximum (FWHM) intensity of the PSF star were $0''.28$ at $11.7 \mu\text{m}$ and $0''.44$ at $18.1 \mu\text{m}$, comparable to the diffraction limits (λ/D) of the telescope at

these wavelengths. A Moffat function was fitted to the radial profile of each source to derive the value of the FWHM. All observations were made at air masses less than 1.2.

Using the standard stars Sirius and Vega for flux calibration and air mass correction, I derive flux densities for AB Aur of 21 ± 2 Jy at $11.7 \mu\text{m}$ and 36 ± 4 Jy at $18.1 \mu\text{m}$. These values fall within the spread of previous measurements for AB Aur, Table 4.1, which is thought to be variable in the mid-infrared, and the reported error bars are typical for mid-infrared photometry. In addition to the emission from dust, the measured fluxes contain mid-infrared radiation from the stellar photosphere. I estimated the contribution from the photosphere by using the NextGen models developed by Hauschildt et al.(1999), assuming a stellar effective temperature of 9500 K (van der Ancker et al. 1998), $\log g = 4.0$, and solar metallicity. I scaled the model using UVB fluxes for AB Aur (Malfait et al. 1998). From this procedure, I estimate the photospheric flux densities to be 0.054 Jy at $11.7 \mu\text{m}$ and 0.021 Jy at $18.1 \mu\text{m}$, which are negligible compared to the emission from dust.

Source Size

We show in Figure 4-4 the contour levels for AB Aur and the PSF star, scaled so that peak fluxes and the lowest contours are at the same flux level for both images. The lowest contour represents the 3σ flux level (three times the background noise) for the AB Aur images. The far right panels in the figure show the residuals after subtraction of the normalized PSF from AB Aur. This residual corresponds to fainter emission extending out to 2 arcsec (280 AU) from the star at $11.7 \mu\text{m}$ and to 2.5 arcsec (350 AU) at $18.1 \mu\text{m}$. This later value equals the outer boundary of the dust emission seen in the millimeter continuum by Pietu et al. (2005). I do not see evidence in the images of a ring-like structure as proposed by Pantin et al. (2005).

At these wavelengths a fit to the contour levels of AB Aur between $0''.2$ and $2''.0$ in radius indicates an approximately constant position angle of $80^\circ \pm 11^\circ$, with an inclination (under the assumption of flat disk geometry), $i = \cos^{-1}(\Delta y / \Delta x)$, of $29^\circ \pm 11^\circ$ at $11.7 \mu\text{m}$ and $12^\circ \pm 12^\circ$ at $18.1 \mu\text{m}$, where Δy and Δx are the semi-major and semi-minor axis of the fitted ellipse. The uncertainties in the measurements arise from multiple fittings as I vary the radii of the ellipse. This low, nearly face-on, inclination is consistent with recent optical and near-IR results (Grady et al. 01, Fukagawa et al. 04).

We also clearly resolve a bright, compact inner emission region near AB Aur. Figure 4-5 shows the values of the FWHM for AB Aur and the PSF star. I clearly resolve a bright, compact inner emission region near AB Aur. Since integration time can influence the FWHM of the image due to effects such as guiding error, rotation of the pupil and seeing, I divided the data into subsets (equal to the nod dwell time) of equal integration time for AB Aur and PSF star. By comparing these subsets, I conclude that the difference of the FWHM for AB Aur and the PSF star is evident and not an artifact of integration time. Quadratic subtraction of the average FWHM values of the source and the PSF star gives source sizes for the strong compact emission of $17 \pm 4 \text{ AU}$ at $11.7 \mu\text{m}$ and $22 \pm 5 \text{ AU}$ at $18.1 \mu\text{m}$. Error bars in these measurements were calculated using error propagation of the standard deviation of the average FWHM values for AB Aur and PSF star as seen in Fig. 4-5. The size of the compact emission is consistent with that determined by Liu et al. (2005) at $10 \mu\text{m}$.

Dust Properties

Even elementary considerations imply that the AB Aur disk is structurally complex. In this section I show that radial variations probably exist in the grain size and/or composition, and

that the extended mid-IR originates in an optically thin region bounding an optically thick layer near the disk mid-plane.

Particle Temperature and Sizes

Because the most extended mid-IR emission is faint, I divide the images into three annuli centered on the star, each with a width $\Delta r = 100$ AU. This is equivalent to 2.3 and 1.6 of the resolution elements at 11.7 and 18.1 μm , respectively. By assuming that the mid-IR emission is optically thin and that the measured fluxes at both wavelengths originate within the same region, I then calculate average color temperatures of 215 ± 3 K, 189 ± 6 K, and 184 ± 10 K for the circumstellar dust within each of the three regions, with the highest temperature corresponding to the region nearest the star. The quoted uncertainties in these temperatures are due only to measurement errors in the flux densities, which are the relevant uncertainties when examining the radial trends in temperature and corresponding dust properties. The expected blackbody temperatures at these distances are 103 K at 50 AU, 59 K at 150 AU, and 46 K at 250 AU, which are much lower than the derived color temperatures, indicating the presence of smaller, less efficiently emitting grains.

The temperature of a dust grain in thermal equilibrium with stellar radiation depends on the distance to the heating source and on the radiative efficiency of the dust particle. The value of the efficiency depends on the properties of the material and the size of the grain and can be considered equal to unity for radiation shorter than a critical wavelength λ_o . Given some assumptions about the material, the value of λ_o can be used to estimate a characteristic grain radius a as explained in detail in Chapter 3. One finds that $\lambda_o \approx a$ in the case of moderately absorbing dielectrics such as graphite and amorphous silicate, while $\lambda_o/2\pi \approx a$ for strongly absorbing dielectrics like polycyclic aromatic hydrocarbons (PAHs) (Backman and Paresce

1993). I used the energy balance equations as presented in Chapter 3 to calculate the expected flux ratio (11.7/18.1) for different values of λ_o as a function of distance to the star and constrain the sizes of the mid-IR emitting particles throughout the disk. From the observations, the observed flux ratios for the three regions are 0.63-0.68, 0.46-0.53, and 0.44-0.51, with the values decreasing as I move further from the star. Assigning these average flux ratio values to the midpoint of each region and assuming moderately absorbing materials, I see that the emission in these regions can be well constrained to come from particles of sizes 1.1-1.3 μm in the central 100 AU, 0.2-0.3 μm for the dust between 100 and 200 AU, and 0.08-0.12 μm for the dust between 200 and 300 AU. For strongly absorbing material, the corresponding values are 0.2-0.8 μm , 0.02-0.05 μm , and 0.008-0.02 μm for the three regions respectively, Figure 4-6. For strongly absorbing materials, the corresponding average values are 0.2 μm for the compact emission, and 0.04 and 0.01 μm for the other two regions.

These considerations suggest that I need different dust populations to fit the color temperatures at different distances from the star. The circumstellar dust in AB Aur is probably a combination of different materials, since PAH emission bands at 3.4, 6.2, 7.7, 8.6, and 11.3 μm and the amorphous silicate emission feature at 9.7 μm have been detected (Cohen 1980, van den Ancker et al. 2000). Thus, the deduced radial variation in particle size may result partly or entirely from a radial variation in dust composition. Pietu et al. (2005) find that the CO emission in AB Aur extends out to 1000 AU, whereas the millimeter dust continuum, such as the 18.1 mm emission, extends only to 350 AU. They propose that this marked difference in the CO and dust continuum radial distributions may be due to a fairly abrupt change in the radial variation in the dust opacity, perhaps associated with less-processed dust at larger radii. Thus, at least qualitatively, both sets of observations support the idea that there are radial variations in the dust

properties in the AB Aur disk. Mid-IR spectroscopy from the Very Large Telescope Interferometer (VLTI) of three other Herbig Ae stars has revealed radial variations of dust composition in those systems, with crystalline silicates dominating the inner 2 AU regions, and a mixture of crystalline and amorphous silicates located in the 2-20 AU regions of the disks (van Boekel et al. 2004). Detailed follow-up mid-infrared spectroscopy with high spatial resolution of the AB Aur system can help resolve this issue.

Dust Optical Depth and Disk Morphology

Stellar optical radiation penetrates the CS dust to a radius corresponding roughly to $\tau_v = 1$. I assume that the disk is flat, with an inner radius $R_{in} = 0.5$ AU, an outer radius $R_{out} = 400$ AU, a thickness $\Delta S = 10$ AU, a dust mass $M_{dmm} = 2 \times 10^{29}$ g (Mannings and Sargent 1997), and a uniform volume dust density given by Equation 3.16.

We estimate from these considerations that $\tau_v = 1$ at $R \cong 2$ AU. The value obtained is an upper limit for several reasons. First, for simplicity I have assumed a uniform volume dust density; however, a radially decreasing density distribution with power-law indices in the range 0.5-2.0 is more consistent with previous models (Beckwith et al. 1990; Mennshchikov and Henning 1997; Dullemond et al. 2001) and will increase the dust density closer to the star. Second, extrapolating values of the visible absorption coefficient from the submillimeter region underestimates the visible extinction along the line of sight to the star, which is five times larger than predicted by this relationship at $0.55 \mu\text{m}$ (Mathis 1990); therefore, the value of $\tau_v = 1$ is probably reached at $R < 2$ AU. I conclude that the stellar radiation does not penetrate very far in the plane of the disk, in agreement with the conclusion of Mannings & Sargent (1997). However, for the dust far from the star to reach the temperatures inferred from the observations, it must be heated by direct radiation from the star, which implies heating of the dust above and

below the mid-plane. This dust could reside either in the surface layer of a flaring disk or in an envelope.

To address this issue further, I consider the vertical (i.e. perpendicular to the plane of the disk) optical depth in the system. Since I believe the disk to be almost face-on, an estimate of the vertical optical depth of the disk at mid-infrared wavelengths should indicate whether I am only detecting emission from the dust located above the disk (if the disk is optically thick to mid-infrared radiation) or from both sides of the disk (if the disk is optically thin to mid-infrared radiation). The dust in the mid-plane evidently would be too cool for us to detect, since visual radiation cannot penetrate there. Using the best fit to the AB Aur data for the disk surface density distribution, Equation 3.19, where $\Sigma_0 = 10^4 \text{ g cm}^{-2}$ (Dullemond et al. 2001) and $\tau_\lambda = \kappa_\lambda \Sigma$, I find that the AB Aur disk is optically thick vertically to mid-IR radiation out to a radius of 118 AU. The disk becomes optically thin to mid-IR radiation beyond 118 AU from the star. This result suggests that, except in the outermost disk, I cannot look through the disk at mid-IR wavelengths and are only detecting mid-IR emission from the "surface" layer of the disk facing us. This result has its parallel in the CO observations of AB Aur by Pietu et al. (2005), which show that the optically thick emission lines, arising near the more directly irradiated disk surface, have higher excitation temperatures than the optically thin ones weighted toward material in the disk mid-plane

Models

The passive flared disk model with inner rim developed by Dullemond et al. (2001) returns the detailed geometry of a CS disk for given specific stellar parameters and general disk properties such as dust mass and inner and outer disk radius. I have applied their model code (kindly provided by C. P. Dullemond) to AB Aur to compare the inferred geometry of the disk

model to parameters derived from the observations. In this context, the size of the compact mid-IR emission detected in the images coincides with the emergence at a radius of ~ 10 AU of the disk from the shadow of the inner rim. The model predicts a jump in the surface temperature of the dust at this boundary, which translates into stronger fluxes at mid-IR wavelengths. The dust temperature implied by the images for the compact mid-IR emission is about 100 K lower than the value predicted by the model for the surface layer of the disk at the onset of flaring (see Figure 4-7). This inconsistency results from the fact that I am comparing an average color temperature within the inner 100 AU to the peak temperature from the model within this region. With the exception of the dust at the inner rim, which is heated to dust sublimation temperatures, the model dust temperatures in the inner 10 AU are colder than 200 K because that dust is shadowed from stellar radiation. The dust temperature peaks at a radius of about 10 AU and decreases outwards as r^{-2} . The model indicates that the average temperature of the surface layer in this region is about 200 K, which is consistent with the results in the previous section. In this context, I suggest that the strong compact emission detected in the images is a combination of unresolved emission from the inner rim and emission from the surface layer of the disk at the onset of flaring, which is resolved. Likewise, the size of the more extended component that I detect in the images is as predicted from the model for the outer surface layer of the disk, which becomes too cold at very large radii to be detected in the mid-IR.

The segregation of particle sizes that I derive from the observations can also be explained within the passive flared disk model. Small grains in a region optically thin to stellar radiation, like the surface layer of the disk, experience the effect of radiation pressure. The parameter β is the ratio of the radiative to gravitational forces, which is proportional to the luminosity of the star and inversely proportional to the particle size. For $\beta > 0.5$, particles are on unbound orbits and

will be expelled from the system in timescales comparable to the orbital period of the region where the particles were produced (Backman & Paresce 1993). In the case of AB Aur, these particles will be expelled in timescales of less than 10^3 years for a 500 AU disk in a gas-free environment. I do not consider the presence of molecular CO at radial distances comparable to the mid-infrared emission to be relevant for this result because I believe that the gas and the mid-infrared emitting particles occupy different vertical regions of the disk. When gas molecules collide frequently with dust particles, as is the case when abundant gas and dust coexist, they reach similar temperatures; gas temperatures can drop below dust temperatures as gas is depleted in the system. Pietu et al. (2005) derived temperatures of 70 K for the warm gas near the surface of the disk at a radius of 100 AU and found no evidence for CO depletion. The derived dust temperatures for this radial distance are substantially higher; therefore, it is appropriate to assume that the mid-infrared emitting dust resides in an optically thin layer at the surface of the disk, while the warm gas detected in the system lies at a lower elevation above the midplane. Even if gas and dust coexist, Klar and Lin (2000) showed that hydrodynamic drag forces in a gas-rich environment tend to enhance the effect of radiation pressure, increasing the critical size for particles blown out of the system in a dynamical timescale. The presence of micron-size particles in a system 2-4 million year old implies that there is a replenishing mechanism for these grains, probably collisions of larger particles (Wyatt et al. 1999). Regardless of the formation process involved, if small particles are constantly created, then I should see them at those locations where they are produced or when they are driven outward by radiation pressure from regions closer to the star. They should have lower emission efficiencies, and therefore, elevated temperatures compared to larger dust at the same distance from the star. These smaller, hotter particles would be easier to detect in the mid-infrared farther from the star.

I also considered the implications of the observations if the detected emission originated in a disk and a halo, as proposed by Vinković et al. (2003). The presence of a halo could explain the difference between the derived inclination angles from the study and that of Liu et al. (2005). Given that the images achieved higher sensitivity than those of Liu et al. (2005), I could be seeing more of the tenuous halo or spherical component, which will dilute the asymmetries created by an inclined disk. However, the variation of grain sizes derived from the observations is inconsistent with emission from a halo. In the roughest approximation, if a halo were present I would expect to find a population of larger colder grains concentrated in the disk, and smaller micron and sub-micron size particles residing in the halo. If this were the case, the average grain size in the inner region should be smaller than at larger distances because I would be intercepting more of the halo material in the central region, which is the opposite of the findings.

Conclusions

Our mid-IR images reveal two different emission components in AB Aur. The central stronger emission is resolved, with quadratically deconvolved FWHM sizes of 17 ± 4 AU and 22 ± 5 AU at $11.7 \mu\text{m}$ and $18.1 \mu\text{m}$, respectively. I also detect fainter extended emission out to a radius of 280 AU at $11.7 \mu\text{m}$ and 350 AU at $18.1 \mu\text{m}$. Emission is slightly elongated at $11.7 \mu\text{m}$, indicating a disk inclination angle in the range $29^\circ \pm 11^\circ$ and a PA of $80^\circ \pm 11^\circ$. The morphology at $18.1 \mu\text{m}$ is more circular, corresponding to an inclination angle of $12^\circ \pm 12^\circ$. However, within the uncertainties, inclination angles at 11.7 and $18.1 \mu\text{m}$ are the same. Assuming moderately absorbing material, I derive average radii of the mid-infrared emitting dust in the system and find that larger particles ($a \sim 1 \mu\text{m}$) dominate the mid-infrared emission in the inner (<100 AU) regions of the disk, and smaller particles ($a < 0.3 \mu\text{m}$) dominate in the outer regions of the disk. These results are reasonably well accounted for by a model of a passive flared disk with an inner

rim. The presence of a more spherical component fails to account for the particle size segregation derived from the observations.

Table 4.1. Comparison of flux density measurements for AB Aurigae.

Date Observed	Wavelength [μm]	Flux [Jy]	Reference
Oct. 1993	11.70	20.60	Marsh et al 95
Nov. 1994	11.70	23.00	Marsh et al 95
Feb. 2000	11.70	25.00	Chen & Jura 03
Aug. 2000	11.70	19.00	Chen & Jura 03
Nov. 2003	11.70	19.67	this study
Nov. 1994	17.90	34.70	Marsh et al 95
Feb. 2000	18.70	31.00	Chen & Jura 03
Aug. 2000	18.70	17.00	Chen & Jura 03
Nov. 2003	18.10	35.50	this study

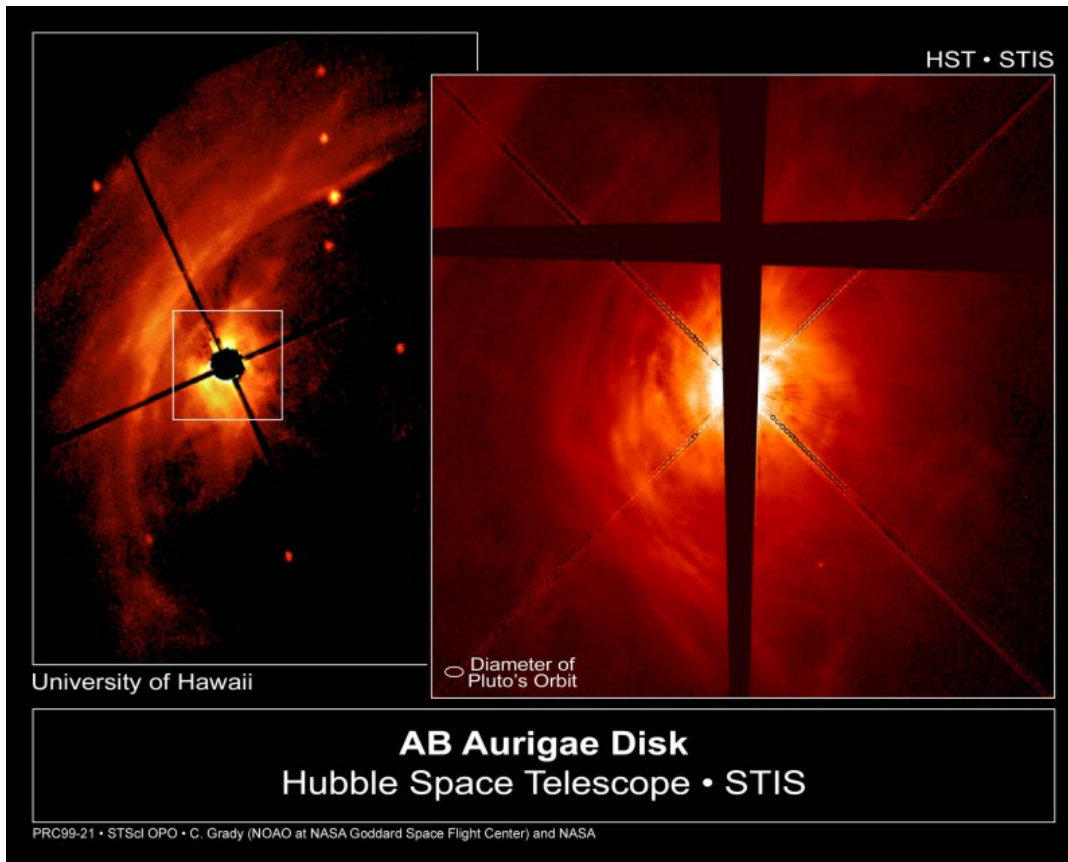


Figure 4-1. Near-infrared scattered light of AB Aurigae taken with STIS at the Hubble Space Telescope (Grady et al. 1999). The image shows the dusty disk closer to the star as well as more extended nebulosity.

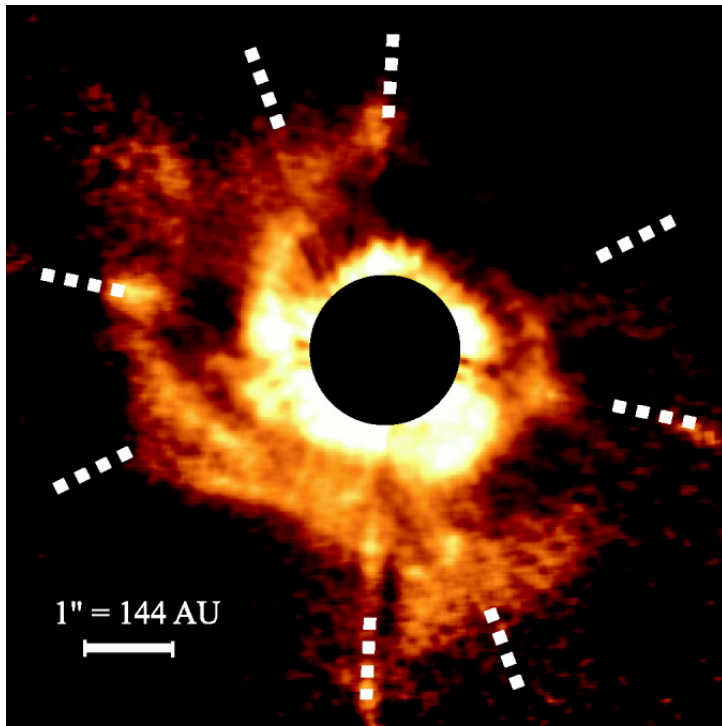


Figure 4-2. Near-infrared scattered light image of AB Aurigae showing spiral structure (Fukagawa et al. 2004)

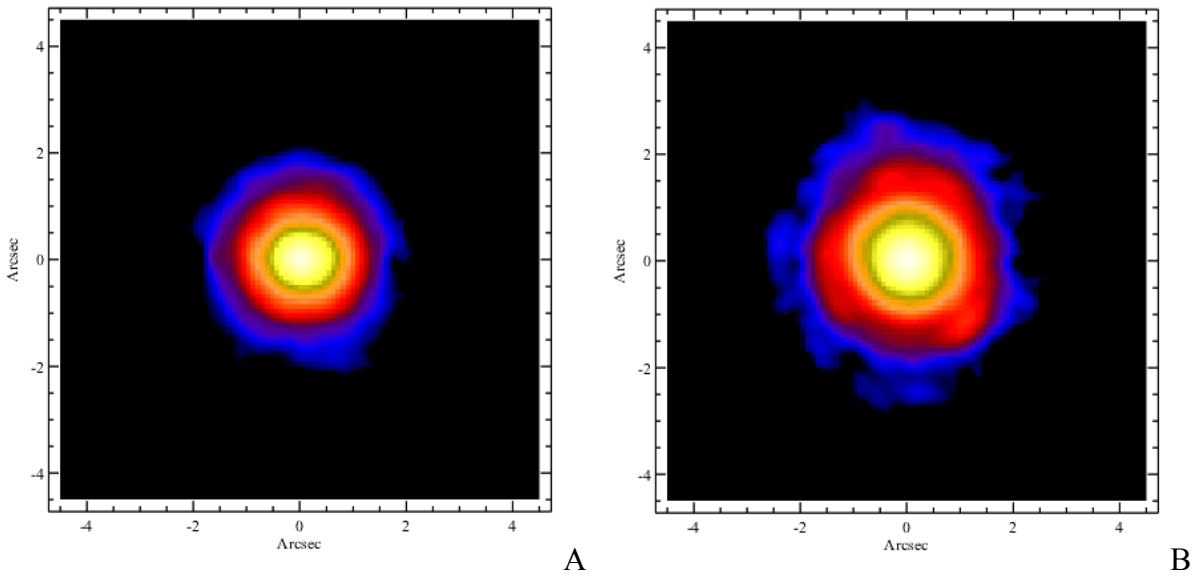


Figure 4-3. AB Auriga false color images at $11.7\ \mu\text{m}$ and $18.1\ \mu\text{m}$ (left and right) taken with Michelle on Gemini North. These maps clearly show the extended mid-IR emission. The lowest color display is at the 3σ level of the background.

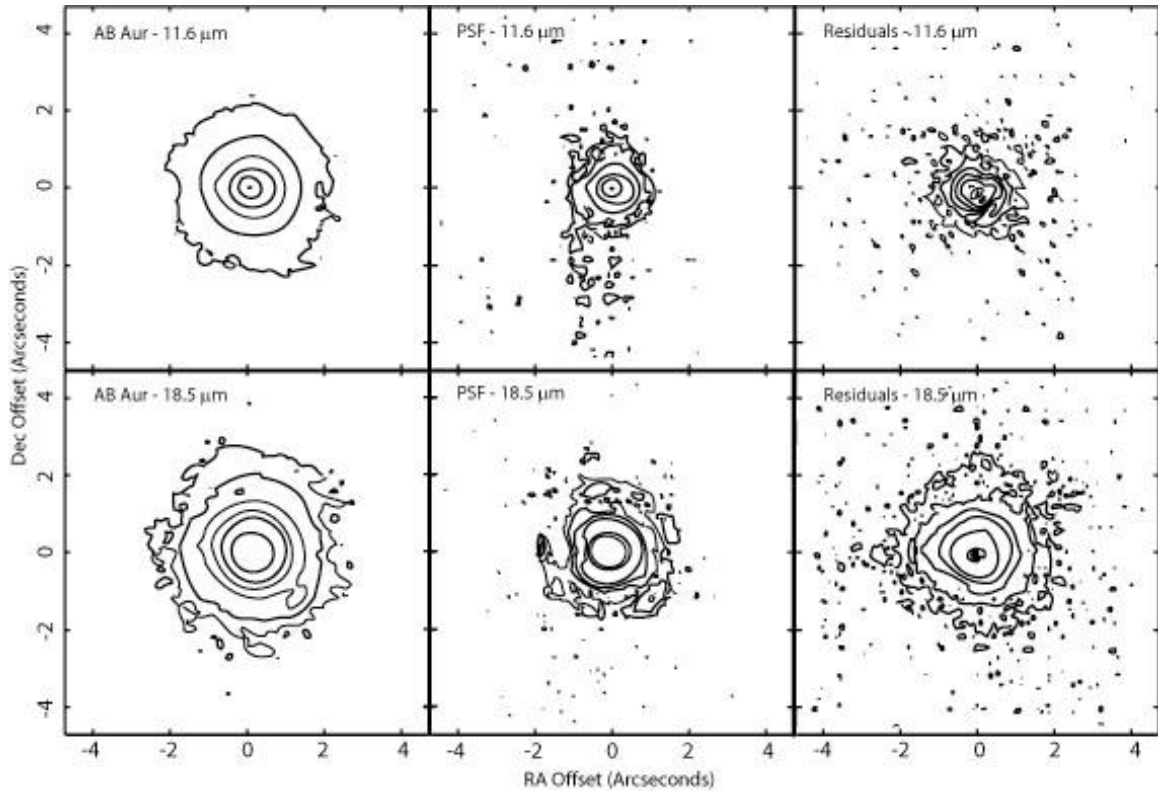


Figure 4-4. Normalized contour level of AB Aur, PSF star and PSF subtracted emission. Upper panels show 11.7 μm data (contour) of AB Aur, PSF star scaled at 100 % of AB Aur peak emission, and PSF subtracted emission. AB Aur and PSF star contour levels are (0.06, 0.25, 1.07, 4.50, 18.86, 79.20) $\text{Jy}/\text{arcsec}^2$, lowest contour is 3σ (60 $\text{mJy}/\text{arcsec}^2$) of the background for AB Aur. Contour levels for the residual emission at 11.7 μm are (0.37, 0.69, 1.31, 2.47, 4.67, 8.83) $\text{Jy}/\text{arcsec}^2$. Lower panels show 18.1 μm data (contour) of AB Aur, PSF star scaled at 100 % of AB Aur peak emission (Sirius was used to obtain better signal to noise ratio at this wavelength), and PSF subtracted emission. Contour levels are (0.15, 0.33, 0.73, 1.61, 3.54, 7.77) $\text{Jy}/\text{arcsec}^2$. Lowest contour is 3σ (150 $\text{mJy}/\text{arcsec}^2$) of the background for AB Aur. Emission from AB Aur can be seen extending to $\sim 2''$ in the 11.7 μm data and to $\sim 2.5''$ in the 18.1 μm data. For cosmetic reasons, a very noisy part of the image at the extreme right of the 11.7 μm PSF image has been removed; that has no effect in the region of the stellar image, per se

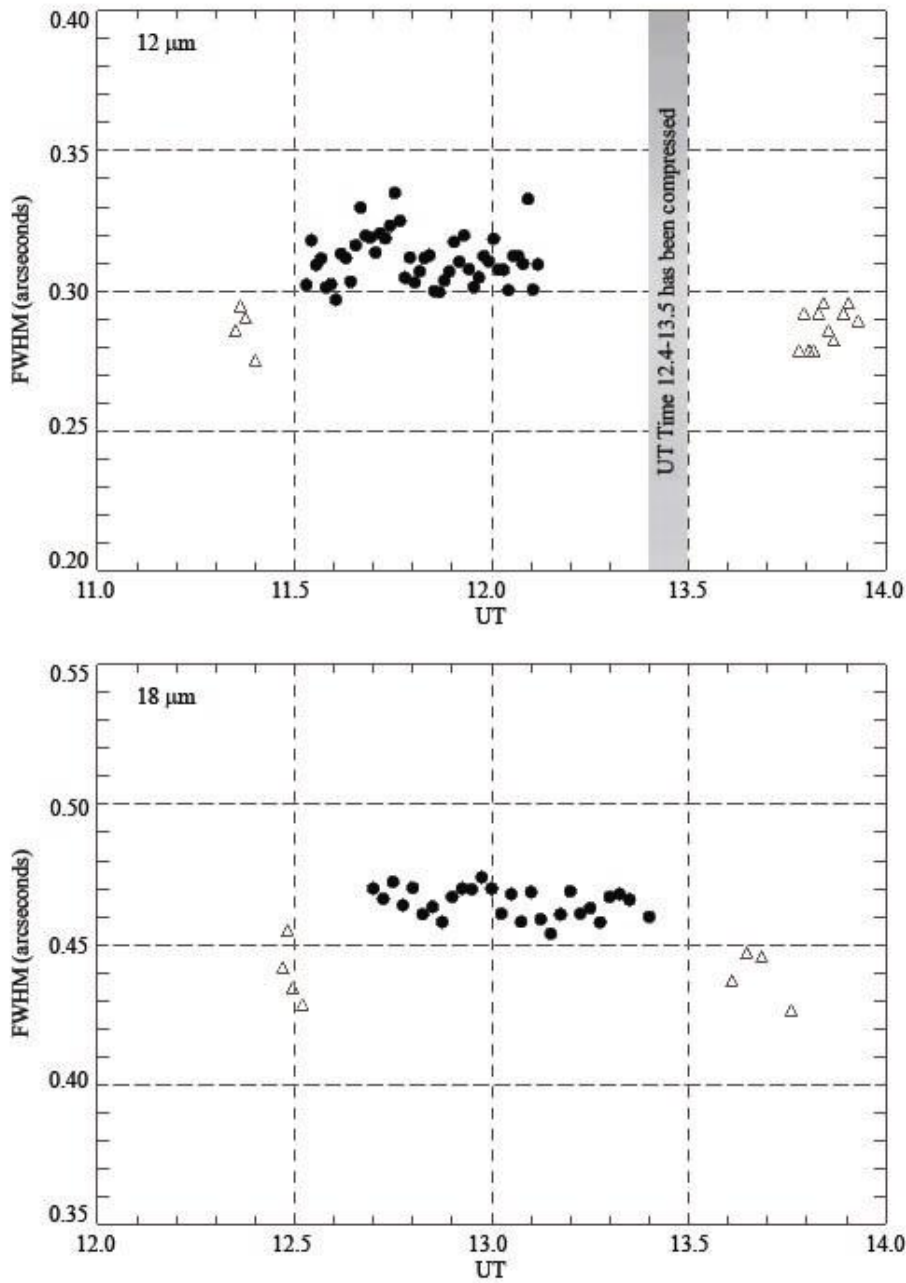


Figure 4-5. 11.7 μm data (top panel) and 18.1 μm (lower panel) FWHM for AB Aur (solid circles) and PSF star (open triangles). Each point of the 11.7 μm data represents 1 nodset for a total on-source time per frame of 0.8 sec. Each point of the 18.1 μm data represents 2 nodsets stacked for a total on-source time per frame of 0.6 sec. After the 11.7 μm observations of AB Aur were taken, the PSF star was going through transit very close to zenith, as a result, there is a large elapse time in the graph between the observations. The second PSF star observation at 11.7 μm was taken at the end of the 18.1 μm observations.

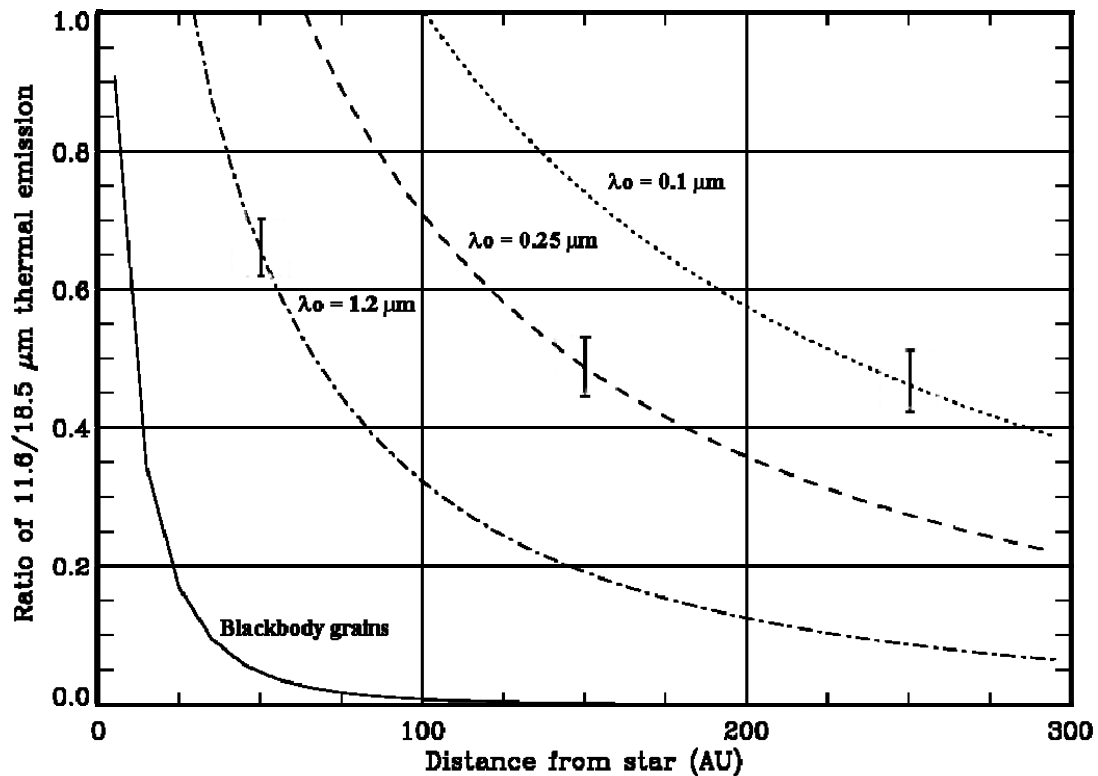


Figure 4-6. Ratio of the thermal emission at 11.7 and 18.1 μm shown for different values of λ_0 . Grain sizes equal λ_0 for moderately absorbing material, or $\lambda_0/2\pi$ for strongly absorbing materials (Backman & Paresce 1993). The observed ratio of flux densities for the regions 0-100, 100-200, and 200 to 300 AU are shown at the mid-point of the three regions at 50, 150, and 250 AU from the star, respectively. The error bars represent the relative uncertainties in the flux measurement ratios.

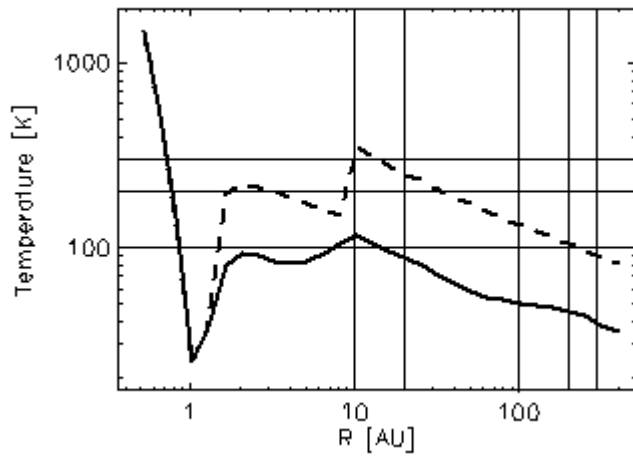


Figure 4-7. Radial distribution of the dust temperature from the flaring disk model of Dullemond et al. (2001). The solid line is the temperature of the disk's mid-plane. The dash line is the temperature of the dust in the surface layer of the disk. In this model the temperature of the flaring layer peaks at 10 AU, comparable to the size I derived from FWHM measurements.

CHAPTER 5
RESOLVING HERBIG AE/BE PROTOPLANETARY DISKS IN THE MID-INFRARED: THE
GROUP I SOURCES

Introduction

The spectral energy distribution (SED) of all HAeBe stars have similar shapes and intensity in the near-infrared with a strong bump at $3\ \mu\text{m}$; however, two main trends are seen in the mid- to far-infrared part of the spectrum; some sources have flat or rising slopes at mid-infrared wavelengths (Group I sources), while others show a steep decline towards longer infrared wavelengths (Group II sources). Meeus et al. (2001) proposed that the underlying reason for the difference in the SEDs was the geometry of the dust: where Group I sources correspond to stars with flaring disks and Group II sources to stars with flat disks. If this is the case, all sources should have similar populations of hot dust near the stars and cold dust in the disks' mid-planes; however, only sources with flaring disks should have warm dust at large distances from the stars and the presence of extended warm dust in these systems can be used to test this theory. Dullemond and Dominik (2004) showed that flaring (disks with high optical depth) and self-shadowed (disks with optical depth below some threshold) geometries are the two natural solutions for a 2D passive disk model with a puffed-up inner rim at the dust sublimation radius and proposed an evolutionary scenario in which flaring disks evolve into self-shadowed disks when the optical depth of the disk drops due to grain growth and settling of larger grains towards the mid-plane of the disk.

Previous studies of HAeBe stars at different wavelengths have confirmed the presence of extended CS dust emission. Near-infrared interferometry has probed the hotter inner regions in these systems and revealed sizes of less than 1 AU, coincident with the dust sublimation radius around these stars (Millan-Gabet 1999, 2001; Eisner et al. 2003, 2004; Monnier et al. 2005). Imaging of some of these systems in the sub-mm continuum and molecular line emission

(Mannings and Sargent 1997, 2000; Corder et al. 2005; Pietu et al. 2005) has shown gas emission regions extending hundreds of AU in size. Masses of the CS material derived from these observations are in the range of 0.01-0.05 solar masses, and provide strong evidence for the existence of optically thick disks where most of the cold mass can reside and still account for the low optical extinction observed towards the central stars. Optical and near-infrared scattered light images from HST and large ground based telescopes have revealed large (hundreds of AU) disks in some sources, sometimes immersed in more extended nebulosities (Grady et al. 1999, 2001). However, different wavelengths probe different dust populations and regions: in the near-infrared regime, the very hot dust closest to the stars dominates the emission; in mm wavelengths, images are sensitive to cold dust; and scattered light studies sample populations of very small grains distributed throughout the systems independently of their temperatures.

To fill the gap between the very hot dust and the cold dust spread throughout the systems, it is necessary to understand the distribution of the warm dust grains. This warm dust reradiates stellar radiation preferentially in the mid-infrared part of the spectrum. Only with the improvement in sensitivity and spatial resolution offered by large 8 to 10 meter telescopes, imaging circumstellar environments in the mid-infrared has become viable. As a result, very few sources have been observed and resolved in the mid-infrared (Fisher et al. 2000, Jayawardhana et al. 2001, Lagage et al. 2006, Marinas et al. 2006). In Chapter 4 I presented mid-infrared observations of the prototype Herbig Ae star AB Aurigae taken from the 8 meter Gemini North telescope. The images revealed for the first time mid-infrared emission in this system hundreds of AU in size. I also showed that the mid-infrared emission in AB Aur originated in two distinct regions: the large resolved surface of a flaring disk and a compact and unresolved region closer to the star. In this chapter I present high-resolution mid-infrared images of the remaining Group I

HAeBe stars obtained from the 8-meter Gemini telescopes as part of my imaging survey of HAeBe stars.

Observations and Data Reduction

The sources HD36112 and HD179218 were observed on October 2004 using Michelle at the Gemini North Observatory. The remaining sources were observed between August 2005 and March 2006 using T-ReCS at the Gemini South Observatory. Images were taken with the Si-5 filter and the Qa filter. The standard chop/nod technique was used to remove sky background and thermal emission from the telescope. Nearby point-spread-function (PSF) stars were observed before and after each observation of the Herbig stars. A description of the observational program and its sequence is shown in Table 5-1.

Image calibration was achieved by using mid-infrared standard stars, Table 5-2, and doing aperture photometry on the images. In addition to emission from the dust, the measured fluxes contain mid-infrared radiation from the stellar photosphere. I estimated the contribution from the stellar photospheres by approximating photospheric fluxes by blackbody fluxes using the effective temperatures of the sources presented in Chapter 3 of this work. Optical photometry in the UBV bands from Malfait et al. (1998) and Hillenbrand et al. (1992) was used to normalize the models. The average ratios of the U_o/U_m , B_o/B_m , V_o/V_m , where o stands for observed and m for modeled, were used to calculate the scale value and normalize the modeled atmospheric fluxes. For all the sources included here, stellar fluxes were negligible when compared to the total flux of the system and were not subtracted from the images.

I also used the available line fluxes from Acke and van den Ancker (2005) to estimate the contribution of the 11.2 μm PAH emission line and 11.3 μm silicate emission line to the derived 11.7 μm fluxes since these emission lines are within the Si-5 filter bandpass. Line emission

contributed more than 1% of the total flux for HD97048, HD179218, and HD169142. Total fluxes, estimated photospheric fluxes, and color-corrected warm dust fluxes after subtraction of the contribution from line emission are listed in Table 5-3.

Extended Emission

In the Si-5 filter images I spatially resolve extended emission at the FWHM level in four sources (HD97048, HD100453, HD135344, HD169142). Figure 5-1 shows the FWHM measurements for these Herbig stars and associated PSF stars in the Si-5 and Qa filter images. All seven sources are spatially resolved at the FWHM level in the Qa filter. Figure 5-2 shows the FWHM measurements for the remaining three Group I sources (HD36112, HD139614, and HD179218) and associated PSF stars. The steps followed to obtain FWHM measurements and to derive intrinsic source sizes at this level are described in Chapter 3 of this work. Sizes at the FWHM level range from 17 AU to 55 AU in the Si-5 filter images and from 22 to 55 in the Qa filter images. The ranges of sizes at both filters are the same within the errors.

In order to evaluate extension in the systems at a fainter level I subtracted the PSF from the target sources. First, we normalized all the images by dividing them by the peak fluxes in each image and multiplying them by 100. Then, all images were centered so that the peak position for HAeBe stars and their respective PSF stars were at the same position on the images and the PSF image was subtracted from the HAeBe image. The residuals in the Si-5 filter images are shown in Figure 5-3. The largest disks at this filter are HD97048 and HD169142, which are also the HAeBe stars with strongest PAH emission.

To assess the validity of the residuals, I measured diameters of this fainter emission at the surface brightness contours equivalent to 1% and 0.5% of the peak emission in the Si-5 filter, and 5% and 3% of the peak emission in the Qa filter. These specific levels were chosen so that they were more than three times the background noise for all the extended sources and their

respective PSFs. The deconvolved diameters at these levels were calculated in two different ways: using direct measurement of the diameters at the specified contours for the sources and PSF, and assuming Moffat profiles. The results from the original and modeled profiles were in good agreement with each other. Limiting sizes were estimated by increasing the measured sizes of the Herbig stars until the deconvolved size minus the error was larger than zero. I used half the spread in sizes observed at the FWHM level as an upper limit to the errors for this analysis. HD139614 is the only source not resolved at this fainter level at any filter. The remaining 6 sources have sizes from 100 to 500 AU at this fainter level. Tables 5-5 and 5-6 show measured sizes in the Si-5 and Qa filters for all resolved sources, and limiting sizes for sources with unresolved emission. Figures 5-4 and 5-5 show contour levels for all the sources and their PSF stars (lower right corner of each panel) in the Si-5 and Qa filters, respectively.

Notes on Individual Sources

HD36112

HD 36112 (MWC 758) is located in the Taurus-Auriga complex of dark clouds. Together with AB Aurigae and other well-known Herbig Ae/Be stars, HD36112 is located on a chain of young stars along the projection of the galactic equator in this region with declinations from +24 degrees to +31 degrees. Evidence of CS dust is seen in molecular line emission and near-infrared interferometric studies. Mannings and Sargent (2000) resolved CO molecular line emission and 1.3 mm continuum emission around this star, consistent with a disk in keplerian rotation with the blue-shifted wing to the east and the redshifted wing to the west. The study derived a semi-major axis of 245 AU, a PA of 116 degrees and inclination of 46 degrees for the disk. More recently, Dent et al. (2005) modeled ^{12}CO observations by a disk with an outer radius of 170 AU, an inclination angle of less than 10 degrees, and a disk mass of .04 solar masses.

Near-infrared K band interferometry resolved the inner disk region around HD36112 with a size of 0.55 AU (Monnier et al. 2005).

The mid-infrared images presented here show extended mid-infrared emission at 11.7 and 18.1 μm (central wavelengths for the Si-5 and Qa filters used in Michelle). I derive an upper limit to the size of the extended emission at the FWHM contour level of 55 AU at 11.7 μm . At this level, the 18.1 μm emission from HD36112 is resolved with a deconvolved size of 53 ± 8 AU. At the fainter level, the mid-infrared emission is also resolved with sizes of 94 AU at the contour level equivalent to 0.5% of the peak emission at 11.7 μm and 98 AU at the contour level equivalent to 3% of the peak emission at 18.1 μm . The 11.7 μm residual image, Figure 5-3, is consistent with an almost face-on disk with an inclination of ~ 20 degrees to the line of sight (assuming flat geometry).

HD97048

The star HD97048 (CU Cha) is a Herbig A0/B9 star embedded on the southeastern edge of the Chameleon I dark cloud, a region of recent star formation. Extinction toward this source is only $A_v=1.75$, less than half the average estimated extinction towards the cloud, $A_v=5.0$, implying that the star is located in the near side of the cloud (Covino 1997). The distance to the source from the Hipparcus data is 180 pc. HD97048 illuminates the reflection nebulae Ced 111 and is the brightest member of a cluster of young stars and the center of ongoing low-mass star formation (Habart et al. 2003). The recently discovered HH 921 outflow (Bally et al. 2006) seems to originate on this source or one of its companion sources. The outflow has a position angle, PA, of 100 degrees and is made of $H\alpha$ bows east and west of HD 97048, as well as $H\alpha$ filaments. The bent shape of the outflow has been interpreted as the result of interaction with the cloud in the North-South direction.

The spectrum of HD97048 shows unusual 3.43 and 3.53 μm emission features, only seen in another two stars. The features have been identified as the signature of nanodiamonds (Whittet et al. 1983, Guillois et al. 1999). The spatial distribution of this emission was resolved with a FWHM size of 32 AU (Habart et al. 2004), but their origin is still unclear. At mid-infrared wavelengths, very strong PAH emission bands dominate the spectrum of this star, with no indication of silicates (Berrilli et al. 1992). The PAH emission has been resolved in the 10 μm band extending over 1000 AU of the star (Prusti et al. 1994, van Boekel 2004, Siebenmorgen et al. 2000). Mid-infrared imaging from the VLT at 11.3 μm resolved emission closer to the star to a radius of 360 AU (Lagage et al. 2006). The emission seen in Lagage et al. (2006) shows asymmetries, with the peak of emission shifted towards the west. This asymmetry was interpreted as the result of PAH emission arising on the flaring surface of a disk with an inclination angle of 42.8 degrees. Acke and van den Ancker (2006) also resolved extended [OI] line emission consistent with a disk with a semi-major axis oriented at a PA of 160 degrees.

HD97048 shows no polarimetry variability that could indicate an intrinsic polarization of the starlight due to an inclined disk (Bastien 1985, Whittet et al. 1992, McGregor et al. 1994). In fact, the PA of polarization for HD97048 is 140 degrees and coincides with the direction of the cloud's magnetic field lines at this position. All studies of polarization in HD 97048 have shown a rotation of the PA of polarization with wavelength, which has been explained by grains in the CS environment of the source being aligned with the reflection nebula, which also has a PA of 140 degrees.

At 11.7 μm (central wavelength for the Si-5 filter used in T-ReCS) HD97048 shows the largest disk of all the HAeBe stars included in this study with an outer radius of 253 AU. The images at this wavelength present the same asymmetries seen by Lagage et al. (2006) consistent

with a flaring disk with an inclination of ~ 45 degrees to the line of sight. However, the $18.3 \mu\text{m}$ (central wavelength for the Qa filter used in T-ReCS) continuum image does not reveal any asymmetries, which is puzzling if both the PAH and continuum emission arise in the surface of a flaring disk. The measured maximum size at this wavelength is only 59 AU in radius. I do not believe the small size of the disk at this wavelength to be the result of the sensitivity of the observations; in fact, the size remains constant at 5 % of the peak emission and fainter levels in the image. The constant size implies a hard edge for the observed $18.3 \mu\text{m}$ emission at this radius. Given the complex nature of the source and its environment, I examine this source in more detail at the end of this chapter.

HD100453

With an age of 14 million years, HD100453 is the oldest star in the sample. The star is only 114 pc away and a member of the Lower Centaurus Crux association (Kouwenhoven 2005). HD100453 has been classified as a planetary nebula (Garcia-Lario 1998); however, it appears in numerous HAeBe studies (Malfait et al. 1998, Meeus et al. 2001, Viera et al. 2003). The spectrum of HD100453 shows no silicate emission band and moderate to strong PAH emission bands. The PAH emission feature at $3.3 \mu\text{m}$ is marginally resolved with a size at FWHM of 0.18 arcsec or 20 AU (Habart et al. 2006). The lack of a silicate feature suggests that large grains dominate the infrared emission on this source (Dominik et al. 2003).

Chen et al. (2006) detected a companion source southeast of HD100453 at a PA of 127 degrees and a separation of 1 arcsecond. Assuming the source is a physical companion and not a background star, they determine the star to be an M3-M4 star. The warm CS dust in this system is extended and was resolved using mid-infrared interferometry by Liu et al. (2006). Their

observations are consistent with a small disk of radius 12 AU at FWHM in the 10-12 μm region and of 15 AU at FWHM in the 18 μm filter.

We resolved mid-infrared extended emission for this source. The FWHM size is 26 AU at both wavelengths, slightly larger than those derived by Liu et al. 2006. At the fainter level this source is only ~ 45 AU in radius, being the smallest source resolved in the survey. Since the source size is the same at 1 % of the peak emission and fainter levels at 11.7 μm and at 5 % of the peak emission and fainter levels at 18.3 μm , I conclude that the derived size coincides with the edge of the mid-infrared disk and it is not the result of the mid-infrared emission falling below the detection level. The small size of the disk could result from dynamical disk clearing of the disk due to the companion source, this truncation is expected to occur at a radius of about $1/3$ the distance between the sources, which is in agreement with the derived sizes. However, given that this is one of the oldest sources in the sample, the small disk size can also be the result of the evolution of the system. I do not detect a mid-IR companion to this source. Mid-infrared emission in HD100453 is mostly symmetric and consistent with a face-on disk or small spherical halo.

HD135344

Distance estimates to the isolated Herbig Ae star HD135344 range from 88 to 140 pc. Thi et al. (2001) classified this source as an unusual debris disk based on the age they derived for the system. They used values for T_{eff} and stellar luminosity from Coulson and Walther (1995), which differ from values cited in more recent studies (van den Ancker et al. 1998, and thereafter), resulting in a much older system. The CS environment of HD135344 has large amounts of gas, making the environment of this source more consistent with proto-planetary disks than with debris disks. At mid-infrared wavelengths, HD135344 was probably resolved

from CTIO by Jayawardhana et al. (2001), but their results were inconclusive. Extended emission, consistent with a disk size of 200 AU, was detected at 20.5 μm (Doucet et al. 2006).

The mid-infrared images taken in this study show deconvolved sizes at the FWHM level of 43 ± 10 AU and 50 ± 15 AU at 11.7 and 18.3 μm , respectively. At the fainter level, residual emission for HD135344 is not symmetric, Figure 5-3. The deconvolved sizes at the contour level equivalent to 1 % of the peak emission at 11.7 μm are 190 AU and 109 AU for the semi-major and semi-minor axis respectively and 160 AU and 120 AU at the contour level equivalent to 3 % of the peak emission at 18.3 μm . Assuming that the mid-infrared emission originates in a flat inclined disk, this ellipticity translates into an inclination of 40 to 50 degrees.

HD139614

HD139614 has also been classified as a Vega-type star in different studies; however, its spectral energy distribution is typical of Group I Herbig Ae/Be stars. Silicates dominate the mid-infrared spectral energy distribution of this star. Meeus et al. (1998) interpreted the non-variability of the spectral lines in this source as indication of a disk oriented close to face-on. The spectrum of HD139614 also shows emission lines characteristic of accretion activity and winds (Hubrig et al. 1999). From ^{12}CO molecular line emission observations, the presence of a disk of mass 0.01 solar masses, outer radius of 110 AU and inclination of less than 10 degrees was derived (Dent et al. 2005). HD139614 has the largest magnetic field measured on a PMS star of intermediate mass, and the Ca II emission line shows circular variable polarization that has been explained by dust clouds or larger particles in the line of sight to the star (Yudin et al. 1999).

This is the only source not resolved at 11.7 μm at any level. I calculate FWHM deconvolved sizes of 21 ± 7 AU at 18.3 μm . At the fainter level, the signal to noise ratio of the PSF was too low to obtain reliable measurements.

HD169142

There is mounting evidence for extended emission around the isolated Herbig B9/A5 star HD169142 (MWC 925). Using differential polarimetry, Kuhn et al. (2001) detected spherical near-infrared polarized emission from scattered light with a diameter of 200 AU. ^{12}CO molecular line emission is resolved and consistent with a nearly face-on keplerian disk of mass 0.02 solar masses and outer radius of 235 AU (Raman et al. 2006, see also Greaves et al. 2000, Dent et al. 2006). The SED of this source shows no silicates and very strong PAH emission. PAH emission at $3.3\ \mu\text{m}$ is extended with a FWHM size of 0.3 arcsec or 43 AU (Habart et al. 2006).

HD169142 is the second largest source at $11.7\ \mu\text{m}$, only trailing HD97048. This is probably due to the large fraction of PAH emission contributing to the measured fluxes. At the FWHM level, I derive deconvolved sizes of 55 ± 17 AU and 38 ± 6 AU at 11.7 and $18.3\ \mu\text{m}$, respectively. These sizes are the same within the errors. At the fainter level, the mid-infrared emission is spherically symmetric consistent either with a disk viewed face-on or an envelope. The intrinsic sizes at this fainter level are 144 AU at $11.7\ \mu\text{m}$ and 77 AU at $18.3\ \mu\text{m}$ consistent with sizes derived from near-infrared polarization studies.

HD179218

HD179218 (MWC 614) is an isolated Herbig Ae star. At mid-infrared wavelengths the spectrum of this source shows very high levels of crystalline silicates (Meeus et al. 2001), including cold enstatite, which is only found on this star. Since crystallization is thought to start in the innermost very hot regions of CS environments, the presence of enstatite in the outer colder regions of the CS environment of HD179218 might be indicative of a more turbulent and massive environment favorable to a more efficient mixing of processed material around the star (van Boekel et al. 2005). $\text{H}\alpha$ emission line studies of HD179218 showed that the line profile

consisted of a sharp peak and a weakly variable absorption on the blue wing of the profile with a period of about 10 days (Miroshnichenko et al. 1999, Kozlova 2004). The profile of the H α emission line could be explained if the line originates in a disk wind. Goodson et al. (1999) showed that magnetic field in an accretion disk causes the formation of a disk wind that creates streams of gas variable on these timescales. Additional long-term variability in the Na I doublet that might be explained by accretion of gas into a companion source was also observed (Kozlova 2004); however, there is no known companion source to HD179218.

Dent et al. (2005) detected ^{12}CO emission for HD179218 and derived the presence of a disk with an outer radius of 120 AU, an inclination of 40 degrees, and a total mass of .01 solar masses. More recently, Liu et al. (2006) detected for the first time extended emission on this source using 10 μm nulling interferometry with adaptive optics. They modeled their results using a Gaussian disk and derived disk sizes at the FWHM level of 20 AU.

HD179218 is the farthest source in this sample. The derived FWHM deconvolved size at 18.1 μm is 24 ± 8 AU, consistent with the result at 10 μm of Liu et al. (2006). At the fainter level I detect spherically symmetric emission out to a radius of 82 AU at 11.7 μm and 47 AU at 18.1 μm .

HD97048: An Alternative Scenario

Our 11.7 μm image, where PAH emission dominates, confirms the asymmetries and extension seen in the Lagage et al. (2006) image, and can be interpreted in the context of a flaring disk with an inclination of about 45 degrees to the line of sight. However, the 18.3 μm continuum image, does not show the same asymmetries, which is a puzzling result if both the PAH and the continuum emission arise in the surface of a flaring disk.

The difference in the sizes of extended emission can be understood if different grains are responsible for the emission observed at each filter. PAH emission arises in very small transiently heated grains, which are heated to high temperatures and re-radiate at a specific wavelength independently of their distance to the star. The emission seen in the PAH bands images is fainter at larger distances because of lower density at larger radii, but not because of lower dust temperatures. Thermal continuum, on the other hand, depends on the temperature and the density of the grains, and both depend on the distance to the heating source. Based on this, I could expect to see the continuum emission arising from a smaller area than the PAH emission even if the emitting grains have identical spatial distributions.

However, if the morphologies in the images are real, the PAH and continuum emissions have to originate in different regions. If dust grains populate the surface layer of a flaring disk, and the asymmetry arises from the disk inclination with respect to the line of sight, I expect to see a similar asymmetry in the continuum emission images, which is not the case. Figure 5-6 shows the expected emission at 10 and 20 μm for a flared disk with an inclination of ~ 45 degrees (Dullemond & Dominik 2004), the asymmetries are visible at both wavelengths. To verify that the observed difference was not the result of the lower resolution at 18.3 μm , I degraded the resolution of the 11.7 μm image to match the resolution at 18.3 μm by convolving the 11.7 μm image with the 18.3 μm PSF. The asymmetries observed in the PAH band were still clearly visible, Figure 5-7. Therefore, I have to assume that the difference between the continuum emission and the PAH emission is intrinsic to the system and not an artifact of the observations.

While the flaring disk model describes well the PAH emission images, multi-wavelength observations seem to point to a more complex dust distribution. From the 10 μm observations

alone, dominated by PAH emission, optically thin emission is seen extending over very large distances. Prusti et al. (1994) modeled this emission as an optically thin halo with a large inner hole. I might take this interpretation and assume that the PAH emission and continuum emission are sampling different structures within the system, with the PAH emission located in a more extended optically thin halo, and the continuum emission tracing the surface of a more compact disk inside a cavity in the halo. The strong PAH emission seen in the images and on the Lagage et al. (2006) images will be dominated by the inner walls of the optically thin shell. In this scenario, the observed asymmetry in the PAH emission bands can be the result of interaction of the large envelope with the cloud.

Numerous studies seem to point in that direction: the PA of polarization for HD97048 is aligned with the cloud magnetic field lines, the star is embedded on the edge of the cloud, Figure 5-8, and is moving towards regions of higher density in the cloud. HD97048 has a proper motion in RA of -20 mas/yr or -17 km/s, no proper motion in declination and a heliocentric radial velocity of 34 km/s (Ducourant et al. 2005). Another indication that the geometry might be the result of interaction with the cloud is that a similar asymmetry is observed around the Chameleon I infrared nebula, Cha IRN, also located in the same region. The IRAS images of the large nebula associated with these systems, Ced 111, shows multiple mid-infrared sources at $12\ \mu\text{m}$, but at longer infrared wavelength HD97048 and Cha IRN dominate the emission, Figure 5-9. The H band polarization map of Cha IRN shows a similar asymmetry to HD97048, with the peak of emission also shifted towards the west, Figure 5-10.

In addition to the morphological differences seen in the Si-5 and Qa images, there is also evidence of positional offsets between the star (optical position) and the peak of emission observed at other wavelengths. If the emission observed at any wavelength arises in a disk

surrounding the central star, and the inclination of the disk allow us to see the star, the peak of emission from circumstellar dust will be close to the star and since we cannot resolve the inner regions of the system, the peak of emission observed should coincide with the optical position of the star. There are some indications of this effect in previous studies of HD97048. The optical and near-IR positions for this source overlap; however, the IRAS peak of emission is shifted towards the NW of the source. The offset is larger than the IRAS positional error ellipse. The same effect is seen on the mm images of Henning 1998, Figure 5-11, in which they pointed out that the observed positional offset for HD97048 was larger than the positional errors of the observation.

The astrometry accuracy listed by Gemini Observatory for mid-infrared chop-nod observations not planned for high accuracy is low, about 1 arcsec. Nevertheless, I performed astrometry in the images by using the coordinates recorded for a given reference pixel in each T-ReCS image, and measuring the offset of the observed peak of emission from the optical position entered in the observation. I also measured the offset between the 11.7 and 18.3 μm peaks. As a reference, I also calculated positional offsets for the PSF star, where no shift is expected under perfect pointing. For the PSF star, the maximum offset between the 11.7 μm images and the optical position was 0.4 arcsec both in RA and Dec, the maximum offsets between the 18.3 μm images and the optical position were 0.4 arcsec in RA and 0.6 arcsec in Dec, and the maximum offsets between the 11.7 and 18.3 μm images for the PSF were 0.2 arcsec in RA and 0.4 arcsec in Dec. The total offsets were 0.6 arcsec (11.7 μm to optical), 0.7 arcsec (18.3 μm to optical) and 0.4 arcsec (11.7 μm to 18.3 μm). All these offsets are lower than the astrometry accuracy of 1 arcsec listed by Gemini; therefore, there is no positional offset for the PSF star. For HD97048, the offsets between the 11.7 μm images and the optical were 0.9 arcsec in RA and 1.5 arcsec in

Dec, the offsets between the 18.3 μm images and the optical were 0.7 arcsec in RA and 0.8 arcsec in Dec, and the offsets between the 11.7 and the 18.3 μm images were 0.2 and 0.8 arcsec in Dec. The total offsets were 1.8 arcsec (11.7 μm to optical), 1.1 arcsec (18.3 μm to optical) and 0.8 arcsec (11.7 μm to 18.3 μm). These offsets are larger than the ones seen in the PSF images, especially at 11.7 μm where the offset in Dec is almost twice the astrometry accuracy of Gemini. Like in the IRAS and mm images, the mid-infrared peaks of emission are seen to the NW of the optical position, with the 11.7 μm peak farther out, Figure 5-12. Even with low astrometry accuracy, the offset of the 11.7 μm peak of emission relative to the optical position of HD97048 is evident. The 18.3 μm peak is also offset; however, the positional offset is close to the positioning errors and future multi-wavelengths observations of HD97048 planned for high astrometric accuracy should be planned to clarify this issue.

These images of HD97048 reveal the importance of multiwavelength observations to address the structure of a system. The different sizes, morphologies and positional offsets observed here together with the evidence for interaction of this system with the nearby molecular cloud and positional offsets of the star with observations at longer wavelength cannot be explained in the flaring disk scenario. The theory of an optically thin halo thousands of AU in size with a large inner hole proposed by Prusti et al. (1994) with an embedded small disk might explain these inconsistencies.

Spherical Emission: Flaring Disk or Envelope?

In the analysis of the AB Aurigae system, I showed that if I assumed a flat disk of inner radius 0.5 AU, outer radius of 400 AU, thickness of 10 AU, a uniform dust density, and the derived cold dust mass from mm studies, I could calculate the optical depth along the plane of the disk and estimate how far into the disk stellar radiation could penetrate. In that case I derived

an upper limit of 2 AU for the disk to become optically thick to stellar radiation. Because the cold dust masses derived from mm studies in all the sources included in this chapter are larger than those calculated for the AB Aurigae system, I can safely conclude that under the same assumptions, all these systems are also optically thick to stellar radiation at the disk mid-plane if they are surrounded by flat or flaring disks. Therefore, the presence of warm optically thin dust at large radii implies that the dust has to be heated by direct radiation from the star located either above or below the disk mid-plane. The dust could reside either on the surface of a flaring disk or on a halo.

In Chapter 4, I also calculated the optical depth of a system perpendicular to the plane of the disk at mid-infrared wavelengths, which indicates whether I am detecting emission above and below the disk mid-plane (if the disk is optically thin to mid-infrared radiation) or just above the disk mid-plane (if the disk is optically thick to mid-infrared radiation). In the case of AB Aurigae I determine that the disk remained optically thick out to a radius of 118 AU and, therefore, I was only detecting infrared radiation from the surface closest to us. The same conclusion can be extended to the other sources presented here since they are at least as massive as AB Aurigae. A detailed analysis leading to these results is shown in Chapter 4 of this thesis.

Geometry of the Systems: Disks or Haloes?

The radial distribution of grain sizes provides information about the geometry of the system. Small grains in a region optically thin to stellar radiation, like the surface layer of a flaring disk or a halo, experience the effect of radiation pressure. Smaller grains are pushed outward because radiation pressure overcomes the gravitational force, while larger grains stay closer to the star and in the disk mid-plane. In the flaring disk approximation, it is expected that larger grains in the disk dominate in the inner regions closer to the star, and smaller grains in the surface layer of the disk dominate in the outer regions. In the disk plus halo scenario, the line of

sight to the system intercepts more halo material near the star, and only graze the halo in the outer regions. As a result, average particle sizes near the star will be weighted toward the smaller particles in the halo, while larger grains concentrated in the disk will dominate the average particle sizes derive in the outer regions. Knowledge of the radial distribution of grains dust sizes can then be used to discriminate between these two scenarios for spherically symmetric systems.

To study the properties of the dust as a function of distance to the star, the angular sizes of the mid-infrared emission observed in the Si-5 and Qa images should be large enough at both filters to subdivide them into independent annular regions of width Δr larger than the resolution element of the observations. With the exception of AB Aurigae, presented in Chapter 4, this analysis is only possible for HD169142.

The images of HD169142 were first cross-convolved to the same resolution (the Si-5 image was convolved with the Qa PSF, and the Qa image was convolved with the Si-5 PSF). Then the mid-infrared emission from HD169142 was divided into three rings of width $\Delta r = 90$ AU (0.62 arcsec). This is equivalent to 1.4 and 1.1 times the resolution element of these observations at 11.7 and 18.3 μm respectively. Average flux density ratios (11.7/18.3) for the circumstellar dust within each region were 0.32, 0.38, and 0.37. I then calculated the expected flux ratio for particles of different properties as a function of distance to the star by using the temperature of the grains as outlined in Chapter 3 of this work. This is possible because the expected flux ratio of a dust particle depends on the properties of the material, the sizes of the grains, and the distance to the heating source. I then assigned the observed flux ratios values to the midpoint of each region to constrain the characteristic grain sizes for each region. Figure 5-13 shows the expected ratio of thermal emission from different dust grains and the observed values. Using the λ_0 value from the plot that matches the observations and assuming moderately

absorbing grains, I derived particle sizes of 6.0, 0.5, and 0.2 μm for the three regions, with the largest particles closest to the star. There are high uncertainties in this method because I am not taking into account the PSF to calculate distances, I am not including photometric calibration errors, and I am assuming a very simplified model for the dust grains; however, since these uncertainties will affect the all regions equally and we are only interested in the average grain sizes in the regions relative to each other, and not in deriving realistic dust grain sizes, this approach is justified. As in the case of AB Aurigae, this result suggests that I need different grain sizes to fit the observed flux densities at different distances from the star, with smaller grains farther from the star and larger grains at smaller radii.

This segregation of particle sizes can be explained if the dust grains dominating the mid-infrared emission reside in an axisymmetric structure like the flaring surface of a disk, but not if the dust grains are located in a spherical envelope. Therefore, the most extended and spherically symmetric Group I sources included in this survey, AB Aurigae and HD169142, provide observational evidence of the presence of axisymmetric circumstellar dust distributions in these systems.

Conclusions

I have observed 8 (7 sources presented here plus AB Aurigae, Chapter 4) Group I Herbig Ae/Be stars in the mid-infrared with high spatial resolution. For 7 sources, extended emission is resolved in the Si-5 and Qa filter at the FWHM level and fainter brightness levels. The exception is HD 139614, which was only resolved at the FWHM level at 18.3 μm . At the fainter levels 5 sources show spherical emission consistent with disks' orientations close to face-on, while two sources HD135344, and possibly HD97048, show asymmetries expected for disks inclined 40 to 50 degrees to the line of sight. HD97048 is a special case since the emission at

18.3 μm is spherically symmetric, while the 11.7 μm emission is not. For all sources the measured sizes (or limiting sizes) at the FWHM level are the same within the errors at both wavelengths, but at fainter levels HD97048 have very different sizes at both wavelengths.

The different sizes observed in the PAH filter (~ 500 AU) and the Qa filter (~ 100 AU) for HD97048 might result from the large fraction of PAH emission in this system. However, HD169142 has a larger contribution of PAH emission (Acke and van den Ancker 2005) and the observed sizes in the Si-5 and Qa filters are still the same. Besides different sizes for the extended emission, the images of HD97048 show different profiles in the two filters: the peak of emission in the Si-5 profile is shifted to the right, while the Qa profile is centrally peaked. In addition, the peaks of emission observed in these images are shifted to the NW relative to the optical position of the star. The positional offset of the peak of emission in the Qa image is 1.1 arcseconds, close to the astrometry accuracy of 1 arcsecond of these observations; however, the offset of the peak of emission in the Si-5 image is offset by 1.8 arcseconds. Future observations with high astrometry accuracy should be able to explore this in more detail. If both emissions arise in the flaring surface of a disk inclined to the line of sight, both images should show the same asymmetry (either centrally peaked or shifted to the right) and the peak of emission should coincide with the position of the star. Therefore, I propose that emission for HD97048 arises from different components in the system and not from an inclined flared disk as previously thought.

The extended emission resolved in these systems confirms the presence of optically thin dust heated by stellar radiation at large distances from the central star, either the surface layer of a flaring disk or a halo. However, the observed segregation of dust grain sizes, with smaller grains at larger radii and larger grains closer to the stars that we derived for the two largest and

spherically symmetric systems included in this survey (AB Aurigae and HD169142) is inconsistent with halo models and supports thermal emission from grains on the surface of flaring disks. This study does not exclude the presence of more extended haloes in these systems; in fact, many of the sources are surrounded by large-scale emission; but the observed mid-infrared emission detected in this study is not arising in a spherical component.

I derived outer disk radii of 50 to 250 AU for these sources, with the smallest resolved disk belonging to the oldest star in the sample, HD100453. The disk size in this source could also result from disk truncation due to tidal interaction with the companion star detected by Chen et al. (2006). The companion source is not detected in the mid-infrared images presented here.

Table 5-1. Log of observations.

Program ID	UT Date	HD #	Filter	On-source Time	PSF PPM #	Flux Standards
GN-2004B-Q-91	10/03/2004	179218	Si-5, Qa	645	136291	HD176670, HD1255
	10/05/2004	36112	Si-5, Qa	645	70153	HD1632, HD180450
GS-2005B-Q-7	8/21/2005	135344	Si-5, Qa	608	320766	HD133774, HD156277
	8/21/2005	169142	Si-5, Qa	608	267912	HD133774, HD156277
	9/09/2005	139614	Si-5	608	320766	HD156277
	3/10/2006	139614	Qa	608	320766	HD169916, HD133774
	2/06/2006	97048	Si-5, Qa	608	370812	HD110458, HD133774
	2/06/2006	100453	Si-5, Qa	608	340310	HD110458, HD133774
	9/08/2005	163296	Si-5	608	267912	HD169916
3/12/2006	163296	Qa	608	267912	HD156277	

Table 5-2. Standard stars photometry

HD #	F (Si-5) [Jy]	F (Qa) [Jy]
1255	10.2	4.05
1632	6.47	2.55
110458	3.99	1.72
133774	8.87	3.78
156277	5.26	2.11
169916	22.2	8.95
176670	6.66	2.64

Table 5-3. Derived flux measurements.

HD #	Observed Flux (Jy)		Color-Corrected Flux (Jy)		BB Photosphere (Jy)		Dust Continuum Flux (Jy)	
	Si-5	Qa	Si-5	Qa	Si-5	Qa	Si-5	Qa
36112	4.80	8.58	4.80	8.90	0.02	0.01	4.78	8.57
97048	6.81	20.97	6.80	21.73	0.01	0.00	6.80	20.96
100453	6.77	27.10	6.75	28.07	0.04	0.02	6.73	27.08
135344	1.21	3.51	1.21	3.64	0.03	0.01	1.18	3.50
139614	4.40	13.90	4.39	14.40	0.02	0.01	4.37	13.89
169142	2.87	11.60	2.86	12.01	0.02	0.01	2.84	11.59
179218	19.48	37.93	19.49	39.33	0.01	0.00	19.47	37.93

Table 5-4. Quadratic subtracted sizes in the Si-5 filter for all Group I sources. The sizes are the result of quadrature subtraction as explained in the text. This gives an accurate result at the FWHM; however, it underestimates sizes at the other brightness levels where the profiles significantly deviate from a Gaussian function. An asterisk over a number implies limiting sizes.

HD #	D (pc)	Sizes (arcseconds)					Sizes (AU)				
		50%	error	1%	0.50%	Range	50%	Error	1%	0.50%	range
31293	144	0.12	0.03	0.66	0.80	0.02	17	4	95	115	3
36112	204	0.27*		0.40	0.46	0.25	55*		82	94	51
97048	180	0.23	0.03	1.22	1.40	0.06	41	5	220	252	11
100453	112	0.23	0.06	0.51	0.51	0.11	26	7	57	57	12
135344	140	0.31	0.07	0.58	0.70	0.10	43	10	81	98	14
139614	140	0.26*					36*				
169142	145	0.32	0.10	0.86	0.99	0.19	47	14	125	144	28
179218	240	0.10*		0.32	0.40	0.02	24*		65	82	4

Table 5-5. Quadratic subtracted sizes in the Qa filter for all Group I sources. Same as Table 5-4, but for the Qa filter.

HD #	D (pc)	18 μ m Deconvolved Sizes (arcseconds)					18 μ m Deconvolved Sizes (AU)				
		50%	error	5%	3%	range	50%	Error	5%	3%	range
31293	144	0.15	0.03	0.60	0.62	0.02	22	4	86	89	3
36112	204	0.26	0.04	0.41	0.48	0.09	53	8	84	98	18
97048	180	0.18	0.06	0.29	0.29	0.04	32	11	53	53	7
100453	112	0.23	0.06	0.39	0.38	0.08	26	7	44	43	9
135344	140	0.36	0.11	0.44	0.48	0.18	50	15	62	67	25
139614	140	0.15	0.05								
169142	145	0.26	0.04	0.49	0.53	0.06	38	6	71	77	9
179218	240	0.1	0.04	0.18	0.23	0.01	24	8	37	47	2

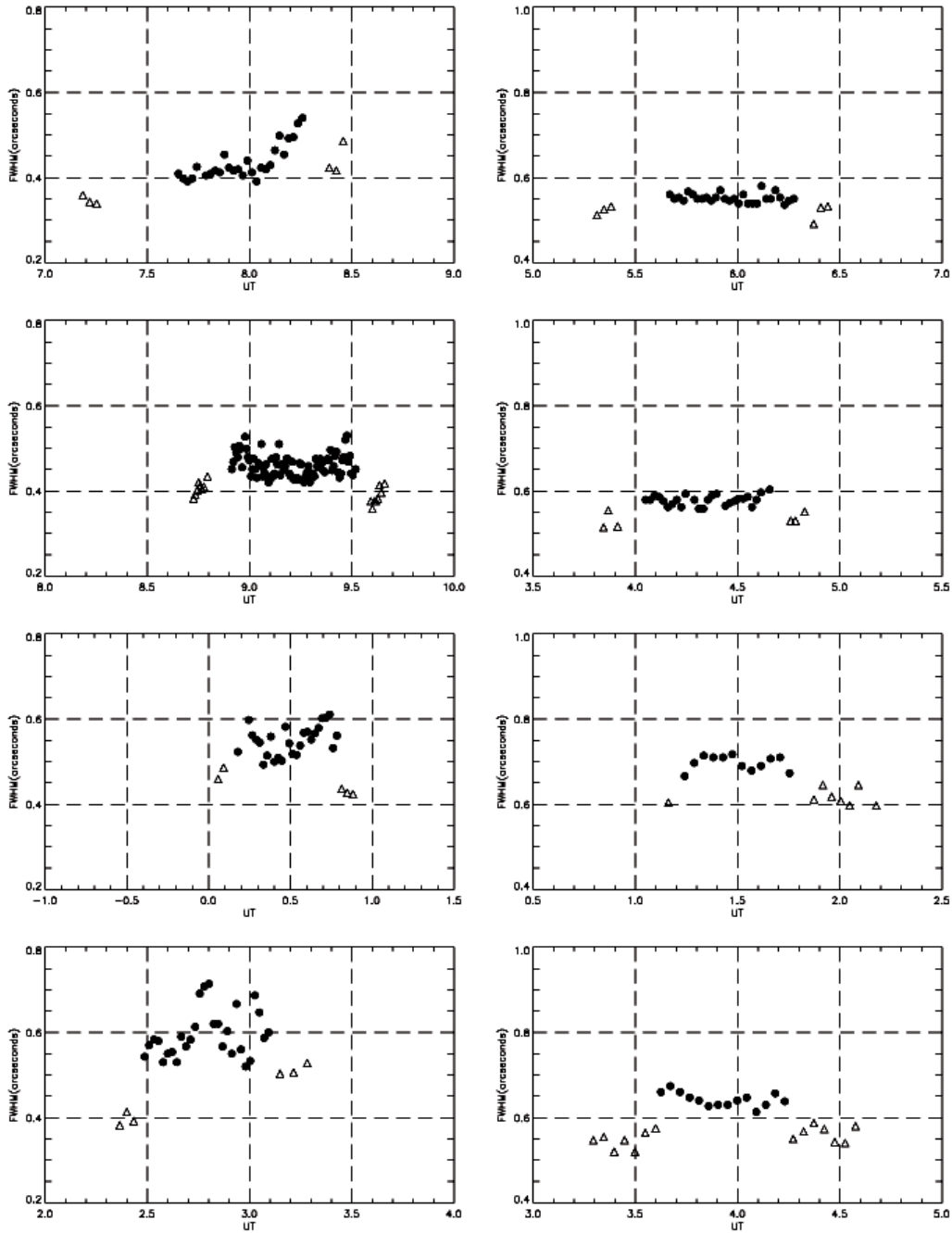


Figure 5-1. Clearly resolved sources in the sample. Variations in the FWHM measurements of Herbig Ae/Be stars (black circles) and PSF stars (triangles) are due to changes in the seeing during the observations. The x-axis shows the UT time of the observations. The first column are measurements in the Si-5 filter while the second column shows the measurements in the Qa filter. From top to bottom, the sources in this plot are HD97048, HD100453, HD135344 and HD169142. To measure the FWHM size of HD97048 I only used the first set of points where the seeing was stable.

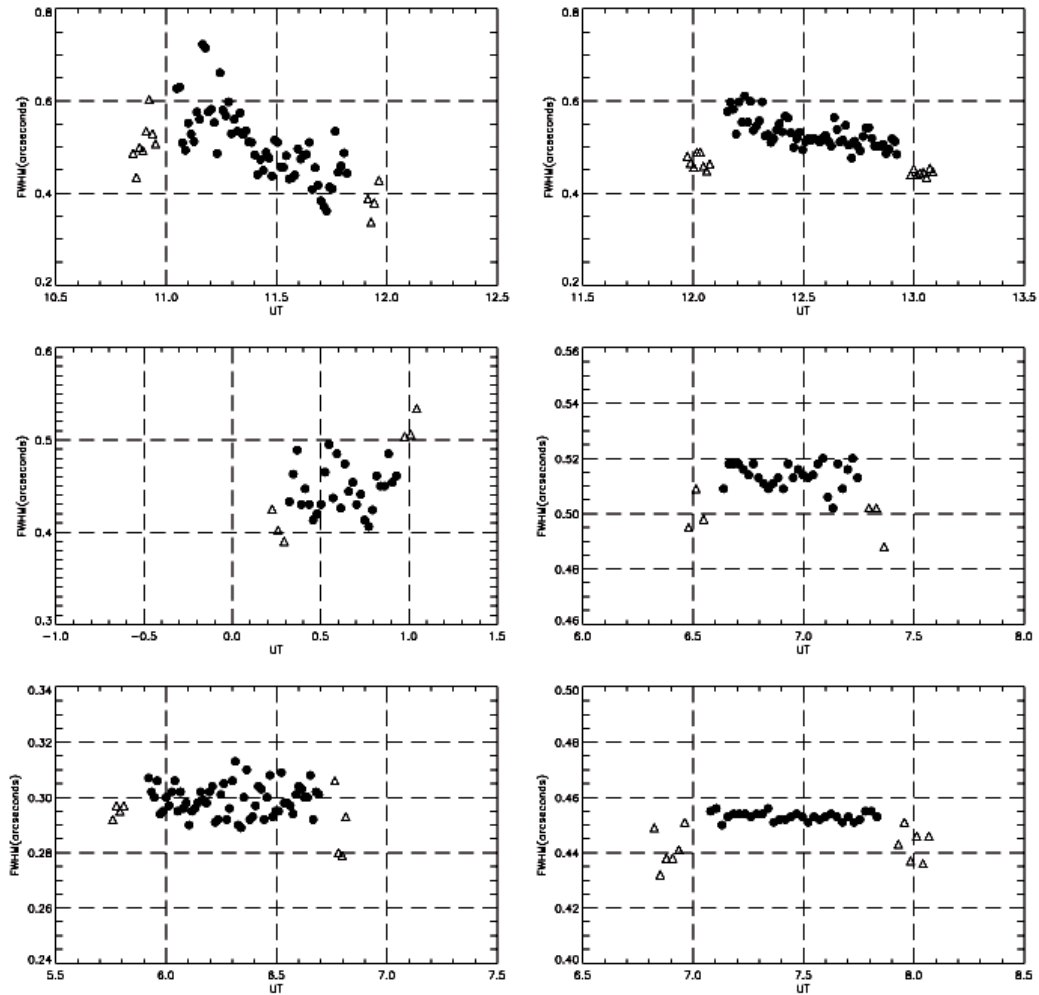


Figure 5-2. FWHM measurements for HD36112, HD139614, and HD179218 (top to bottom). Like in the previous figure, the first column shows the Si-5 filter measurements and the second column shows the Qa filter measurements. Black circles are used to represent Herbig Ae/Be stars and open triangles to represent PSF stars. Errors due to changes in the seeing in the Si-5 filter during these observations were larger than the calculated sizes. However, all three sources are resolved in the Qa filter.

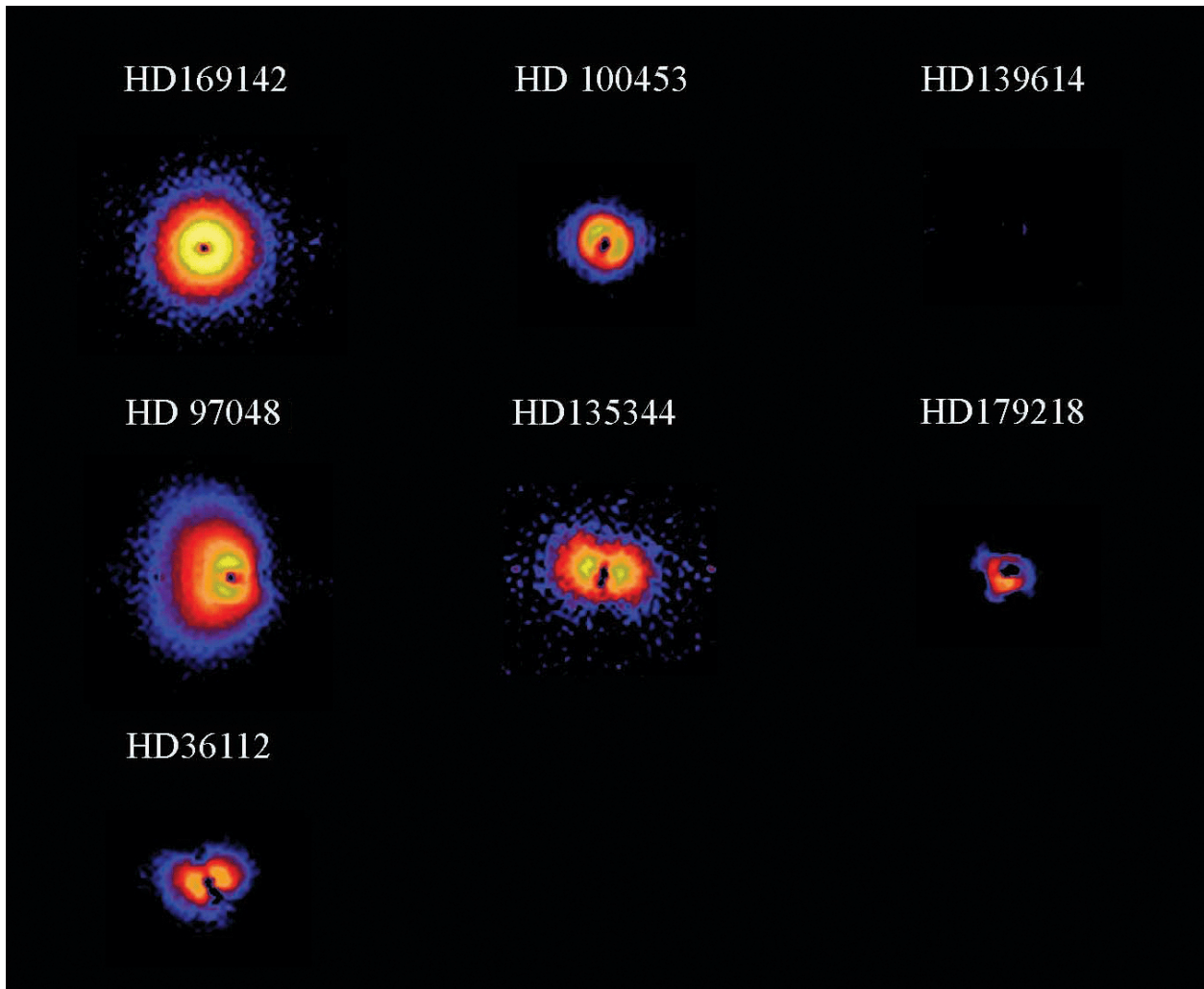


Figure 5-3. Residuals after subtraction of the normalized PSF in the Si-5 filter. All sources were normalized to the same peak of emission in order to evaluate extensions on the sources. At this wavelength, HD169142 and HD97048 are the more extended sources. This is expected since they are also the sources with larger PAH emission at this wavelength. The residuals for HD179218, HD36112 and, specially, HD139614 are compromised due to changes in the seeing during the observations.

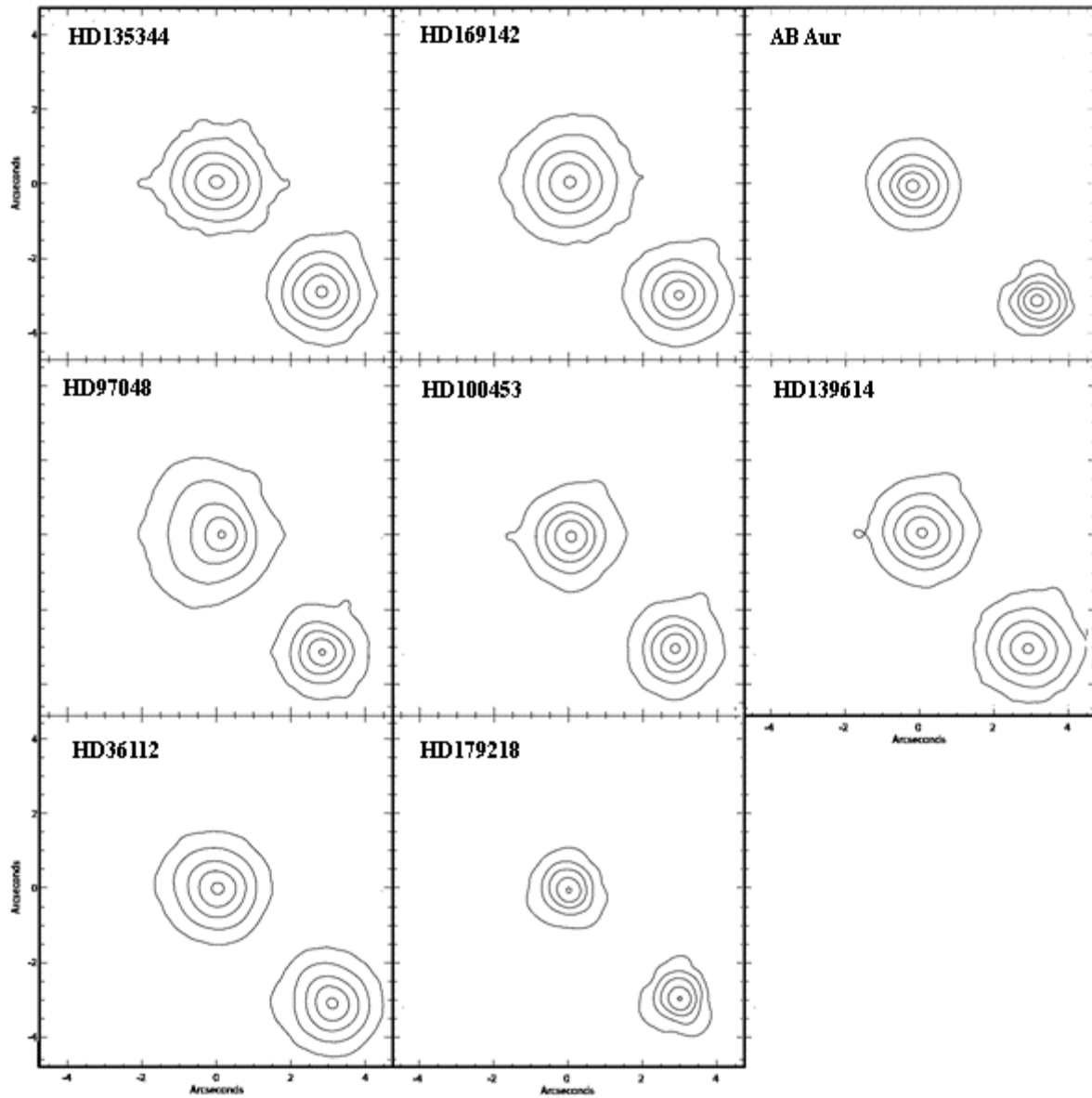


Figure 5-4. Group I sources and PSF stars in the Si-5 filter. The images were normalized so that the science sources and the PSF sources have the same maximum flux density. Lowest contours are 0.5 % of the peak of emission in all cases. PSF sources are in the lower right corner of each panel.

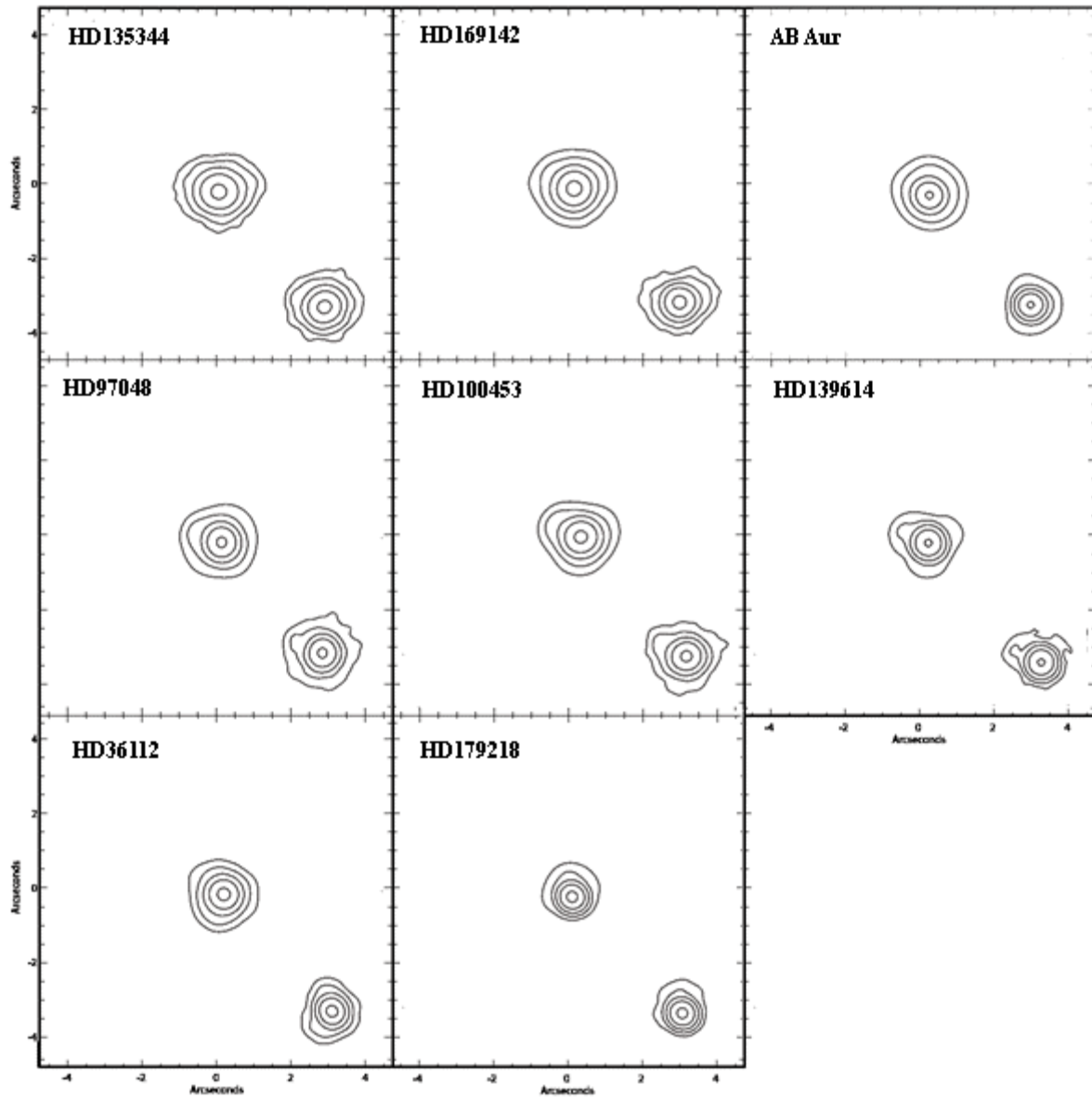


Figure 5-5. Group I sources and PSF stars in the Qa filter. The images were normalized so that the science sources and the PSF sources have the same maximum flux density. Lowest contours are 3 % of the peak of emission in all cases. PSF sources are in the lower right corner of each panel.

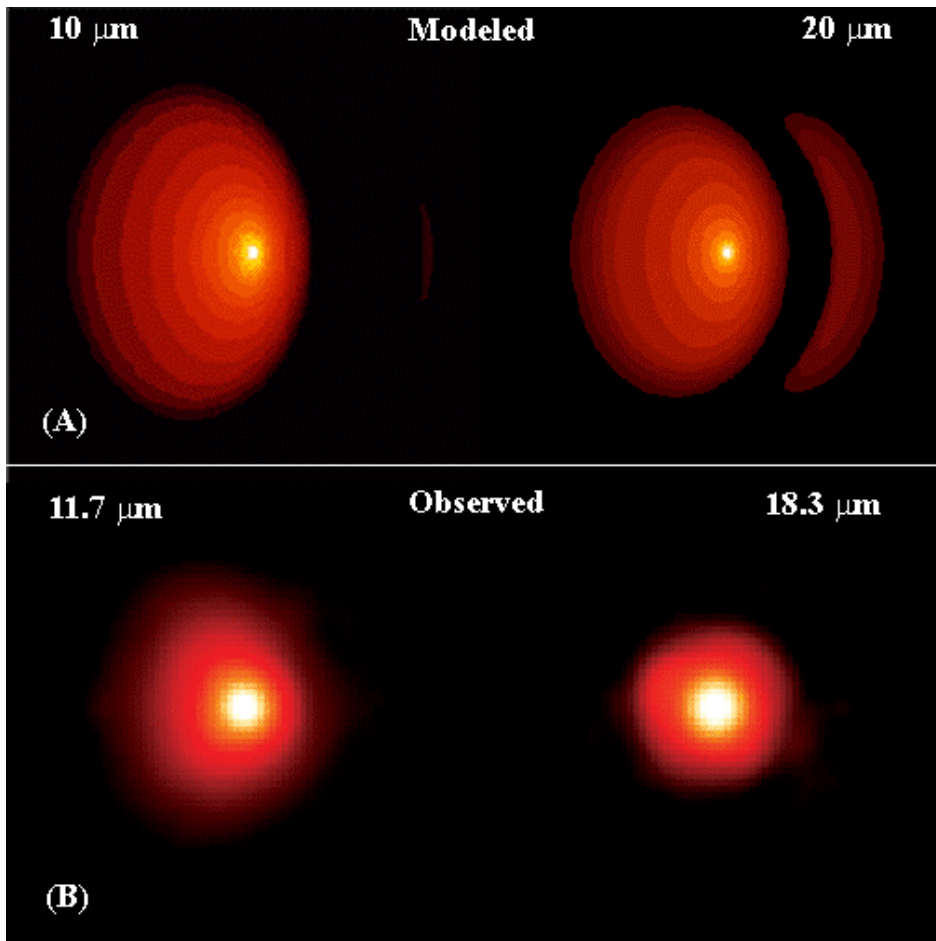


Figure 5-6. Modeled and observed emission from a flared disk with an inclination of ~ 45 degrees (A) Expected emission from Dullemond (2001). (B) Observed mid-infrared images of HD97048.

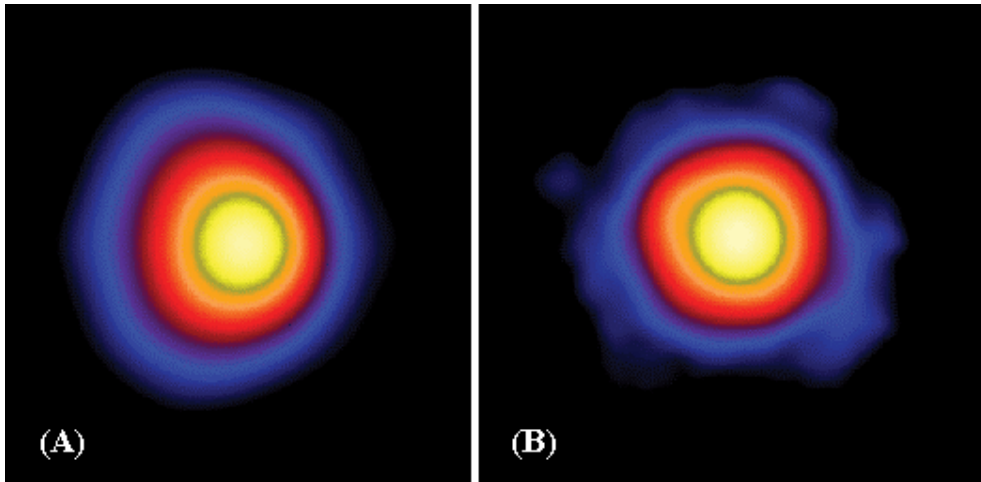


Figure 5-7. HD97048 cross-convolved Gemini images (A) Si-5 image convolved with the Qa PSF image. (B) Qa image convolved with the Si-5 PSF image. The asymmetries are still visible in panel (A).

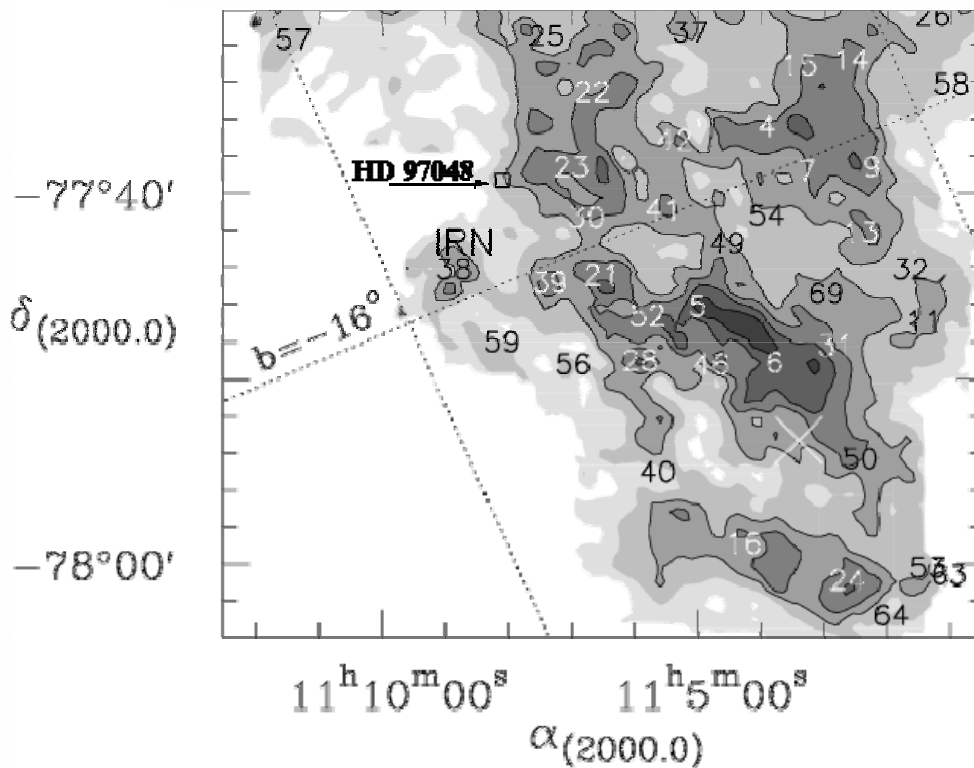


Figure 5-8. Location of the Herbig star HD97048 on the southeastern edge of the Chameleon I dark cloud. The image shows the $C^{18}O$ map of the ChaI dark cloud (Haikala 2005). The location of the nearby Infrared Nebula (IRN) is also labeled. Numbers correspond to other sources mentioned in the above study.

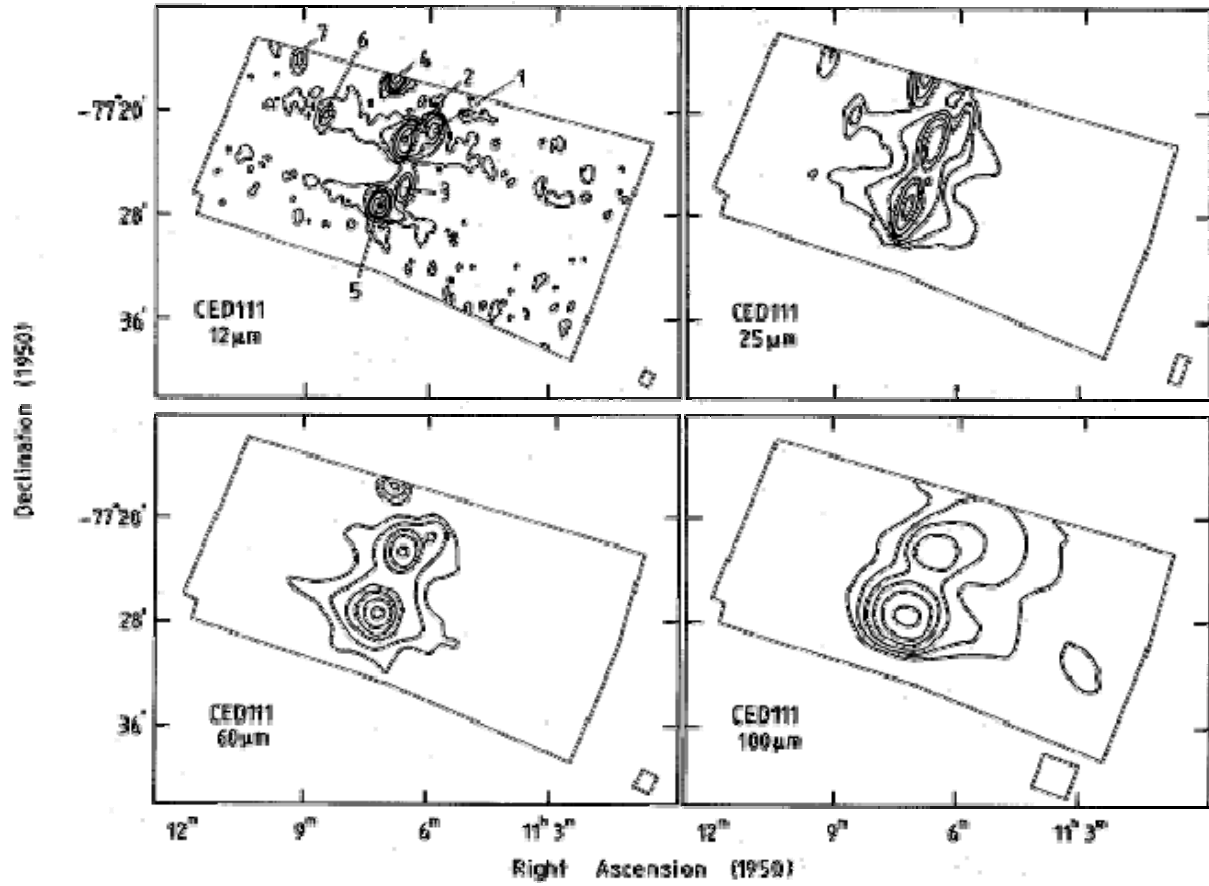


Figure 5-9. IRAS images of the Ced111, reflection nebula associated with HD97048. HD97048 is source number 2 in the first panel. Other IRAS sources are also visible at 12 μm. At longer infrared wavelengths, HD97048 and Cha I IRN (source 5 in the first panel) dominate the emission (Assendorp et al. 1990).

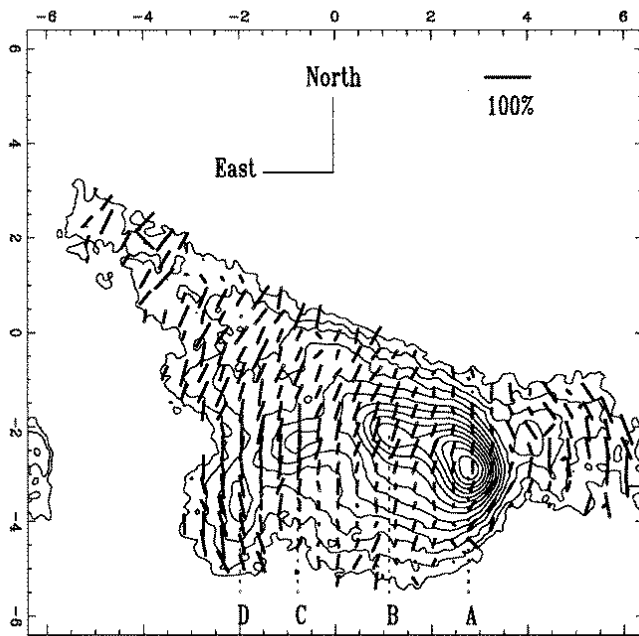


Figure 5-10. H band polarization map of Cha I IRN. The observed geometry of the source is similar to the geometry of the PAH emission in HD97048. (Ageorges et al. 1996)

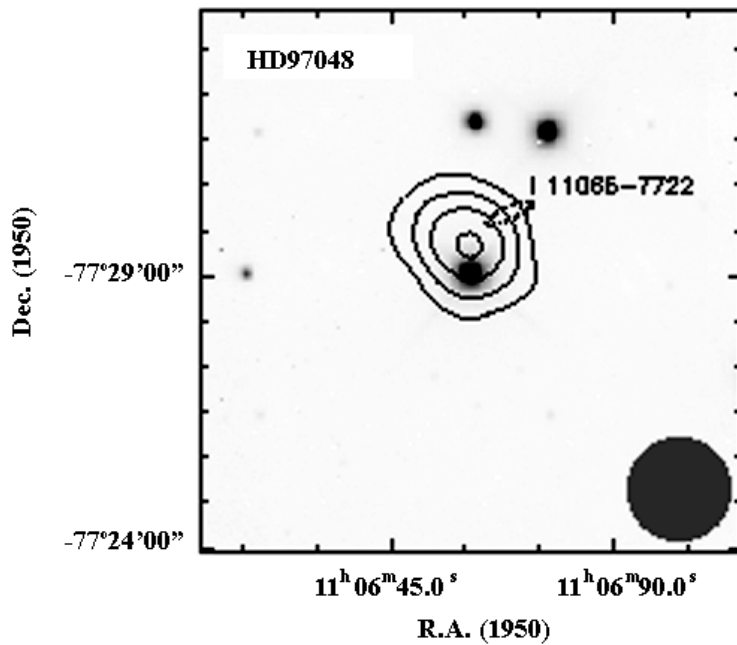


Figure 5-11. 1.3 mm observations of HD97048 showing the offset of mm emission relative to the optical and near-infrared source position (Henning 1998).

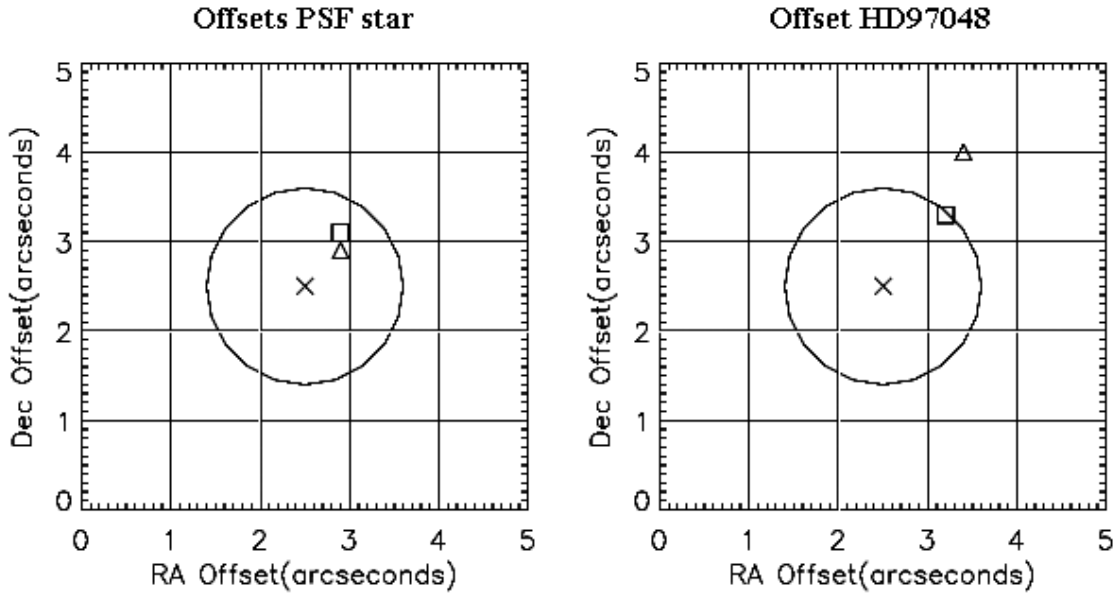


Figure 5-12. Offset of the Si-5 and Qa peak of emission relative to the optical position of HD97048 (left panel) and PSF star (right panel). The circle shows the 1 arcsec astrometry accuracy listed by the Gemini website for regular mid-infrared chop-nod observations.

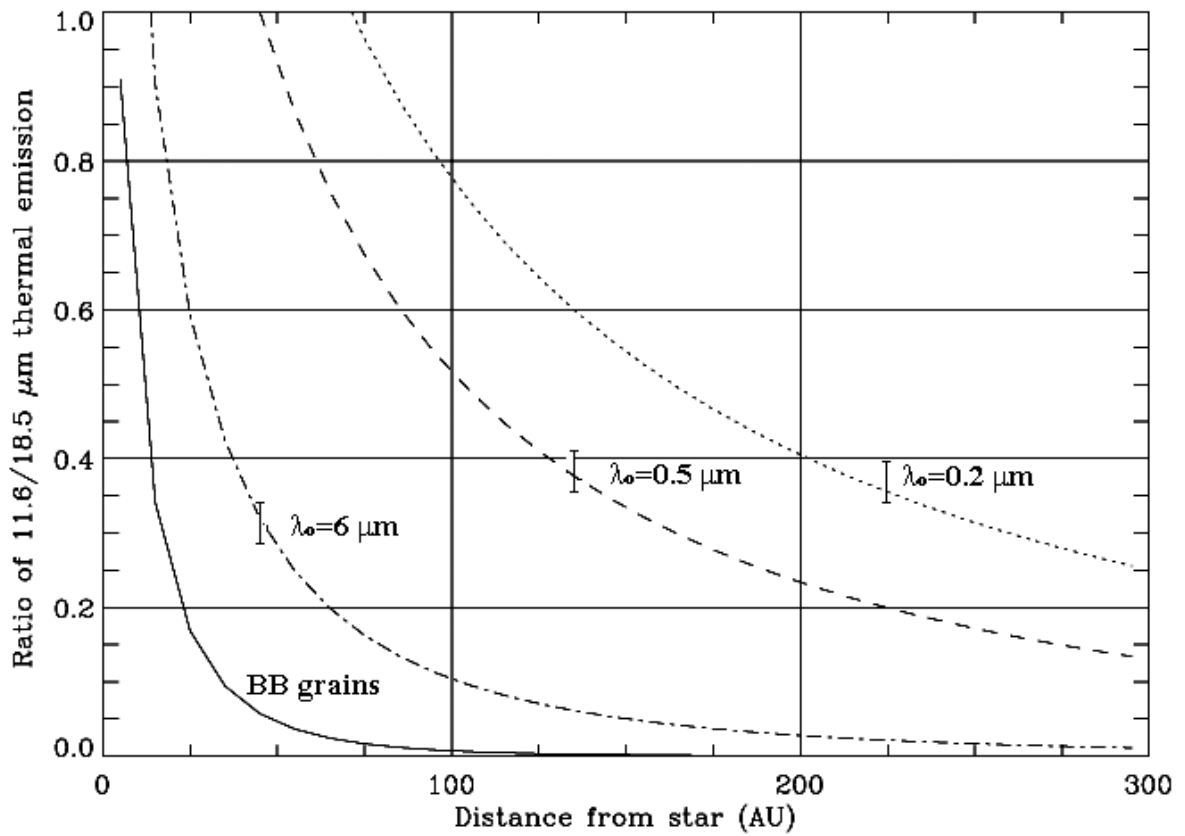


Figure 5-13. Ratio of the thermal emission at 11.7 and 18.3 μm for different values of λ_0 . Grain sizes equal λ_0 for moderately absorbing material, or $\lambda_0/2\pi$ for strongly absorbing materials (Backman & Paresce 1993). The observed ratio of flux densities for the regions 0-90, 90-180, and 180 to 270 AU measure for HD169142 are shown at the mid-point of the three regions at 45, 135, and 225 AU from the star, respectively. The error bars represent the relative uncertainties in the flux measurement ratios due to centering of the regions.

CHAPTER 6
RESOLVING HERBIG Ae/Be PROTOPLANETARY DISKS IN THE MID-INFRARED: THE
GROUP II SOURCES

Introduction

Herbig Ae/Be classified as Group II sources (Meeus et al. 2001) stars have spectral energy distributions with a declining slope in the mid- to far-infrared regime. Contrary to Group I sources which have flaring protoplanetary disks, the disks in Group II sources are expected to be flat (Meeus et al. 2001, Dullemond et al. 2004). If this is the case for all Group II sources, since these systems are optically thick to stellar radiation, the dust in the disk will be cold and the large mid-infrared excesses observed in the systems should arise uniquely from the inner regions of the disks. No extended emission should be detectable at larger distances in the mid-infrared.

Many of these sources classified as Group II sources are UX Orionis-type stars (Dullemond et al. 2003) showing irregular photometric variability (UXOR behavior). The V light from the star drops in brightness by up to 3 magnitudes, with durations of days or weeks. During these minima, the light from the sources gets reddened and become more polarized, and at very deep minima, there is an observed color reversal where the light becomes bluer (Bibo and The 1991). This behavior has been associated with irregular dust clouds in orbit around the stars (Wenzel 1968, Grinin 1988, Herbst et al. 1994). The nature of the clouds has been associated with comets orbiting the systems close to the stars (Grady et al. 2000), which requires comets to cover at least 20% of the sky; filamentary dust structures arising in the outer regions of flaring disks (Grinin et al. 1991, Bertout 2000), which is inconsistent with the short period of days or weeks observed in these sources; and filaments arising in the puffed-up inner rim of flat protoplanetary disks (Dullemond et al. 2004).

In Chapter 5 of this work, I describe the observations of Group I Herbig Ae/Be stars obtained as part of a survey of Herbig stars. From the 8 Herbig Ae/Be stars included in the

survey, I detected extended emission 50 to 250 AU in radius for 7 sources at both wavelengths. The FWHM for these systems were 8 to 29 AU in radius. In all the systems, mid-infrared emission could be separated into two components: an unresolved compact emission region and the resolved surface of a flaring disk, with the extended emission contributing less than 50% of the total emission in these systems. Since all the systems were optically thick to mid-infrared radiation perpendicular to the plane of the disks and the disks had inclinations of less than 45 degrees, the mid-infrared emission detected in the systems originated on the surface of the flaring disks closer to us. These results provided evidence of the association of Group I sources with flaring disk geometries. However, the classification of sources into two groups broadly defined two types of geometries, and it is expected that some systems will fill the gap in between as they evolve from one group to the other.

In this chapter, I present mid-infrared observations of the Group II sources included in this survey of Herbig Ae/Be stars. Three of the sources presented here (HD34282, HD144668, and HD169142) show extended mid-infrared emission. Two of these extended sources, HD34282 and HD144668, have been associated with UXOR behavior (Natta et al. 1997). HD 34282 and HD163296 has been classified as Group I and Group II sources by different authors and are considered to be intermediate systems. However, our photometry and classification place these objects with group II sources. To explore the possible evolution of the circumstellar dust between the Group I and Group II sources as a function of stellar parameters, I include all the Herbig Ae/Be stars observed in this survey at the end of this chapter.

Notes on Individual Sources

HD34282: Distance estimates to the A0 Herbig star HD34282 (V1366 Ori) range from 160 pc using Hipparcus parallax (van den Ancker et al. 1998), to 326 pc using photometry (Amado et al. 2006), to 400 pc from dynamical considerations (Pietu et al. 2003). Luminosities estimates

using Hipparcus distance place this object well below the expected luminosity for an A0 star, while the larger distances give a more consistent position in the HR diagram for a PMS star. The mid-infrared spectrum of this source shows strong PAH emission at 8.7 and 11.2 μm , but no silicate emission (Schultz et al. 2005). The star has strong photometric variability with visual amplitude of 2.4 magnitudes (Natta et al. 1997), indicative of UXOR behavior. In addition, Amado et al. (2006) report that HD34282 is rapidly pulsating with the shortest period (18 minutes) known for a star in the instability strip of the HR diagram.

The presence of a large disk with an outer edge of 835 AU and a mass of 0.1 to 0.7 solar masses has been inferred from interferometric observations of ^{12}CO (Pietu et al. 2003, Acke et al. 2005, Merin et al. 2004). The 2.6 mm continuum is not extended (Mannings & Sargent 2000) and the source was undetected in a search for CO at 4.7 μm (Carmona et al. 2005).

HD36917: V372 Ori is a member of the young Orion Nebula Cluster (ONC). Distance estimates to this star range from 270 pc (Tovmassian et al. 1990, 1997) to 500 pc. The distance to ONC is 470 pc (Walker et al. 1969). The absence of emission features in the near-infrared and the low ratio of infrared to stellar luminosity relative to other Herbig stars have been interpreted as clearing of the dust in the inner regions. As a result, Manoj et al. (2002) classified this source as in intermediate stage between Herbig Ae stars and Vega type stars. Polarization studies show a PA of 43 degrees for the dust in the system.

HD37806: MWC 120 was first classified as a Herbig star by Pagodin (1985). $\text{H}\alpha$ spectropolarimetry is consistent with compact $\text{H}\alpha$ emission being polarized by a rotating disk-like structure (Manoj et al. 2002). Near-infrared interferometry results are also consistent with an inner disk only 3.31 mas in size (Eisner et al. 2004)

HD41511: For many years this A type star (MWC 519, 17 Lep, HD41511) was a candidate Herbig Ae star. However, the star was placed above the main sequence with $M_V = -3$ by Perryman et al. (1995). Welty and Wade (1995) reported Doppler motions from a binary system with an M type companion, and concluded that the stars probably form an interacting binary system which has evolved beyond the main sequence since it is unlikely for both stars to be young due to the very different time scales for stellar evolution between A and M type star (Pols et al. 1991).

HD50138: MWC 158 is an isolated star located 290 pc away. This star shares properties with evolved [Be] star and with young HAeBe stars. He I emission line shows variable inverse P cygni profile that has been interpreted as a signature of accretion and stellar wind (Grady et al. 1994, Pogodin et al. 1997). The source has large near- and mid-IR excess characteristic of circumstellar dust; however, the spectral energy distribution of HD50138 shows a steeper decrease of infrared flux towards the far-IR than any other HAeBe star. Baines et al. (2006) found this source to be a wide binary with a separation between 1 and 3 arcsec and a PA of 30 degrees. Polarization studies show strong evidence of a thin gaseous disk with a high inclination angle, almost edge-on (Bjorkman et al. 1998).

HD144668: HR5999 (V856 Sco) is a very well studied Herbig Ae star located in the central part of the Lupus 3 dark cloud. The Hipparcos parallax to HD144668 corresponds to a distance of 208 pc. The optical extinction towards this source is moderate ($A_V = 0.49$) and the star is a fast rotator with velocity, $v \sin i = 204$ km/s (Royer et al. 2002). HD144668 exhibits typical UXOR behavior in the optical (Perez et al. 1992) and UV range (Perez et al. 1993) with variability in the visual of 1.7 magnitudes (Natta et al. 1997).

The mid-infrared ISO spectra of this source shows a weak and broad silicate emission feature Siebenmorgen et al. (2000) indicative of large (sizes $> 1\mu\text{m}$) silicates grains (van Boekel et al. 2003). $\text{H}\alpha$ and Mg II emission line profiles suggest a circumstellar disk seen almost edge-on (Perez et al. 1993). Compact mid-infrared extended emission with a radius of 2-3 AU was detected by Preibisch et al. 2006 using long-baseline interferometry from the VLTI.

The star forms a common proper motion pair with the A1.5 star HR6000 and has another close visual companion at a distance of 1.4 arcseconds and a PA of 111 degrees, Rossiter 3930 (Stecklum et al. 1995). Rossiter 3930 shows $\text{H}\alpha$ emission line (Reipurth 1994) and has been classified as a T-Tauri star. This companion is probably responsible for most of the x ray flux in the system. Grady et al. (2005) observed the system using the Hubble Space Telescope and confirm the classification of the companion as a T Tauri star. Tjin A Dje et al. (1989) also report a spectroscopic binary with a separation of 0.17 AU.

HD150193: MWC 863 (Elias 2-49) is an isolated Herbig A2 star near the ρ Oph molecular cloud at a distance of 150 pc. In optical and near-infrared speckle observations, a companion at a separation of 1.1 arcseconds has been detected (Reipurth and Zinnecker 1993). The companion has been classified as a T Tauri star of spectral type K4 (Bouvier and Corporon 2001).

Several studies suggest the presence of circumstellar dust around this star. ISO mid-infrared spectrum shows amorphous and crystalline silicate features (Meeus et al. 2001) and linear polarization has been observed in the optical and near-infrared (Maheswar et al. 2002, Whittet et al. 1992). Near-infrared images from the 8.2 m Subaru telescope show circumstellar dust extending to a radius of 190 AU, while no extended emission was detected around the companion source HD150193B (Fukagawa et al. 2003). The disk showed asymmetries that could be interpreted by interaction with the companion source.

HD158643: 51 Oph is a B9 star located 130 pc away with a rotation velocity $v \sin i = 267$ km/s. The UV and optical part of the SED does not show any excess emission and Grady et al. (1991) compared the evolutionary state of this source to that of B Pic. However, contrary to B Pic, HD158643 has a large gas content (van den Ancker 2001), which was confirmed by Thi et al. (2004). CO observations are consistent with a small dust disk viewed almost edge-on and the system is probably at an intermediate state between an evolved proto-planetary disk and a debris disk.

HD163296: This is an isolated Herbig Ae star at a distance of 122 pc. The spectral energy distribution of this source is intermediate between the group I and group II sources and it is the only source included in this chapter that does not show significant photometric variability (Henning et al. 1998). The spectrum of this source shows the presence of silicate grains (van den Ancker 2000). HD163296 is associated with large amounts of cold dust, and extended emission has been resolved in CO emission line and 1.3 mm continuum with an inclination of 58 degrees and a PA of 126 degrees (Manning and Sargent 1997). HST STIS images of this system show a large bright disk extending out to a radius of 325 AU, followed by a dark lane with a bright edge at ~ 390 AU (Grady et al. 2000). From these observations the PA angle of the disk was estimated to be 140 degrees, close to the PA derived from mm observations. Extended emission is also seen in Ly α out to a radius of 180 AU (Devine et al. 2000). Doucet et al. (2005) also resolved elongated emission at 20.5 μm and derived an outer disk radius of 200 AU, an inclination of 60 degrees for the disk, assuming flat geometry, and a PA of 105 degrees. K band interferometric observations inferred a size of 0.45 AU for the inner edge of the disk (Monnier et al. 2005). The system is also associated with the Herbig-Haro HH409. HH409 is composed of a

bipolar collimated jet at a PA of 223 degrees, a counter jet at a PA of 42 degrees, and a chain of HH knots.

Observations and Data Reduction

The stars HD36917, HD37806, and HD50138 were observed using Michelle at the Gemini North Telescope. The remaining sources were observed with T-ReCS at the Gemini South Telescope. Images were taken with the Si-5 and Qa filter for all the sources. The standard chop/nod technique was used to remove sky background and thermal emission from the telescope. Nearby point-spread-function (PSF) stars were observed before and after each observation of the Herbig stars. A description of the observational program and its sequence is shown in Table 6-1.

Some of the sources presented here were some of the first science observations taken using the Gemini South Telescope and as a result, some of the images have poor image quality due to unresolved problems with the telescope. Therefore, two sources, HD38087 and HD41511, were excluded from most of the analysis done to the other sources.

Image calibration was done using the standard stars presented in Table 6-2. I used aperture photometry to derive flux densities for all the sources. In addition to emission from dust, the measured fluxes contain mid-infrared radiation from the stellar photosphere. I estimated the contribution from the stellar photospheres using blackbody approximations normalized to the optical photometry of the stars (Malfait et al. 1998). Photospheric fluxes accounted for less than 2 % of the total fluxes in the Si-5 images and less than 4 % of the total fluxes in the Qa images in all the sources except HD38087. Photospheric fluxes in this case account for 15 to 40 % of the total flux in both filters. Previous mid-infrared photometry from IRAS overestimated the mid-infrared fluxes probably due to low spatial resolution, which led to source contamination with the surrounding environment. For sources with available line fluxes from Acke and van den

Ancker (2005), I estimated the contribution of the 11.2 μm PAH emission line and the 11.3 μm silicate emission line to the measured 11.7 μm fluxes. In all cases the contribution from line emission was negligible. I present the derived flux densities, color-corrected fluxes, photospheric fluxes, and resulting mid-infrared flux from warm dust alone in Table 6-3.

Extended Emission

For all the objects included in this study, except HD 38087 and HD41511, we used quadrature subtraction of the FWHM of the science target and PSF star to derive sizes at the FWHM level, or limiting sizes for unresolved sources, for a detailed explanation of this method refer to Chapter 3. We did not resolve extended emission at 11.7 μm for any of the sources presented here at the FWHM level, at 18.3 μm HD34282 was the only source resolved at the FWHM level.

At a fainter level, resolved extended emission was resolved in three Group II sources: HD34282, HD144668, and HD163296. Figure 6-1 presents the FWHM measurements at 11.7 and 18.3 μm for these three objects and their PSF stars. Figure 6-2, presents the 11.7 μm residual emission for the resolved sources at this Herbig stars.

HD34282: Our Gemini observation of this source show the source possibly resolved at the FWHM level at 11.7 μm ; however, the error in the size measurement is comparable with the derived size for the system. From these observations, we derived an upper limit to the disk of 116 AU at this wavelength, assuming the distance to the source to be 400 pc. Residual emission after PSF subtraction is visible in the images, indicative of extended emission at fainter levels. At 1 % of the peak emission, the deconvolved semi-major axis is 1.07 arcsec (429 AU) and the semi-minor axis is 0.68 arcseconds (270 AU). These measurements are consistent with an inclination of about 51 degrees assuming flat geometry and a PA of -22 degrees for the semi-

major axis. The residual emission accounts for at least 22 % of the source total emission at this wavelength.

At 18.3 μm , HD34282 is one of the faintest sources included in this survey; however, the source is clearly resolved at this wavelength with a FWHM deconvolved size of 0.24 ± 0.09 arcseconds or 136 ± 36 AU. The error in the measurements were taken to be half the spread in the FWHM measurements as a conservative upper limit to the error, since we did not have enough points to calculate the standard deviation of the measurements.

HD144668: Most of the mid-infrared emission around HD144668 arises from an unresolved region close to the star. We derived upper limits for this region of 31 AU at 11.7 μm and 40 AU at 18.3 μm . At fainter brightness levels, extended emission is seen in the residual 11.7 μm image, Figure 2. We derived intrinsic sizes at 1 % of the peak emission of 0.46 arcseconds (97 AU) and 0.15 arcseconds (31 AU) for the semi-major and semi-minor axis of the extended emission at this wavelength. The observed ellipticity in this source is consistent with an inclination of 71 degrees assuming flat geometry. The semi-minor axis is almost aligned with the companion source in the plane of the sky at a PA of 113 degrees, with the semi-major axis perpendicular. The observed residual emission accounts only for about 10% of the total emission from HD144668 at this wavelength; therefore most of the excess emission from this source is compact and unresolved.

Rossiter 3930 is the only mid-infrared companion detected in this survey. The source contributes about 5% of the total flux of the system at both 11.7 and 18.3 μm . The derived flux densities are 0.84 Jy at 11.7 μm and 0.56 Jy at 18.3 μm . We combined photometry in the literature for this source with our mid-infrared fluxes for Rossiter 3930, Table 5, to construct the SED of this source and using a blackbody model derive the effective temperature for Rossiter

3930, Figure 3. The best fit to the SED gives an effective temperature of 4060 K and photospheric fluxes of 22.6 and 10.17 mJy at 11.7 and 18.3 μm respectively. The color-corrected flux density from warm dust is then 0.81 and 0.57 Jy at 11.7 and 18.3 μm , resulting in a color temperature of 383 K for the circumstellar dust in Rossiter 3930. Assuming Rossiter 3930 to be coeval with HD144668 and to have an effective temperature of 4060 K, we derive stellar parameters using the Siess et al. (2001) evolutionary tracks. From this analysis, Rossiter 3930 has a spectral type K7, stellar luminosity of 1.7 solar luminosities, a radius of 1.94 solar radius, and a mass of 0.745 solar masses.

Assuming that HD144668 and Rossiter 3930 form a physical pair and the companion is in the plane of the observed disk around HD144668, the deprojected distance between the two sources is 4.3 arcseconds or 900 AU. If the system is flared instead of flat, the inclination angle will be smaller than 71 degrees; however, a flared disk inclined this much will completely obscure the star, and given the low optical extinction to the star the disk is probably not flaring. Using this new separation between the sources, and the estimated masses for the two sources (0.74 and 1.26 solar masses), we can calculate the orbital period of the companion by using:

$$\left(\frac{P}{2\pi}\right)^2 = \frac{r^3}{G(M+m)} \quad (6.1)$$

where P is the period, G is the gravitational constant, r is the distance between the stars, and M and m are the stellar masses. The estimated period for the system is then 13,400 years, more than 3 times the period derived by Stecklum et al. (1995) assuming the projected separation of 1.4 arcseconds as the distance between the two stars. This new result explains why Stecklum et al. (1995) could not detect any angular motion between their observations and those taken by Jeffers et al. (1963).

HD163296: We derived upper limits for the deconvolved radius of the mid-infrared emission at FWHM of < 14 AU at $11.7 \mu\text{m}$ and < 22 AU at $18.3 \mu\text{m}$. At the fainter level, the source shows extended emission. Figure 2 shows the residuals after PSF subtraction at $11.7 \mu\text{m}$. Resolved extended emission is confined to a small region with a semi-minor axis of 0.46 arcseconds (56 AU) and semi-major axis of 0.71 arcseconds (80 AU). This emission accounts for at least 50% of the total flux observed in the system at this wavelength. Assuming flat geometry, these observations are consistent with an inclination of 46 degrees assuming flat geometry and a PA of 145 degrees, in agreement with previous measurements from mm continuum (Manning and Sargent 1997) and optical (Grady et al. 2000).

Dust Properties

In order to study the properties of the CS dust in these systems, we calculated average dust color temperatures using the mid-infrared flux ratios from the observations. Assuming the mid-infrared emission is optically thin and that the measured fluxes at both wavelengths originated within the same regions for each star, which might be the case for almost all sources, we derived color temperatures in the range of 140 K to 1200 K. Temperatures for Group II sources are higher than for Group I sources as expected if all the mid-infrared emission in the systems arise from a compact region closer to the star.

We also calculated warm dust masses using using Equation 3.14. Table 6-6 shows mid-infrared color temperatures, and warm dust masses derived for all the sources, as well as cold dust masses from the literature when available.

Discussion

The observations of Group II HAeBe stars presented here complement the observations of Group I sources presented in Chapters 4 and 5. While all Group I sources show resolved

extended emission at some level, only 25 % of Group II sources show extended emission. This provides strong observational evidence for different geometries in the two groups, with Group I sources having warm dust in a compact region near the star and at larger radii, and Group II sources only having warm dust in a compact unresolved region close to the star.

I also find a strong correlation between mid-IR fluxes and the sources with resolved extended emission. Figure 6-5 shows a plot of the near-IR to mid-IR luminosity ratio versus the mid-IR colors for all the sources in our sample. All the Group I sources have mid-infrared colors $[12]-[18] > 0.5$, the three extended Group II sources have mid-infrared colors $0 < [12]-[18] < 0.5$, and most of the compact unresolved sources have negative mid-infrared colors.

The deconvolved Si-5 and Qa sizes at the FWHM level are the same within the errors for all the sources showing extended emission at this level, Figure 6-6. For the sources HD36112, HD139614, HD179218, and HD34282 where I only have an upper size limit in the Si-5 images, the Qa sizes are smaller than the limit, which is also consistent with the sources having similar sizes at both wavelength. Therefore, I can assume that the observed thermal emissions observed at both filters originate within the same regions. If this also applies for the unresolved sources, I can use the derived dust fluxes to calculate color temperatures and warm dust masses for all the sources in the survey.

The ratio of mid-infrared to sub-mm dust masses, Figure 6-7, shows that the CS environments of the resolved Group II sources differ from resolved Group I sources. In the plot all Group I H A e Be stars have similar warm to cold dust mass ratios. The outliers are HD34282 and HD163296, the only Group II objects in the plot. The lower fraction of warm to cold dust mass seen in these sources implies that less dust is directly exposed to stellar radiation, which is

another evidence that the resolved Group II objects might be transitioning between the two groups.

Evolution between the groups: Dullemond and Dominique (2004a) and (2004b) proposed that dust settling and coagulation could change the geometry of a disk reducing the scale height of the outer disk and causing a flaring disk to partially collapse in the outer edges, and then to become fully self-shadowed. In this scenario, we expect flatter and colder disks associated with Group II sources to be more evolved older systems. To explore this theory, we looked for trends relating stellar ages mid-infrared group classification, sizes of the resolved extended emissions, and contribution of the residual emission to the total emission of the resolved extended systems.

Figure 6-8, first panel, shows $11.7 \mu\text{m}$ deconvolved sizes at the contour level equivalent to 1 % of the peak emission as a function of age for all the resolved sources. For the sources showing elliptical mid-infrared emitting regions, we used the size of the semi-major axis. There is no evidence of evolution among these extended systems relative to their ages.

Figure 6-8, second panel, shows the contribution of the residual emission flux to the total flux of the systems as a function of stellar age for all the resolved sources. For optically thick disks, we expect that the larger the contribution of the extended emission to the total mid-infrared excess of the system, the more warm dust is located at large radii from the central star, which implies either that the disk is intercepting more stellar radiation or that the system is made of smaller grains. Again, there is no correlation of the age of the systems with emission from the extended component. Extended mid-infrared emission in the resolved systems accounts from 15 to 50 % of the total flux of the system, with the majority of the systems having only 20 % of the total emission extended regardless of their ages.

It is possible that the orientation of the systems affects how much extended radiation we can resolve, especially because these systems are optically thick to mid-infrared radiation. For a highly inclined disk, like HD144668, most of the contribution from the semi-major axis will be compact, and this can lead to less extended overall emission; however, we should still be able to resolve the extended emission along the semi-major axis. On average Group II sources included in this survey are more distant than Group I sources; however, this alone is not sufficient to explain the difference between the two groups since some of the closer sources are unresolved.

If the compact Group II sources are more evolved self-shadowed disks, and if the different fractions of extended to compact mid-infrared emission are the result of the evolution of the circumstellar dust, there is no evidence to tie this evolution to stellar ages. If we assume that Group II sources correspond to fully self-shadowed disks, we might expect these systems to be in general older than the Group I sources, which is not the case. On the contrary, Group II sources in this sample are on average younger and more massive than the Group I sources, Figure 6-9. Dust color temperatures for these sources are on average higher, as expected if most of the dust emitting in the mid-infrared is located at very small radii, which explains the observed decrease of dust color temperatures with stellar ages of the systems shown in Figure 6-10.

Dullemond and Dominique (2004b) showed that the time scales for the evolution of flaring disks to self-shadowed disks are only on the order of 1 Myr. Since 10 of the 11 resolved target sources are older than a million year, these time scales contradict the presence of flaring disks around any of these objects. The exception is the only binary system resolved in this survey, HD144668.

Conclusions

I describe here our high-resolution mid-infrared images for 12 Group II HAeBe stars. Three of the sources presented here share properties with typical Group I sources associated with

large protoplanetary flaring disks. Contrary to Group I sources (Chapters 4 and 5), these extended objects show more elliptical emission consistent with systems viewed with an inclination angle of 46 to 71 degrees. The two sources with the higher inclination angles, HD34282 and HD144668, are also the systems that exhibit large photometric variability representative of UXOR behavior. This is in agreement with the theory that UXOR behavior is related to filaments of dust created in the surface layer of protoplanetary disks reddening and polarizing the light from the central star. For these filaments to affect the light from the central star, disks have to be seen at a high inclination angle. The high inclination angle is also consistent with these systems having flatter disks than Group I sources, since a flared disk with a high inclination angle will obscure the central star. HD163296 shows almost spherical extended emission, consistent with a maximum inclination angle of 45 degrees. The inclination angle is consistent with values derived from scattered light and mm line emission and continuum studies (Mannings and Sargent 1997, Grady et al. 2001). These resolved Group II sources also differ from Group I sources in that they have a ratio of warm to cold dust mass two orders of magnitude smaller than all Group I sources. HD34282, HD144668, and HD163296 might belong to an intermediate stage between the very large flaring disks and the compact unresolved sources.

The observations of the disk in HD144668 allow me to constrain the stellar parameters for its companion source (Rossiter 3930). Based on previous near-infrared and optical photometry for Rossiter 3930, I derived an effective temperature of 4060 K for this star. Positioning this source in the HR diagram and assuming that the star is coeval with HD144668, I derived a spectral type of K7, luminosity of 1.07 solar luminosities, a radius of 1.94 solar radius, and a mass of 0.745 solar masses. I also calculate the rotational period of the system to be 13,400 years

assuming that the star lies in the plane of the HD144668 disk; which explains why no angular motion between Rossiter 3930 and HD144668 was detected between observations of the system taken between 1963 and 1995.

This survey of HAeBe stars shows a strong correlation between mid-infrared colors, [12]-[18], and extended emission: resolved extended Group I sources have mid-infrared colors larger than 0.5, compact unresolved Group II sources have negative mid-infrared colors, and resolved Group II sources have mid-infrared colors in between. There is also a clear correlation of sizes at the FWHM from Si-5 and Qa images, which indicates that emission at both wavelengths originate in the same region.

We find no evidence of evolution from Group I sources to Group II sources. On the contrary, Group II sources are on average younger and more massive than Group I sources; therefore, these sources might evolve in different ways. Mid-infrared circumstellar emission in these systems indicate higher dust color temperatures and originate closer to the stars than in Group I sources, where dust emission is more extended and dust color temperatures are lower. In addition, theoretical models have shown that the time scales for the evolution of flaring disks to flat cold disks are on the order of a million year, which is less than the age of almost all the extended sources in this survey.

Table 6-1. Log of observations

Program ID	UT Date	HD #	Filter	On-source Time	PSF Stars	Flux Standards
GN-2003B-Q-25	11/12/2003	50138	Qa	645	PPM 188954	Sirius
	12/16/2003	36917	Si-5, Qa	645	PPM 188954	HD13596, HD37160
	12/18/2003	37806	Si-5, Qa	645	PPM 148614	HD33554, HD1255
Payback	12/4/2003	34282	Si-5, Qa	608	PPM188020	alpha cma
	12/04/2003	38087	Si-5, Qa	608	PPM214663	alpha cma
	12/05/2003	41511	Si-5, Qa	608	PPM217143	alpha cma
	12/05/2003	50138	Si-5	608	PPM188954	alpha cma
	1/29/2004	58647	Si-5, Qa	608		alpha cma
GN-2004B-Q-91	1/17/2005	244604	Si-5, Qa	645	HD37160	HD37160, HD53510
GS-2005B-Q-7	8/20/2005	144668	Si-5	608	PPM320766	HD156277
	9/08/2005	158643	Si-5	608	PPM266246	HD169916
	9/08/2005	163296	Si-5	608	PPM267912	HD169916
	9/09/2005	150193	Si-5	608	PPM266246	HD156277
	9/12/2005	144668	Qa	608	PPM320766	HD156277
	9/12/2005	158643	Qa	608	PPM266246	HD156277
	3/10/2006	150193	Qa	608	PPM266246	HD169916, HD133774
	3/12/2006	163296	Qa	608	PPM267912	HD156277

Table 6-2. Standard stars flux densities

Name	F (Si-5) [Jy]	F (Qa) [Jy]
Sirius	98.50	41.23
HD37160	6.67	2.66
HD53510		1.80
HD13596	6.62	2.63
HD33554	8.06	3.17
HD1255	10.2	4.05
HD156277	5.26	2.11
HD133774	8.87	3.78
HD169916	22.2	8.95

Table 6-3. Derived flux densities

HD #	Observed Flux (Jy)		Color-Corrected Flux (Jy)		BB Photosphere (Jy)		Dust Continuum Flux (Jy)	
	Si-5	Qa	Si-5	Qa	Si-5	Qa	Si-5	Qa
34282	0.51	0.52	0.51	0.54	0.00	0.00	0.51	0.52
36917	1.11	0.65	1.11	0.67	0.02	0.01	1.09	0.64
37806	7.60	6.60	7.59	6.84	0.03	0.01	7.57	6.59
38087	0.03	0.01	0.03	0.01	0.01	0.00	0.02	0.01
41511	115.00	91.00	114.76	94.32	0.23	0.09	114.77	90.91
50138	67.70	70.00	67.65	72.58	0.03	0.01	67.67	69.99
58647	4.40	2.10	4.37	2.17	0.04	0.02	4.36	2.08
144668	15.26	15.90	15.25	16.49	0.05	0.02	15.21	15.88
150193	13.57	20.04	11.78	21.53	0.01	0.00	11.76	20.76
158643	12.50	10.34	12.48	10.72	0.32	0.13	12.18	10.21
163296	15.14	16.40	15.13	17.00	0.07	0.03	15.07	16.37
244604	1.50	1.85	1.50	1.92	0.01	0.00	1.49	1.85

Table 6-4. Derived dust color temperatures and masses for all sources included in this survey. The error bars in the temperature come from the assumed photometric errors of 10% for the Si-5 filter and 15 % for the Qa filter. For two sources, HD50138 and HD150193, we assumed a photometric error of 20% because of the unstable observing conditions during those observations.

HD	T _{dust} (K)	ΔT (K)	Warm Dust Mass (g)	Cold Dust Mass (g)	Warm/Cold Mass
31293	208	25	5.07E+25	3.98E+29	1.27E-04
34282	283	49	2.05E+24	1.99E+30	1.03E-06
36112	203	24	2.62E+25	5.77E+29	4.53E-05
36917	511	166	9.76E+23		
37806	321	63	2.60E+25		
38087	1205	395	7.44E+21		
41511	349	75	1.43E+26		
50138	286	67	1.50E+26		
58647	812	388	6.49E+23		
97048	163	15	1.35E+26	1.83E+30	7.38E-05
100453	147	12	1.09E+26	4.18E+29	2.61E-04
135344	165	16	1.27E+25	3.18E+29	3.99E-05
139614	158	14	5.69E+25	5.37E+29	1.06E-04
144668	279	47	1.82E+25		
150193	227	42	3.33E+25	1.25E+29	2.66E-04
158643	335	69	2.89E+24		
163296	272	44	6.85E+24	1.35E+30	5.06E-06
169142	147	12	7.99E+25	4.78E+29	1.67E-04
179218	198	23	1.87E+26	4.78E+29	3.92E-04
244604	292	80	7.62E+24		

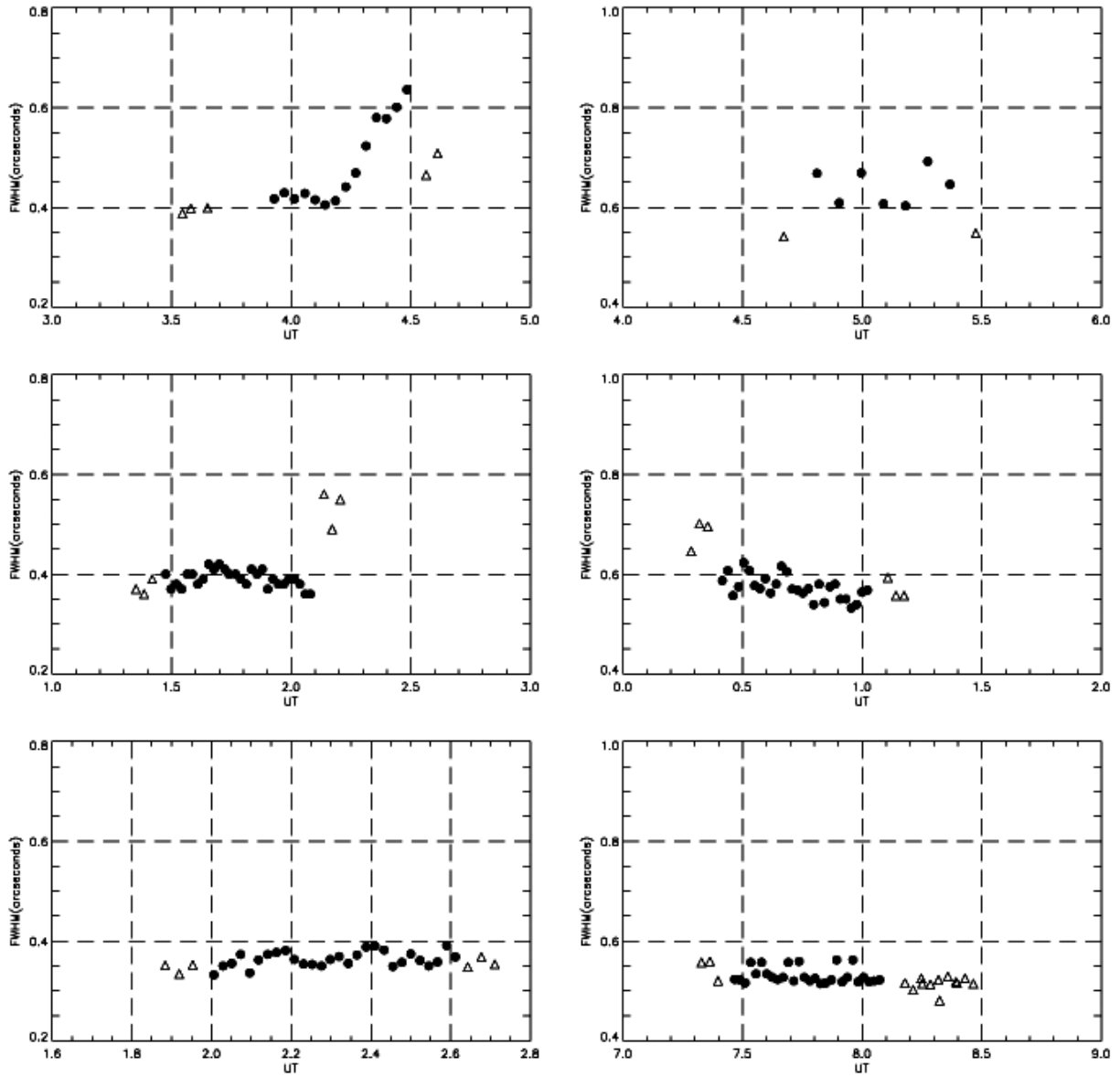


Figure 6-1. FWHM sizes versus UT time for HD34282 (first row), HD144668 (second row), and HD163296 (third row). The filled circles are the measurements for the Herbig stars and the open triangle are the measurements for the PSF stars. The panels in the first column are for Si-5 images and the panels in the second column are the measurements for the Qa images. The only resolved source in this analysis is HD34282 in the Qa filter.

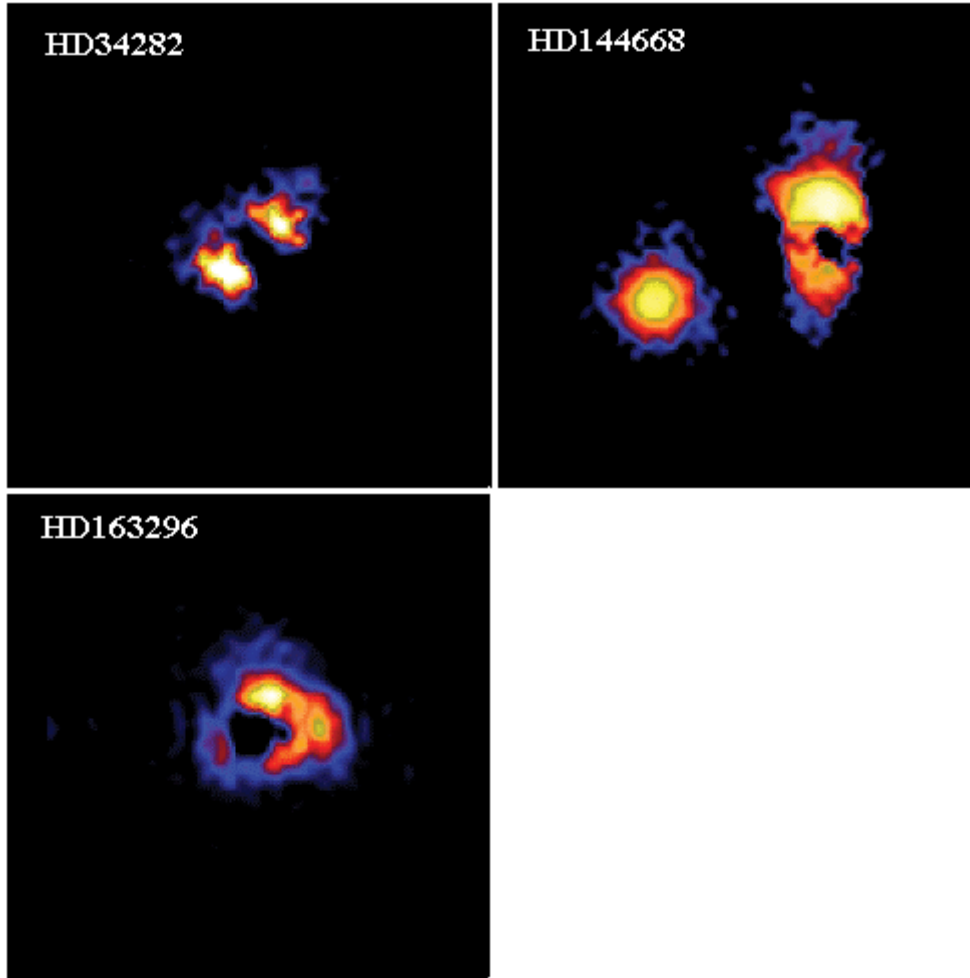


Figure 6-2. Residual emission at 11.7 μm . Each box is 4 arcseconds in size.

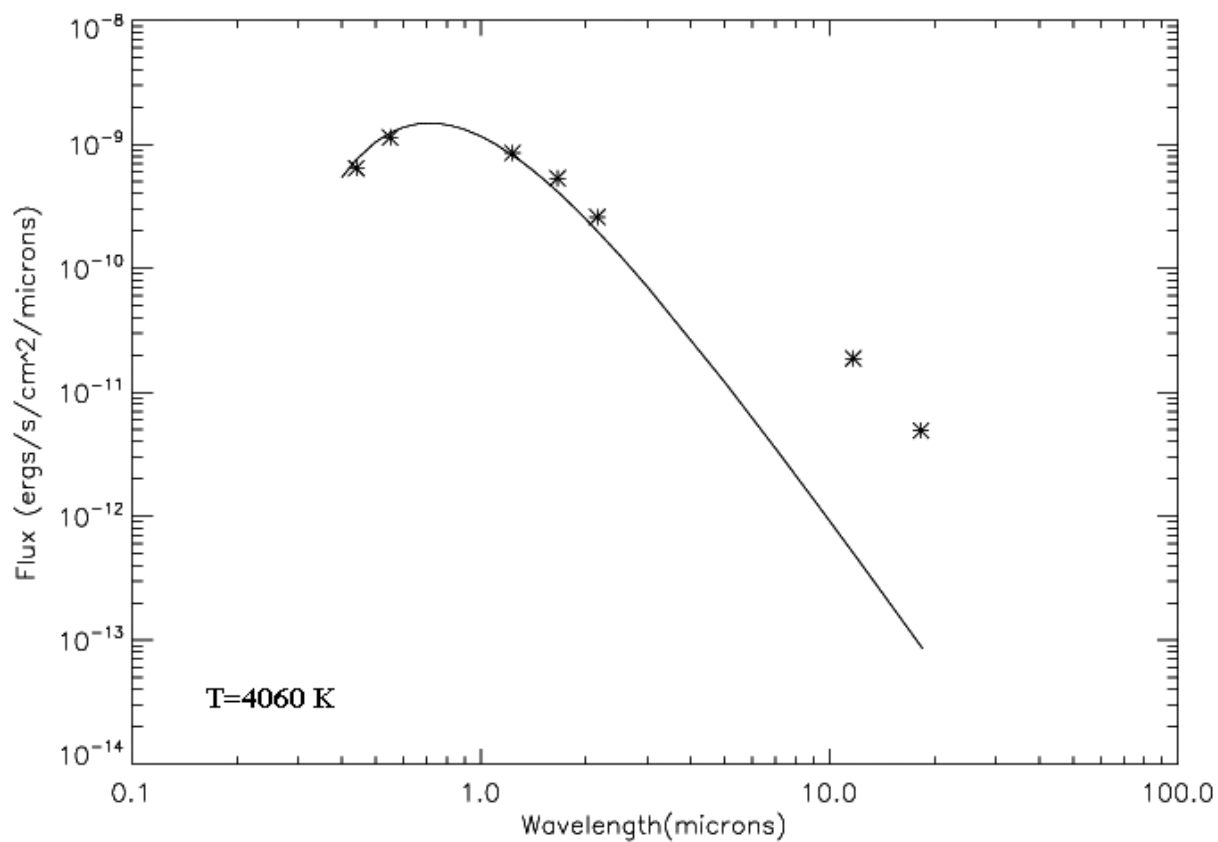


Figure 6-3. Photometry from the literature and from this study for the companion source to HD144668 (Rossiter 3930). The solid line is the best blackbody fit to the optical and near-infrared values. The derived effective temperature for the source is 4060 K.

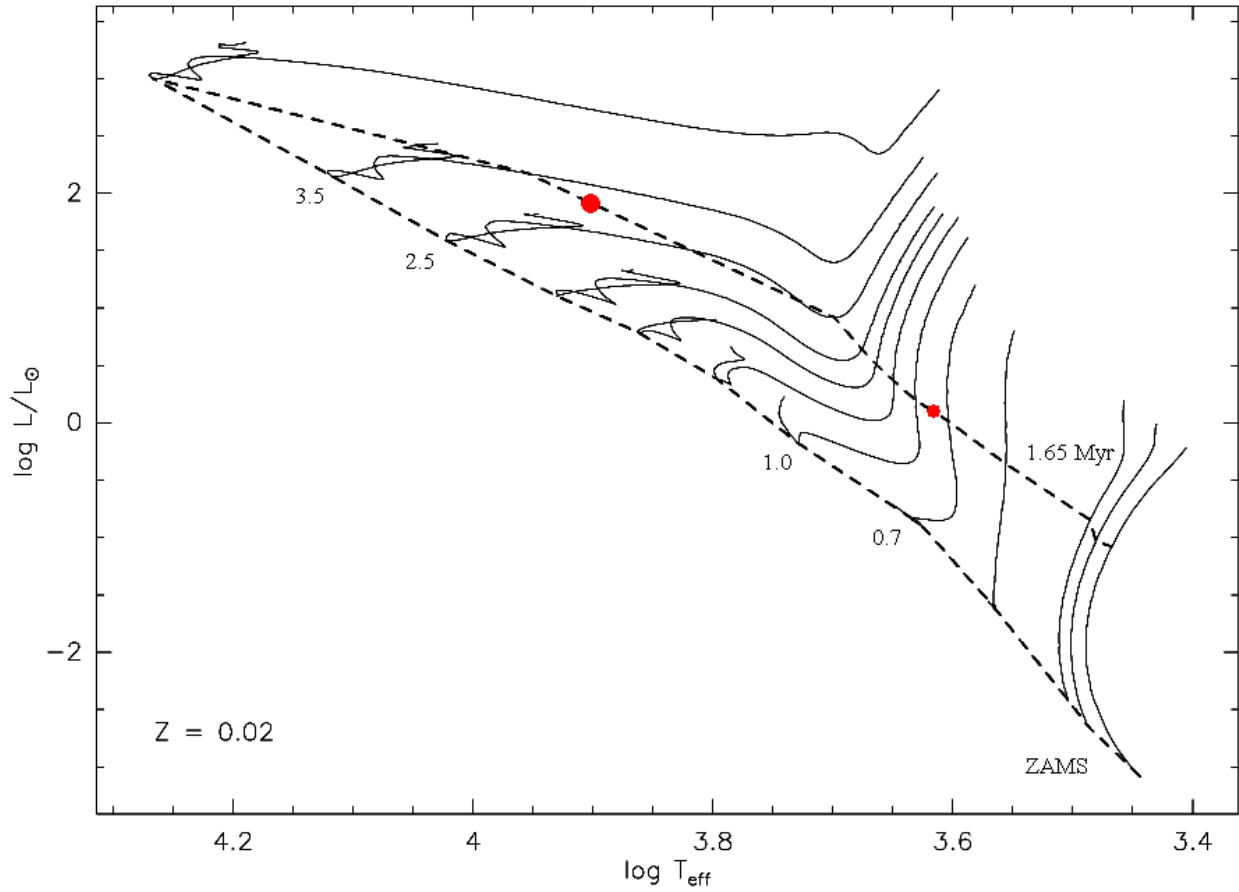


Figure 6-4. H-R Diagram showing the position of HD144668 (largest circle) and Rossiter 3930 (smallest circle). The dash line are the ZAMS and the isochrone for the 1.65 Myr. The solid lines are evolutionary tracks for PMS stars from Seiss et al. (2001).

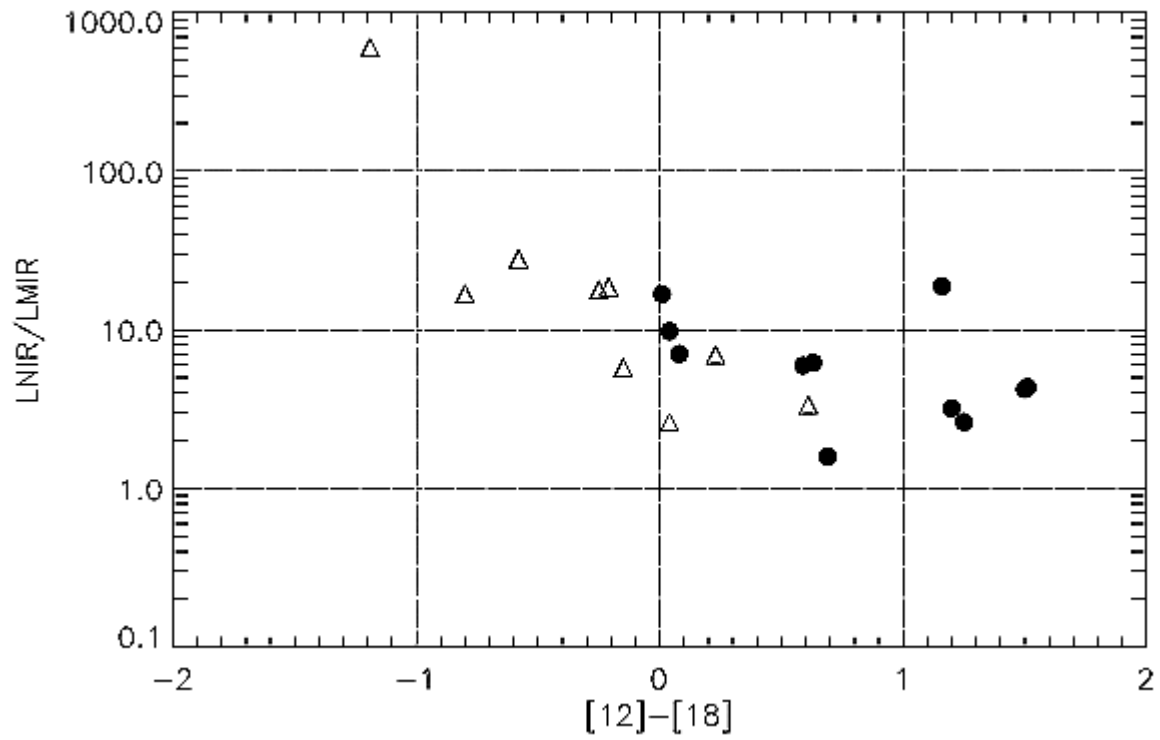


Figure 6-5. Plot of the ratio of near- to mid-infrared luminosity versus mid-infrared colors. The open triangles represent sources with resolved extended emission to some extent. The solid circles are sources with only compact mid-infrared emission.

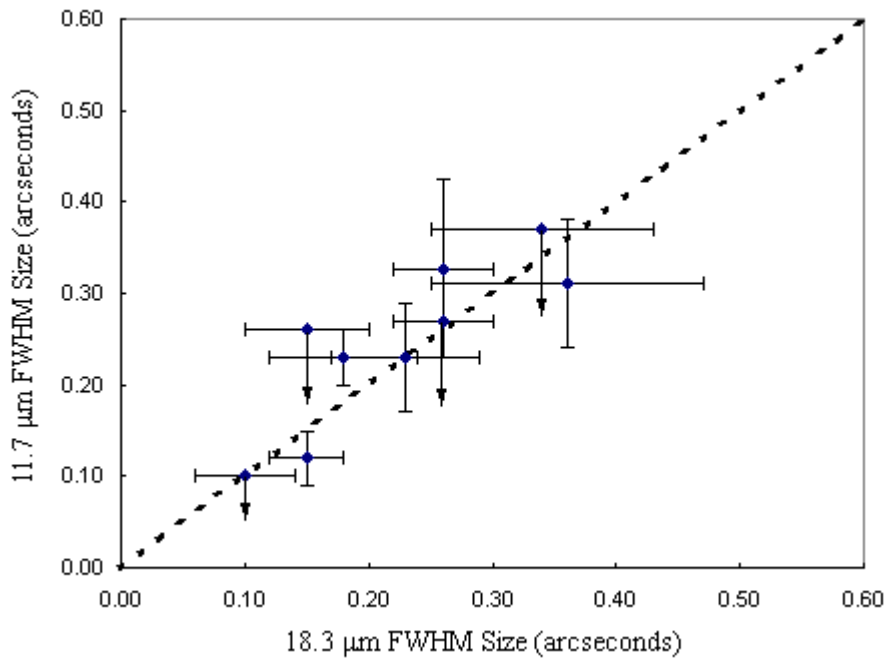


Figure 6-6. Measured sizes at the FWHM level in the Si-5 and Qa images. For sources with unresolved FWHM measurements at 11.7 mm, the upper limit to the size is plotted with an arrow pointing downward. For most sources the sizes are the same within the errors.

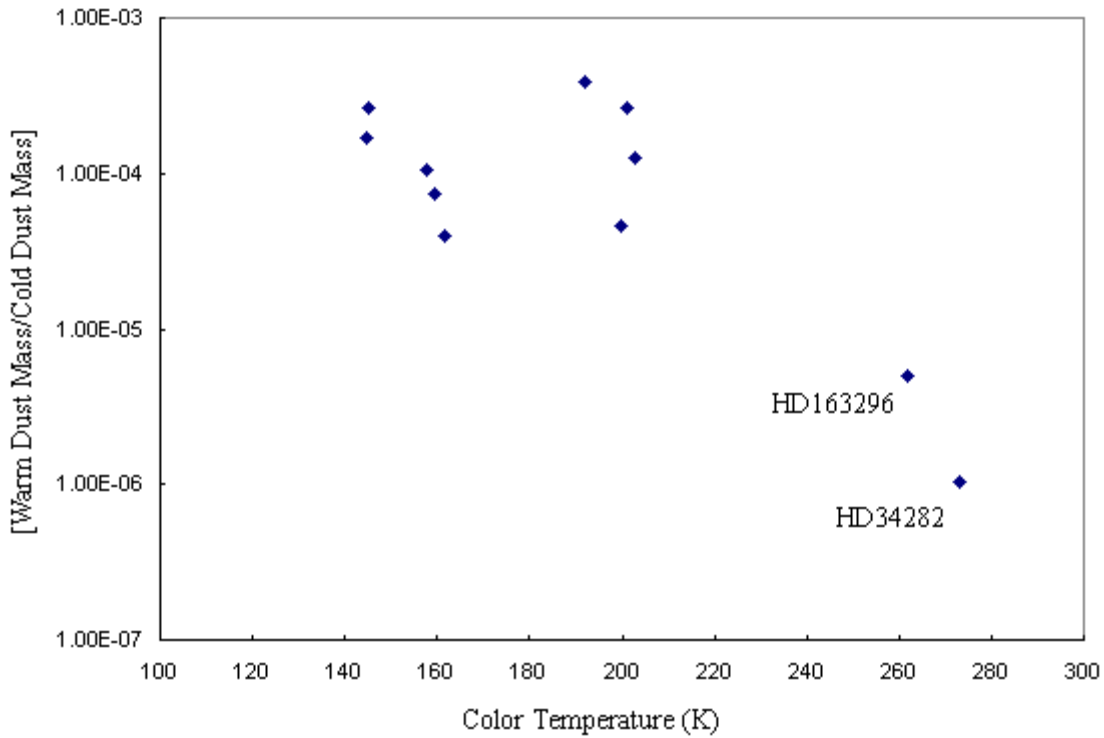


Figure 6-7. Ratio of warm to cold dust disk mass for all the sources with available cold dust mass values in the literature. The circumstellar dust in HD34282 and HD163296 are two order of magnitude colder than in the other sources. The majority of the other sources are Group I sources.

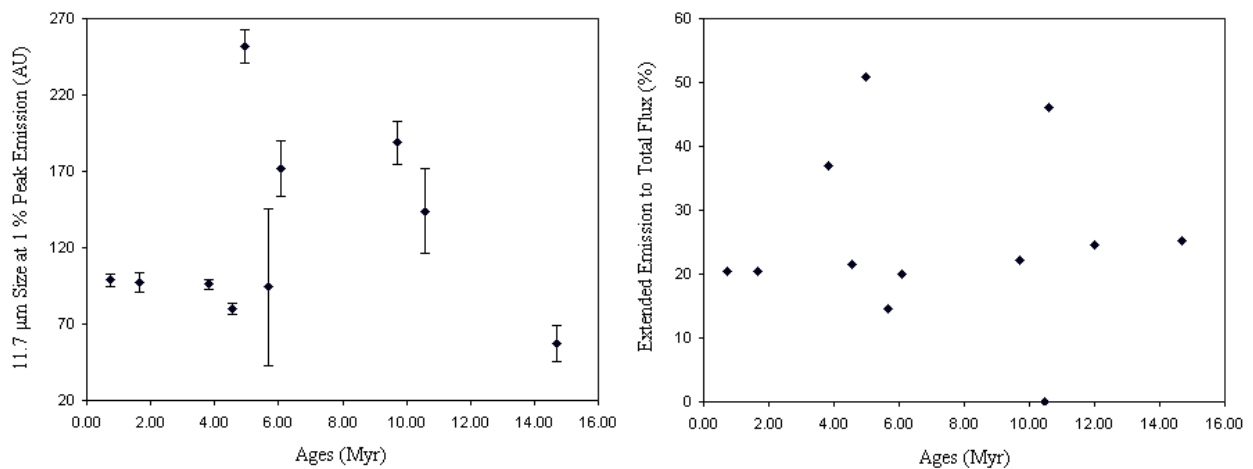


Figure 6-8. Correlation of sizes and fraction of extended to total emission as a function of age. There is no evidence of evolution among these systems.

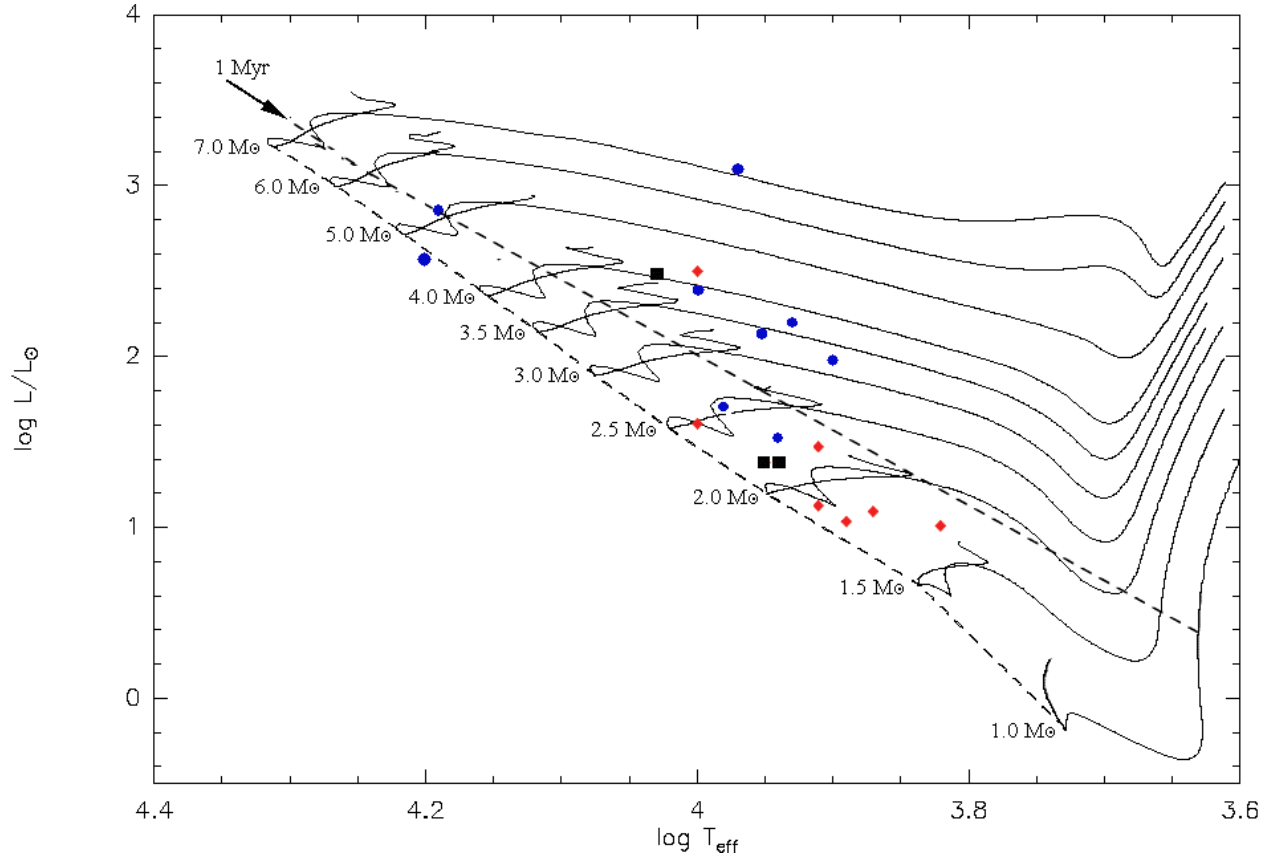


Figure 6-9. Group I and Group II sources in the H-R diagram. Dashed lines represent the zero age main sequence, ZAMS, and the 1 Myr isochrone. Group II sources (blue circles) are on average younger and more massive than Group I sources (red diamonds). The three spatially resolved Group II sources are shown with black squares. Almost all spatially resolved sources are younger than 1 Myr. The exception is HD144668, which is the only binary system resolved in this survey.

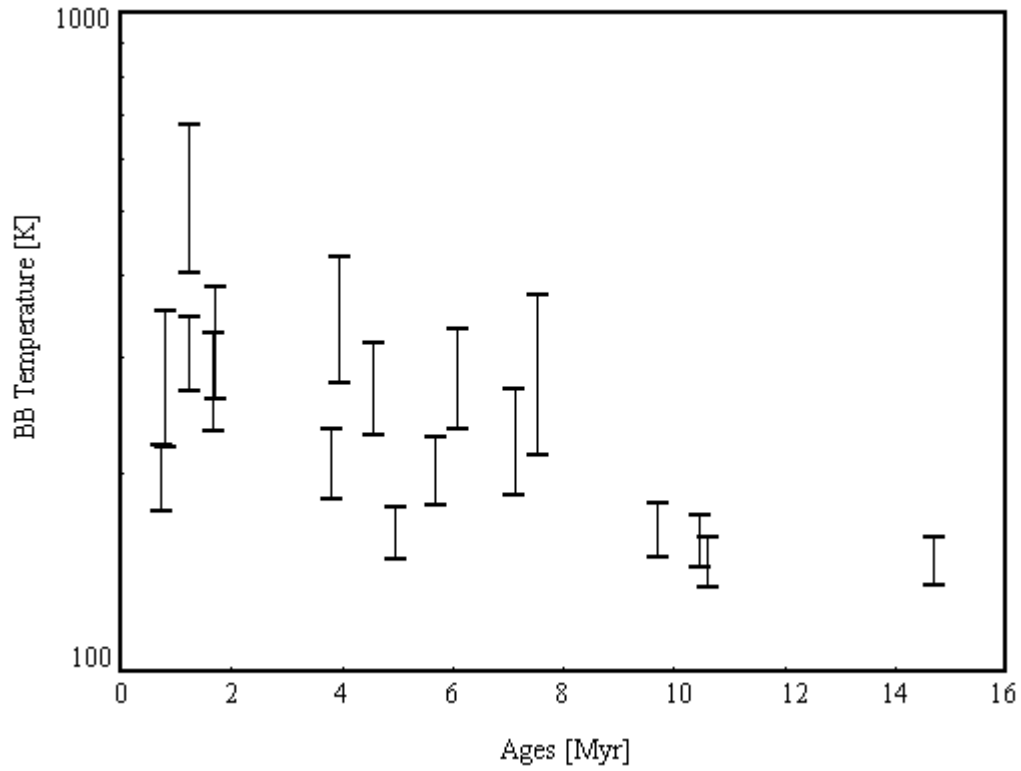


Figure 6-10. Color temperatures for all the sources included in this survey as a function of stellar ages. On average color temperatures decrease with age, implying that most of the dust in the younger systems is located closer to the star.

CHAPTER 8 CONCLUSIONS AND FUTURE WORK

Disk Geometry in Herbig Ae/Be Stars

We have resolved extended emission from all Group I sources in our target list. The majority of these sources have spherical mid-infrared emission extending from a radius of 10 AU to hundreds of AU. This emission could arise either in the optically thin surface layer of an almost face-on flaring disk or a halo. I have used the radial distribution of dust particle sizes derived from the observations to discriminate between these two models. In the case of a halo model composed primarily of very small particles, our line of sight will detect more emission from the halo in the central regions and less in the outskirts of the system, resulting in smaller average dust grain sizes near the center of the system and larger particles at larger radii. In the flaring disk scenario, radiation pressure will produce a segregation of dust particles in the surface layer of the disk, with larger particles — the ones less affected — at smaller radii, and smaller particles at larger radii. We used two of the more extended resolved systems in our survey to evaluate the distribution of grains of different sizes and found larger average grain sizes in the inner regions and smaller grains at larger radii. We conclude that the mid-infrared emitting dust grains are located on the surface layer of a flaring disk and not in a spherical structure. This result does not exclude the presence of additional large-scale haloes in the systems; in fact, observations at other wavelengths have detected very extended nebulosity in many of these sources. Nevertheless, the halo, if present, does not contribute significantly to the mid-infrared emission.

We have also resolved extended mid-infrared emission for 25% of the Group II sources included in this study. Contrary to Group I sources, the emission regions in these objects are more elliptical and consistent with inclined disks. Theoretical models have tied these sources to

self-shadowed flat cold disks. If this is the case for all the Group II sources, we expect to detect only compact unresolved extended emission in these systems. The fact that we detect warm dust in some systems at larger radii implies that those systems are not completely flat and might represent an intermediate stage between the large flaring disks of Group I sources and the flat disks of Group II sources.

This work has shown that warm circumstellar dust in Group I Herbig Ae/Be stars has two components: a compact unresolved component close to the star and a more extended resolved component consistent with emission from the surface layer of a flaring disk, but not with spherical geometries. We also showed that in the majority of Group II sources all the mid-infrared emission originates in a compact unresolved region near the star. Three sources seem to fall between these two categories. Dullemond and Dominique (2004a and 2004b) showed that dust settling and coagulation can change the geometry of a disk reducing the scale height of the outer disk and causing a fully flaring disk to partially collapse first in the outer regions where the disk is least opaque, and then to become fully self-shadowed in about 1 Myr, Figure 7-1. Based on this, I would expect Group II sources to be on average more evolved older versions of the Group I sources. However, we do not find evidence for the evolution of Group I sources into Group II sources; on the contrary, Group II sources are on average younger and more massive than Group I sources and almost all the spatially resolved sources are older than 1 Myr. The circumstellar environment on these sources might evolve in different ways.

Future Work

Notwithstanding the advances in the study of Herbig Ae/Be circumstellar dust, many questions remain. What is the geometry of the younger systems as they evolve from envelopes to flaring disk geometries? Why do we find large flaring disks in systems much older than 1 million year? How does the evolution of Herbig stars compare to the evolution of other PMS stars of

similar mass within the same star-forming region? How does the evolution of Herbig stars in star forming regions compare to the evolution of isolated Herbig stars? What is the influence of clustering on stellar and CS dust evolution? How do the more massive Herbig Be stars evolve?

Expanding what we have learned in the recent years from the evolved isolated Herbig stars to the younger members of this class and the lower mass pre-main sequence T-Tauri stars, requires obtaining new samples of PMS stars of intermediate mass that close the gap between the older optically visible isolated systems and the still embedded sources. Younger stars are probably associated with star forming regions; however, published catalogues of HAeBe stars (The et al. 1994, Malfait et al. 1998) are based on IRAS photometry with low spatial resolution and are unable to discriminate between the infrared emission intrinsic to the sources and that of their complex dusty environments, making the selection of candidates in obscured star forming regions very uncertain. These catalogues are also biased towards the brighter optically visible sources.

To address this issue, over the next year I plan to combine Spitzer photometry from IRAC and MIPS, with much better spatial resolution than IRAS, Figure 8-2, with Flamingos near-infrared spectroscopy to obtain a complete census of PMS stars of intermediate mass in nearby molecular clouds. The new catalogue will allow us to select only those sources with true IR-excess without excluding the younger sources, providing continuity between the more evolved HAeBe stars included in this thesis work and the younger embedded sources of intermediate mass. A larger and unbiased systematic sample is also needed to select PMS stars of intermediate mass for follow up observations at higher spatial resolution from large ground based telescopes.

We would also like to bridge this study of Herbig stars with the evolution of more massive stars. We know that disks are the evidence of stellar formation through gravitational collapse; however, radiation pressure prevents the formation of stars above a certain mass. As an alternative scenario, Bonnell et al. (1998) proposed that massive stars form by coagulation of lower mass objects. We have obtained high-resolution mid-infrared images of two massive Be stars to compare with the sources included in this survey. The images of these more massive stars show very complex extended emission, not compatible with circumstellar disks, as well as lower mass stellar companions. We expect to analyze these systems in detail to gain an understanding of the evolution of CS dust and the stellar formation processes in these more complex systems.

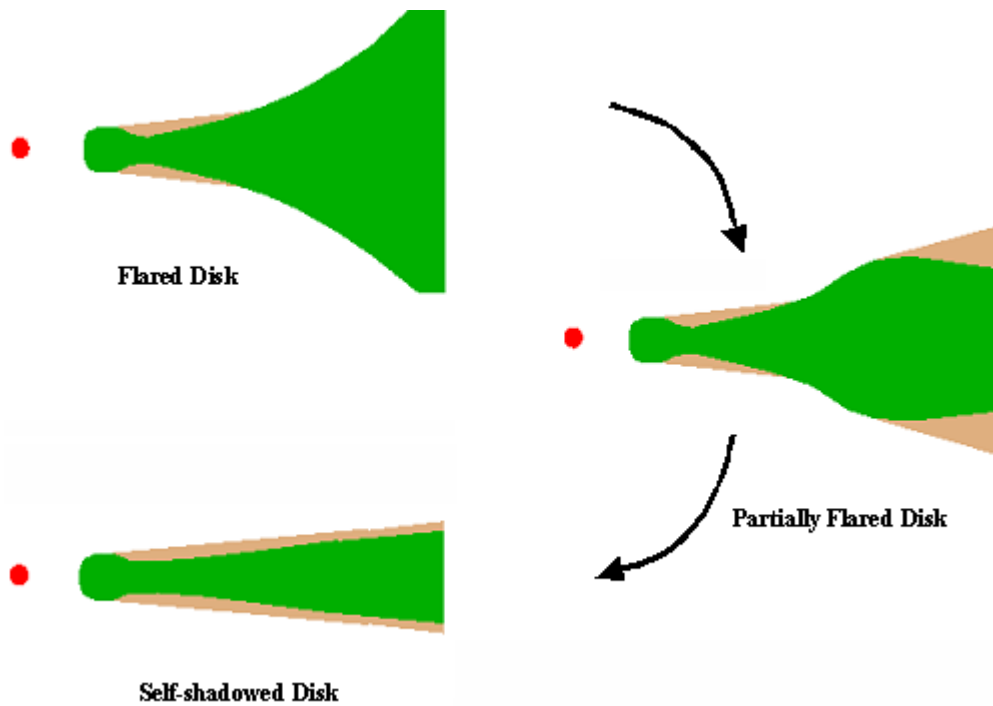


Figure 7-1. Sketch of the evolution of protoplanetary disks in H Ae Be stars proposed by Dullemond and Dominik (2004). The timescales for this evolution is about 1 Myr. The work presented here provides observational evidence for the presence of three geometries consistent with this scenario; however, Group II objects are in general older and more massive than Group I sources and almost all Group I sources are older than 1 Myr.

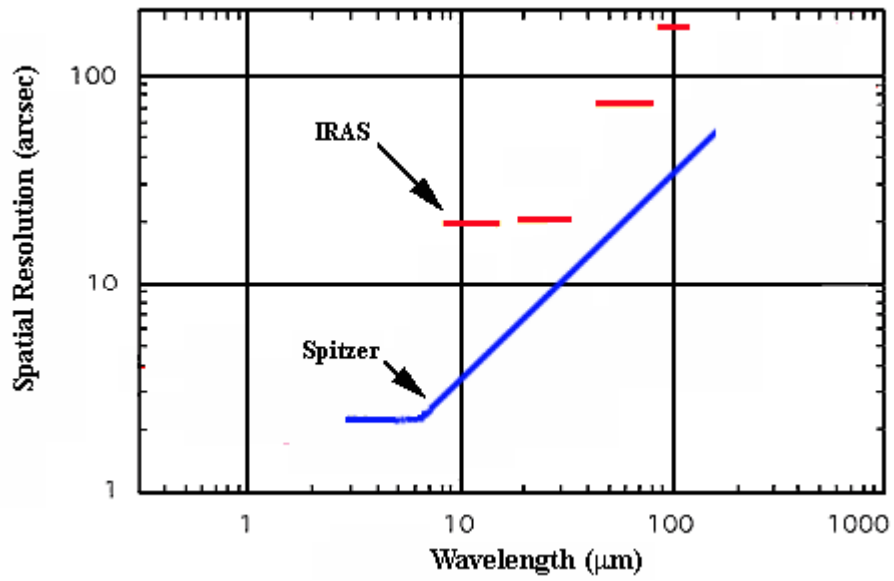


Figure 7-2. Spatial resolution of Spitzer (blue line) from near- to far-infrared wavelengths and the IRAS (red lines) spatial resolution.

LIST OF REFERENCES

- Acke, B. & van den Ancker, M. E. 2004, *A&A*, 426, 151
- Acke, B., van den Ancker, M. E., & Dullemond, C. P. 2005, *A&A*, 436, 209
- Acke, B., van den Ancker, M. E. 2006, *A&A*, 449, 267
- Acke, B., van den Ancker, M. E., & Dullemond, C. P. 2005, *A&A*, 436, 209
- Ageorges, N., Fischer, O., Stecklum, B., Eckart, A., & Henning, Th. 1996, *ApJL*, 463, 101
- Amado, P. J., Rodríguez, E., Choo, Kyung-J., Kim, S.-L., Garrido, R., Suárez, J. C., Moya, A., Martín-Ruíz, S. 2006, *MnSAI*, 77, 97
- Assendorp, R., Wesselius, P. R., Prusti, T., & Whittet, D. C. B. 1990, *MNRAS*, 247, 624
- Backman, D. E. & Paresce, F. 1993, in *Protostars & Planets III*, ed. E. H. Levy & J. I. Lunine (Tucson: Univ. Arizona Press), 1253
- Baines, D., Oudmaijer, R. D., Porter, J. M., & Pozzo, M. 2006, *MNRAS*, 367, 737
- Bally, J., Walawender, J., Luhman, K. L., & Fazio, G. 2006, *AJ*, 132, 1923
- Baraffe, I., Chabrier, G., Allard, F. & Hauschildt, P. H. 1998, *A&A*, 337, 403
- Bastien, P. 1985, *ApJS*, 59, 277
- Beckwith, S. V. W., Sargent, A. I., Chini, R. S., & Guesten, R. 1990, *AJ*, 99, 924
- Berrili, F., Corciulo, G., Ingrassio, G., Lorenzetti, D., Nissini, B., & Strafella, F. 1992, *ApJ* 398, 254
- Bertout, C. 2000, *A&A*, 363, 984
- Bibo, E. A. & The, P. S. 1991, *A&AS*, 89, 319
- Bjorkman, K. S., Miroshnichenko, A. S., Bjorkman, J. E., Meade, M. R., Babler, B. L., Code, A. D., Anderson, C. M., Fox, G. K., & 4 coauthors, 1998, *ApJ*, 509, 904
- Bohm, T. & Catala, C. 1994, *ASP Conference Series*, 62, 214
- Bouvier, J. & Corporon, P. 2001, *IAUS*, 200, 155
- Brandner, W., Potter, D., Sheppard, S., Moneti, A., & Zinnecker, H. 2002, *The Origin of Stars and Planets: The VLT View*, *OSP Conference Proceedings*, Ed. J.F. Alves & M.J. McCaughrean. (Springer-Verlag), 331

- Carmona, A., van den Ancker, M. E., Thi, W.-F., Goto, M., & Henning, Th. 2005, *A&A*, 436, 977
- Charbonnel, C., Däppen, W., Schaerer, D., Bernasconi, P. A., Maeder, A., Meynet, G., & Mowlavi, N. 1999, *A&AS*, 135, 405
- Chen, C. H. & Jura, M. 2003, *ApJ*, 591, 267
- Chen, X. P., Henning, T., van Boekel, R., & Grady, C. A. 2006, *A&A*, 445, 331
- Chiang, E. I. & Goldreich, P. 1997, *ApJ*, 490, 368
- Cidale, L., Zorec, J., & Tringaniello, L. 2001, *A&A*, 368, 160
- Cohen, M. & Kuhl, L. V. 1979, *ApJSS*, 41, 743
- Cohen, M. 1980, *MNRAS*, 191, 499
- Cohen, M., Walker, R. G., Carter, B., Hammersley, P., Kidger, M., & Noguchi, K. 1999, *AJ*, 117, 1864
- Corcoran, M. & Ray, T. 1994, *ASP Conference Series*, 62, 151
- Corder, S. A., Eisner, J. A., & Sargent, A. L. 2005, *ApJL*, 622, 133
- Coulson, I. M. & Walther, D. M. 1995, *MNRAS*, 274, 977
- Covino, E., Alcalá, J. M., Allain, S., Bouvier, J., Terranegra, L., & Krautter, J. 1997, *A&A*, 328, 187
- Dent, W. R. F., Torrelles, J. M., Osorio, M., Calvet, N., & Anglada, G. 2006, *MNRAS*, 365, 1283
- Devine, D., Grady, C. A., Kimble, R. A., Woodgate, B., Bruhweiler, F. C., Boggess, A., Linsky, J. L., & Clampin, M. 2000, *ApJL*, 542, 115
- Di Francesco, J., Evans, N. J., Harvey, P. M., Mundy, L. G., & Butner, H. M. 1994, *ApJ*, 432, 710
- Dominik, C., Dullemond, C. P., Waters, L. B. F. M., & Walch, S. 2003, *A&A*, 398, 607
- Doucet, C., Pantin, E., Lagage, P. O., & Dullemond, C. P. 2006, *A&A*, 460, 117
- Ducourant, C., Teixeira, R., Périé, J. P., Lecampion, J. F., Guibert, J., & Sartori, M. J. 2005, *A&A*, 438, 769
- Dullemond, C. P., Dominik, C., & Natta, A. 2001, *ApJ*, 560, 957
- Dullemond, C. P. & Dominik, C. 2004, *A&A*, 417, 159

- Dullemond, C. P. & Dominik, C. 2004, *A&A*, 421, 1075
- Dullemond, C. P., van den Ancker, M. E., Acke, B., & van Boekel, R. 2003, *ApJ*, 594, 47
- Eisner, J. A., Lane, B. F., Akeson, R. L., Hillenbrand, L. A., Sargent, A. I. 2003, *ApJ*, 588, 360
- Eisner, J. A., Lane, B. F., Hillenbrand, L. A., Akeson, R. L., Sargent, A. I. 2004, *ApJ*, 613, 1049
- Elia, D., Strafella, F., Campeggio, L., Giannini, T., Lorenzetti, D., Nisini, B., & Pezzuto, S. 2004, *ApJ*, 601, 1000
- Evans, N. J. & Di Francesco, J. 1995, *RMAAC*, 1, 187
- Finkenzeller, U. & Mundt, R. 1984, *A&AS*, 55, 109
- Finkenzeller, U. & Jancovics, I. 1984 *A&AS*, 57, 285
- Fisher, R. S., Telesco, C. M., Piña, R. K., Knacke, R. F., & Wyatt, M. C. 2000, *ApJL*, 532, 141
- Fukagawa, M., Hayashi, M., Tamura, M., Itoh, Y., Hayashi, S. S., Oasa, Y., Takeuchi, T., Morino, J., Murakawa, K., Oya, S., & 13 coauthors 2004, *ApJ*, 605, 53
- Garcia-Lario, P., Riera, A., & Manchado, A. 1998, *A&A*, 334, 1007
- Goodson, A. P. & Winglee, R. M. 1999, *ApJ*, 524, 159
- Grady, C. A., Perez, M. R., & The, P. S. 1994, *ASPC*, 62, 409
- Grady, C. A., Woodgate, B., Bruhweiler, F. C., Boggess, A., Plait, P., Lindler, D. J., Clampin, M., & Kalas, P. 1999, *ApJL*, 523, 151
- Grady, C. A., Polomski, E. F., Henning, Th., Stecklum, B., Woodgate, B. E., Telesco, C. M., Piña, R. K., Gull, T. R., Boggess, A., Bowers, C. W., & 19 coauthors, 2001, *AJ*, 122, 3396
- Grady, C. A., Devine, David, Woodgate, B., Kimble, R., Bruhweiler, F. C., Boggess, A., Linsky, J. L., Plait, Philip, Clampin, M., & Kalas, P. 2005, *ApJ*, 544, 895
- Greaves, J. S. & Holland, W. S. 2000, *ASPC*, 219, 296
- Greenberg, R., Hartmann, W. K., Chapman, C. R., & Wacker, J. F. 1978, *Icarus*, 35, 1
- Grinin, V. P., Rostopchina, A. N., & Shakhovskoi, D. N. 1998, *AstL*, 24, 802
- Guillois, O., Ledoux, G., & Reynaud, C. 1999, *ApJL*, 521, 133
- Habart, E., Natta, A., Testi, L., & Carillet, M. 2006, *A&A*, 449, 1067
- Habart, E., Testi, L., Natta, A., & Carillet, M. 2004, *ApJL*, 614, 129

- Habart, E., Testi, L., Natta, A., & Vanzani, L. 2003, *A&A*, 400, 575
- Haikala, L. K., Harju, J., Mattila, K., & Toriseva, M. 2005, *A&A*, 431, 149
- Hamaguchi, K., Yamauchi, S., & Koyama, K. 2005, *ApJ*, 618, 360
- Hamann, F. & Persson, S. E. 1992, *ApJS*, 82, 285
- Hanson, M. M., Rieke, G. H., & Luhman, K. L. 1998, *AJ*, 116, 1915
- Hartmann, L., Kenyon, S. J., & Calvet, N. 1993, *ApJ*, 407, 219
- Hauschildt, P. H., Allard, F., & Baron, E. 1999, *ApJ*, 512, 37
- Helou, G. 1989, *IAUS*, 135, 285
- Henning, Th., Burkert, A., Launhardt, R., Leinert, Ch., & Stecklum, B. 1998, *A&A*, 336, 565
- Herbig, G. H. 1960, *ApJS*, 4, 337
- Herbst, W., Herbst, D. K., Grossman, E. J., & Weinstein, D. 1994, *AJ*, 108, 1906
- Hildebrand, R. H. 1983, *QJRAS*, 24, 267
- Hillenbrand, L. A., Strom, S. E., Vrba, F. J., & Keene, J. 1992, *ApJ* 397, 613
- Hubrig, S., Szeifert, T., Scholler, M., & Yudin, R. 2004, *A&A*, 415, 661
- Hubrig, S., Yudin, R.V., Scholler, M., & Pogodin, M. A. 2006, *A&A*, 446, 1089
- Hubrig, S., Castelli, F., & Wahlgren, G. M. 1999, *A&A*, 346, 139
- Jayawardhana, R., Fisher, R. S., Telesco, C. M., Piña, R. K., Barrado y Navascués, D., Hartmann, L. W., & Fazio, G. G. 2001, *AJ*, 122, 2047
- Jeffers, H. M., van D., W. H., & Greeby, F. M. 1963, *Index Catalogue of Visual Double Stars*, 1961
- Jura, M., Webb, R. A., & Kahane, C. 2001, *ApJL*, 550, 71
- Klahr, H. & Lin, D. 2000, in *ASP Conf. Ser. 219, Disks, Planetesimals, & Planets*, ed. F. Garzón et al. (San Francisco: ASP), 375
- Kouwenhoven, M. B. N., Brown, A. G. A., Zinnecker, H., Kaper, L., & Portegies Zwart, S. F. 2005, *A&A*, 430, 137
- Kozlova, O. V 2004, *Ap*, 47, 287
- Kuhn, J. R., Potter, D., & Parise, B. 2001, *ApJL*, 553, 189

- Lada, C. J. & Adams, F. C. 1992, *ApJL*, 393, 278
- Lagage, P., Doucet, C., Pantin, E., Habart, E., Duchêne, G., Ménard, F., Pinte, C., Charnoz, S., Pel, J. 2006, *Science*, 314, 621
- Leinert, Ch., van Boekel, R., Waters, L. B. F. M., Chesneau, O., Malbet, F., Köhler, R., Jaffe, W., Ratzka, Th., Dutrey, A., Preibisch, Th., & 28 coauthors, *A&A*, 423, 537
- Liu, W. M., Hinz, P. M., Hoffmann, W. F., Brusa, G., Miller, D., & Kenworthy, M. A. 2005, *ApJL*, 618, 133
- Liu, W. M., Hinz, P. M., Meyer, M. R., Mamajek, E. E., Hoffmann, W. F., Brusa, G., Miller, D., & Kenworthy, M. A. 2006, *astro-ph/0612448v1*
- Lorenzetti, D., Nisini, B., Berrilli, F., & Strafella, F. 1994, *ASP Conference Series*, 62, 189
- Malfait, K., Bogaert, E., & Waelkens, C. 1998, *A&A* 331, 211
- Mannings, V. & Sargent, A. I. 1997, *ApJ* 490, 792
- Marsh, K. E., Van Cleve, J. E., Mahoney, M. J., Hayward, T. L., & Houck, J. R. 1995, *ApJ*, 451, 777
- Mathis, J. S. 1990, *ARA&A*, 28, 37
- Meeus, G., Waters, L. B. F. M., Bouwman, J., van den Ancker, M. E., Waelkens, C., & Malfait, K. 2001, *A&A*, 365, 476
- Men'shchikov, A. B. & Henning, T. 1997, *A&A*, 318, 879
- Mendoza, V. E. 1966, *ApJ*, 143, 1010
- Millan-Gabet, R., Schloerb, F. P., & Traub, W. A. 2001, *ApJ*, 546, 358
- Millan-Gabet, R., Schloerb, F. P., Traub, W. A., Malbet, F., Berger, J. P., Bregman, J. D. 1999, *ApJL*, 513, 131
- Moffat, A. F. J. 1969, *A&A*, 3, 455
- Monnier, J. D., Berger, J.-P., Millan-Gabet, R., Traub, W. A., Schloerb, F. P., Pedretti, E., Benisty, M., Carleton, N. P., Huguenaer, P., Kern, P., & 6 coauthors 2006, *ApJ*, 647, 444
- Monnier, J. D., Millan-Gabet, R., Billmeier, R., Akeson, R. L., Wallace, D., Berger, J.-P., Calvet, N., D'Alessio, P., Danchi, W. C., Hartmann, L., & 24 coauthors, 2005, *ApJ*, 624, 832
- Mouillet, D., Larwood, J. D., Papaloizou, J. C., & Lagrange, A. M. 1997, *MNRAS*, 292, 896
- Muzerolle, J., Hillenbrand, L., Calvet, N., Briceño, C., & Hartmann, L. 2003, *ApJ*, 592, 266

- Natta, A., Meyer, M. R., & Beckwith, S. V. W. 1998, *ASPC*, 132, 265
- Ossenkopf, B., Henning, T., & Mathis, J. S. 1992, *A&A*, 261, 567
- Palla, F. & Stahler, S. W. 1993, *ApJ*, 418, 414
- Pantin, E., Bouwman, J., & Lagage, P. O. 2005, *A&A*, 437, 525
- Pezzuto, S., Strafella, F., & Lorenzetti, D. 1997, *ApJ*, 485, 290
- Piétu, V., Guilloteau, S., & Lagage, P. O. 2005, *A&A*, 443, 945
- Piétu, V., Dutrey, A., & Kahane, C. 2003, *A&A*, 398, 565
- Polomski, E. F., Telesco, C. M., Piña, R., & Schulz, B. 2002, *AJ*, 124, 2207
- Raman, A., Lisanti, M., Wilner, D. J., Qi, C., & Hogerheijde, M. 2006, *AJ*, 131, 2290
- Roche, P. F. 2004, *Adv. Space Res.*, 34, 583
- Siess, L., Dufour, E., Forestini, M. 2000, *A&A*, 358, 593
- Stahler, S. W. 1988, *ApJ*, 332, 804
- Strom, S. E., Strom, K. M., & Yost, J. 1972, *ApJ* 173, 353
- The, P. S., de Winter, D., & Perez, M. R. 1994, *A&AS*, 104, 315
- Trujillo, I., Aguerri, J. A. L., Cepa, J., & Gutierrez, C. M. 2001, *MNRAS*, 328, 977
- van den Ancker, M. E., Bowman, J., Wesselius, P. R., Waters, L. B. F. M., Dougherty, S. M., & van Dishoeck, E. F. 2000, *A&A*, 357, 325
- van den Ancker, M. E., de Winter, D., Tjin, A., & Djie, H. R. 1998, *A&A*, 330, 145
- van Boekel, R., Min, M., Leinert, Ch., Waters, L. B. F. M., Richichi, A., Chesneau, O., Dominik, C., Jaffe, W., Dutrey, A., Graser, U., & 13 coauthors, 2004, *Nature*, 432, 479
- Vink, J. S., Drew, J. E., Harries, T. J., & Oudmaijer, R. D. 2002, *ASP Conference Series*, 267, 439
- Vinković, D., Ivezić, Ž., Miroshnichenko, A., & Elitzur, M.. 2003, *MNRAS*, 346, 1151
- Wyatt, M. C., Dermott, S. F., Telesco, C. M., Fisher, R. S., Grogan, K., Holmes, E. K., & Piña, R. K. 1999, *ApJ*, 527, 918

BIOGRAPHICAL SKETCH

Naibi Marinas was born in Havana, Cuba, in 1971. As a child she loved making up stories, drawing, dancing, climbing trees and catching bees. The world was perfect and revolved around her family until the spring of 1980. April that year, a group of Cubans drove a bus into the Peruvian embassy and were granted asylum. The Cuban government asked for the people to be turned in and after the refusal of Peru, removed all guards from the embassy. Within a few days more than 10,000 Cubans were crowded in the tiny grounds of the embassy. Naibi's father, Daniel, was one of those Cubans. Looking for a way to leave the country, he and a friend had decided to enter the embassy. Eleven days later, at dinnertime, eight-year-old Naibi opened the front door to her father; he returned home very skinny and wearing a strange torn blue shirt; Naibi was allowed to go to bed late that night and fall slept at the dinner table listening to her father's voice. Soon after that, Daniel left the country in the Mariel Boatlift, and two years later, his parents, Odilia and Paco, followed him. The family was broken apart and the safety of Naibi's world ended. Because her father had left the country, her mom, America, who worked at the Cuban Science Academy as a language teacher was expelled from her job, and neighbors tried to take their house and leave them homeless. In the years that followed people were stoned on the streets, left bruised and bleeding, and sometimes even killed in public. Life had taken a bizarre dark turn.

At the age of 12, Naibi was admitted into Lenin School for Exact Sciences located just outside Havana. Because of her family involvement in Mariel, her acceptance into the school was controversial and she had to prove she belonged there and deny any contact with her father and grandparents every day for six years. She was part of a dance group, performed in plays, wrote short stories and poems, and developed a passion for mathematics and physics. At Lenin School, students lived outside the Cuban reality, there was no sign of political or economic

struggle, and the short visits to family on weekends were not long enough for students to learn about the situation of the country, the turmoil Naibi had lived in the 1980s faded away. Her career plan was to become either a writer or a physicist; however, her literature teacher assured her that if she studied physics she would end up being a science fiction writer and not a scientist. By the time she finished high school her academic choices were either apply to philology and become a writer (first choice) or apply to physics and become a scientist (second choice). That year, 1989, Havana University did not offer philology as a major and she entered the physics program at Havana University.

The first year at Havana University brought reality back to her life. Outside the school there was no food, or money, and people were reprimanded for only talking about the situation in the country. In the mornings, while leaving to go to school, Naibi's grandfather, Raul, had to walk with her to the bus stop because of street crime. On her way there, most mornings with an empty stomach, she saw people collecting leaves from orange and lemon trees to boil and make tea for breakfast. During that first year in physics, philology was offered again as a major; Naibi applied to change programs and was admitted into philology in 1990. She studied philology for 2 years; she was not interested in writing anymore, but enjoyed linguistics, the science of language, and decided to specialize in that area. In the country, discontent with the government grew steadily over the next year. As her younger brother, Dany, got closer to 15 years of age, military age in Cuba, America and Naibi worried about him being drafted for the mandatory military service and being sent abroad to fight in a foreign war. Her mother proposed to leave for the United States. Ties with her father and paternal grandparents had been kept secret all those years, but they had always wanted to reunite the family. Despite her own feelings, Naibi accepted the family decision and the family left Cuba in October 1992.

A few months later, Naibi started English classes at Miami-Dade College. Because studying science was going to be easier than studying philology in a foreign language, she declared a major in physics. A few years later, she transferred to the University of Florida in Gainesville, where she worked in low temperature physics. During the summer of 1999, Naibi attended a summer research program at the Harvard-Smithsonian Center for Astrophysics to work on improving a laser gauge. That summer, she decided to attend graduate school in astronomy and was accepted into the astronomy program at the University of Florida. From her first year, she enjoyed doing research in astronomy and spending whole nights awake working on telescopes; however, she never liked astronomy classes the way she enjoyed literature, math and physics. She balanced her academic life by gardening at night with a flashlight after going home from school and by doing black and white photography in her spare time. The little free time she had for herself ended in December 3, 2003 when Naibi gave birth to her son Diego. That same night, in the Chilean Andes, the first data for her PhD thesis was collected. This summer, on May 2007, Naibi will finally become a scientist. After thirty five years, Naibi's world is far from perfect, but still revolves around her family: the ones left behind, her grandparents who passed away, her invincible mom, her grown up brother, her loving father, and her amazing music loving son.